GEOLOGY AND GENESIS OF THE GEORGE FISHER ZN-PB-AG DEPOSIT, MOUNT ISA, AUSTRALIA.

VOLUME 1

Thesis submitted by

Lucy H. Chapman B.Sc.(Hons.)

in August, 1999,

for the degree of Doctor of Philosophy

in the School of Earth Sciences,

James Cook University.

ABSTRACT

The George Fisher deposit (107 Mt @ 11.1% Zn, 5.4% Pb, and 93g/t Ag) is the northernmost significant Mount Isa-style deposit hosted by the ~1653Ma Urquhart Shale in the Western Mount Isa Inlier. It is distinguished from the Mount Isa and Hilton Mines by a paucity of syn-late tectonic Cu. This has enabled recognition and examination of a previously unrecognized, syndiagenetic, hydrothermal Zn-Pb-Ag mineralization-system, despite superposition of intense deformation during the Diamantinan and Isan Orogenies.

George Fisher contains eleven west-dipping, stacked, anastomosing, stratabound ore lenses contained within rhythmically laminated pyritic siltstones intercalated with banded mudstones, and separated by barren stylolitic mudstones. The ore-bearing sequence contains abundant carbonate banding including partly coalesced carbonate nodules in pyritic siltstones and planar white carbonate bands in siltstones and banded mudstones. The deposit is zoned from stratigraphically lower Zn-rich to higher Zn+Pb-rich ore bodies. Subeconomic Cu occurrences are coincident with Zn+Pb zones, but are predominantly restricted to upper portions of the sequence. This zonation was developed within two hydrothermal systems separated by 75-125Ma.

Emplacement of Zn-Pb-Ag at George Fisher was the culmination of a complex, syndiagenetic, hydrothermal alteration system. Calcite is a major constituent of texturally distinct carbonate banding and its formation post-dates earliest dolomite-ferroan dolomite-ankerite alteration. At George Fisher, these carbonates are distinguished by unique stable isotope geochemistry within the Urquhart Shale ($\delta^{18}O$ = 17.1-18.5‰, $\delta^{13}C$=-4.1 to -1.7‰) and are enriched in $(Fe,Mn)CO_3$ relative to paragenetically equivalent carbonates located away from economic Zn-Pb-Ag. These carbonates formed during infiltration of warm, basin-derived fluids into cool sedimentary rocks, prior to stylolitization and at depths of a few hundred metres. Chemical zonation of early carbonates over 10-20km provides vectors for Zn-Pb-Ag-bearing fluid influx zones.

Pyritization by thermochemical sulphate reduction of *in situ* organic material post-dated stylolitization. Infiltrating fluids lacked ore metals at the time. Bedding-parallel carbonate±quartz±celsian-hyalophane-K-feldspar vein development was localized in the immediate vicinity of, preceded and structurally prepared the sequence for, economic Zn-

-Pb-Ag mineralization. Sphalerite, galena, hydrophlogopite and bitumen were codeposited. Bitumen reflectance data and mesophase textures constrain maximum temperatures of mineralization and peak thermal conditions during burial to 200°C. Metals were transported in slightly oxidized, near-neutral fluids. Sulphur was either sourced from a separate reduced fluid or was transported as sulphate in the same fluid. Metal precipitation occurred via fluid mixing or sulphate reduction. Much sphalerite is preserved in primary depositional sites whilst galena occurs in syn-late tectonic veins and breccias but retains its primary spatial association with sphalerite at deposit scale. Nineteen galena samples, from a range of paragenetic settings, display homogeneous Pb isotope compositions. A Pb-model age of ~1653 Ma is interpreted to reflect the timing of Zn-Pb-Ag mineralization.

Key characteristics of the syn-late tectonic Cu system include pyrrhotite, biotite-chlorite-dominant and ferroan dolomite-ferroan ankerite -dominant alteration. Phyllosilicates occur in stratabound lenses superimposed on Ba-K-feldspar alteration zones, whilst ferroan carbonate alteration is pervasive throughout the deposit hanging wall. These carbonates are texturally, chemically and isotopically ($\delta^{18}O$ = 13.0-17.3‰, $\delta^{13}C$=-4.6 to -1.3‰) distinct from syndiagenetic carbonates. Copper-bearing fluids had temperatures of 250-300°C based on phyllosilicate mineral stability relationships.

The temporal-spatial-temperature zonation of the Zn-Pb-Ag and Cu systems at George Fisher is not preserved at Mount Isa and Hilton. Mineralogical and geochemical characteristics of carbonate and phyllosilicate alteration assemblages throughout Zn-Pb-bearing strata at the latter deposits are products of syn-late-tectonic Cu mineralization, reflecting greater influx of Cu-bearing fluids at these sites. Poor preservation of syndiagenetic hydrothermal signatures at Mount Isa and Hilton has undoubtedly contributed significantly to the long-standing controversy surrounding the origin of Mount Isa-style Zn-Pb-Ag deposits.

DECLARATION

I declare that this thesis is my own work and has not been submitted in any form for another degree or diploma at any University or other institution of tertiary education. Information derived from the published or unpublished work of others have been acknowledged in the text and a list of references is given.

[redacted]

Lucy H. Chapman

31.8.99

31.8.99

STATEMENT OF ACCESS

I, the undersigned, the author of this thesis, understand that the following restriction placed by me on this thesis will not extend beyond the date specified.

"I wish to place restriction on access to this thesis for a period of two years."

After this period has elapsed I understand that James Cook University will make this thesis available for use within the University library and, by microfilm or other photographic means, allow access to users in other approved libraries. All users consulting this thesis will have to sign the following statement:

"In consulting this thesis I agree not to copy or closely paraphrase it in whole or in part without written consent of the author, and to make proper written acknowledgement for any assistance which I obtained from it."

[redacted]

Lucy H. Chapman

31.8.99

31.8.99

ACKNOWLEDGEMENTS

This PhD study was made possible through the inspiration of Dr Russell Myers and financial support of Mount Isa Mines Limited.

Alice Clark, Steve De Kruijff and Bob Dennis are thanked for support in their role as Chief Geologists during the period of this study. I am especially indebted to Dale Sims (Geology Team Leader - George Fisher Feasibility Study) for logistical aspects of project management in Mount Isa and for employment opportunites at George Fisher. Discussions with Alan Shaw were invaluable to developing the stratigraphic framework of this project. Shaun Versace is thanked for his outstanding efforts with respect to processing aspects of the MIM Ltd data base. My time spent in Mount Isa during the course of this PhD will always be remembered as some of the happiest times thanks to the friendship and support of Danielle Slade and her family and friends, Alan and Caroline Shaw and the MIMEX crew (then) residing at Barracks 45.

This project was initially designed and supervised by Russell Myers. I am indebted to Russell for introducing me to the concepts and range of processes implicit to the Mount Isa problem. Rowena Duckworth and Brett Davis are thanked for stepping in as cosupervisors, and in particular, for supervision on site in Mount Isa. The structural aspects of this study benefitted greatly as a result of Brett's supervision. Mark Hinman, Nick Oliver and Pat Williams are thanked for taking up supervisory roles during the latter stages of this PhD study and are further congratulated for lasting the distance. Discussions with Mark Hinman have been invaluable to the development of a range of concepts presented in this thesis. Nick Oliver is thanked for wide-ranging and enthusiastic discussions related to the Mount Isa problem and reviewing aspects of the thesis. Special thanks to Pat Williams for his indubitable critiques of numerous drafts, encouragement and realism (!).

Thanks also must go to the staff of the Advanced Analytical Centre, and in particular Sharon Ness, Kevin Blake and Chris Cuff. Tim Bell, Nikki Adshead-Bell, Graham Carr, Geoff Denton, Damien Foster, Paul Gammon, Geordie Mark, Matt Painter, Julie Richmond, Jackie Rotherham, Mike Rubenach, Peter Southgate and Roger Taylor are thanked for discussion on a variety of topics.

On a personal note, to my family and friends back home in Adelaide and here in Townsville; your love, untiring encouragement, and understanding have been my life-line and proved to be a huge source of motivation and inspiration. Thank you.

LIST OF ABBREVIATIONS

Alb - Albite
Ank - Ankerite
Bit - Bitumen
Bt - Biotite
Carb - Carbonate
Cal - Calcite
Chl - Chlorite
Cpy - Chalcopyrite
Cs - Celsian
Dol - Dolomite
Fe Dol - Ferroan dolomite
Fe Ank - Ferroan ankerite
Gn - Galena
Gpt - Graphite
Hphl - Hydrophlogopite
Hyl - Hyalophane
Kfs - K-Feldspar
Ms - Muscovite
Mt - Magnetite
Phg - Phengite
Phl - Phlogopite
Po - Pyrrhotite
Py - Pyrite
Py_s - Spheroidal pyrite
Py_b - Brassy pyrite
Py_y - Yellow pyrite
Sid - Siderite
Sp - Sphalerite

MM- Medium-bedded, stylolitic mudstone
BM - Banded Mudstone
CS - Rhythmically laminated carbonaceous siltstone
Nod - Nodular carbonate
PS - Rhythmically laminated pyritic siltstone
SM - Shaly banded mudstone
WB - Layer parallel white carbonate band

Drill hole number explanation:

e.g. J702WI#2
J - Easting on mine grid
702 - First 3 digits of northing on mine grid
W - Drilling direction to the west
I - Inclined drill hole (cf. D- decline, H- horizontal)
#2 - Second inclined drill hole with J702 collar position.

MSCODE Explanation

e.g. 951102
95 - year drilled (1995)
11 - month drilled (November)
02 - second hole for that month.

TABLE OF CONTENTS

PART B
EVOLUTION OF ZN-PB-AG AND CU MINERALIZATION AT THE GEORGE FISHER DEPOSIT, MOUNT ISA, AUSTRALIA.

INTRODUCTION

The Early to Middle Proterozoic sedimentary sequences of the western Mount Isa Inlier and McArthur Basin in Northern Australia contain some of the world's largest known sediment-hosted Zn-Pb-Ag deposits including the Mount Isa, Hilton, George Fisher, McArthur River (HYC), and recently discovered Century deposits.

The George Fisher deposit (107Mt @ 93g/t Ag, 5.4% Pb and 11.1% Zn) is one of the richest known *in situ* sedimentary-hosted Zn-Pb-Ag resources in the region. It is the northernmost ore deposit in the Mount Isa system, situated 2km north of Hilton Mine and 25km north of Mount Isa Mine. It is distinguished from the latter by a paucity of Cu.

The HYC deposit at McArthur River is hosted by dolostone and pyritic black shales of the Barney Creek Formation that were mildly affected by ductile deformation and metamorphism during the Isan Orogeny (e.g. Solomon and Groves, 1994, Hinman, 1995). The majority of workers agree that the Zn-Pb-Ag ores formed as an integral part of sediment deposition, although sedimentary-exhalative versus shallow, subsurface replacement models are debated (e.g. Gustafson and Williams, 1981; Hinman, 1996; Large et al., 1998). The relatively pristine setting of HYC ores, and similarity between general features of host rocks and stratiform mineralization at McArthur River and Mount Isa led to the promotion of McArthur River as an archetype of Northern Australian Proterozoic sediment-hosted Zn-Pb-Ag (e.g. Russell et al., 1981; Lambert, 1983; Legge and Lambert, 1994). This interpretation has been modified due to the recent discovery of the Century deposit and realization that the sulphide ore there was probably emplaced at significant depths late in the burial diagenetic history (Broadbent et al., 1998). It is now acknowledged that a diversity of processes operating at shallow to deep levels in the diagenetic environment were responsible for Zn-Pb-Ag mineralization in the region (for recent summary see Williams, 1998). However, there is no consensus surrounding the timing and origin of Mount Isa Zn-Pb-Ag and Cu ores. As a result, it is not clear whether this deposit is a member of the latter group of sediment-hosted deposits or a separate genetic style (e.g. McGoldrick and Large, 1998).

The genesis of Mount Isa-style Zn-Pb-Ag and its relationship to later-discovered Mount Isa-style Cu is amongst the major controversial topics of the 20th century in the field of economic geology. The Mount Isa mine is unique in that it represents the site of both giant accumulations of sediment-hosted Zn-Pb-Ag and Cu ores (e.g. Gustafson and Williams, 1981). Zinc-Pb-Ag ores are concordant, and banded at a millimetre- to centimetre-scale in a similar fashion to laminated pyritic and carbonaceous siltstone host rocks. Copper ores are disseminated and vein-hosted, contained within a dolomite-quartz alteration envelope and lie adjacent to Zn-Pb-Ag ore-bearing stratigraphy.

Earliest genetic models proposed that Zn-Pb-Ag accumulations were the product of replacement during tectonism and the banded nature of ore was a result of bedding-plane fluid infiltration (e.g. Grondijs and Schouten, 1937; Blanchard and Hall, 1942). This model was adapted to include Cu ores (e.g. Carter, 1953). However, numerous workers questioned the epigenetic hypothesis leading initially to the development of the synsedimentary-exhalative genetic model for sediment-hosted mineralization in the Mount Isa-McArthur region (e.g. Solomon, 1965; Finlow-Bates and Stumpfl, 1979; Russell et al., 1981). The turning point was the discovery of the HYC deposit which was considered to represent the undeformed and unmetamorphosed equivalent of Mount Isa (e.g. Legge and Lambert, 1994). Furthermore, a key basis of the sedimentary-exhalative interpretation was the assumption that fine-grained organic-rich host rocks at both localities were deposited in a deep water setting, that was probably anoxic or stratified, similar to modern seafloor sulphide deposits (e.g. Mathias and Clark, 1975; Large et al., 1998). Copper ores that distinguish Mount Isa were proposed to have deposited in a subsurface feeder-zone to Zn-Pb-Ag ore (Finlow-Bates and Stumpfl, 1979). Thus, the sedimentary-exhalative model accounted for the finely banded and concordant nature of Zn-Pb-Ag ore combined with vein-hosted Cu as part of a single ore-forming system.

More recently, sedimentological investigations of the depositional setting of the Urquhart Shale host rocks at Mount Isa identified features typical of shallow water to emergent depositional systems (e.g. Neudert and Russell, 1981). During the same period, a series

of structural, petrographic and geochemical studies of the Cu system resulted in a consensus that Cu was emplaced late in the tectonic history of the area (e.g. Perkins, 1984, Swager, 1985). Shallow to burial diagenetic emplacement models for Zn-Pb-Ag emerged from these developments (e.g. McGoldrick and Keays, 1990) that predominantly invoked separate origins of the two ore systems (e.g. Neudert, 1983, Heinrich et al., 1989). Recent dating of hydrothermal biotites accompanying Cu emplacement at Mount Isa have given ages of 1523Ma, some 125Ma years younger than deposition of the Urquhart Shale (Perkins et al., 1999). Most recent genetic modelling of the Mount Isa deposit favours the syntectonic and cogenetic interpretation of earliest workers (e.g. Perkins, 1997, see below).

Major sources of contention between proponents of the genetic models include the origin of finely layered sphalerite and galena that mimic the laminated nature of host sedimentary rocks, and the apparently stratiform nature of mineralized lenses at Mount Isa (e.g. Perkins, 1997). However, the genetic problem is magnified by the polydeformed and metamorphosed nature of the sequence and, in particular, the coincidence of zones of intense fold development and sulphide mineralization (e.g. Mathias and Clark, 1975). Syntectonic models of Zn-Pb-Ag mineralization have demonstrated late paragenetic and structural settings for sphalerite and galena and invoke the coincidence to be a product of enhanced fluid flow during deformation (e.g. Myers et al., 1996, Perkins and Bell, 1998). However, others have invoked deformation of preexisting sulphide-rich layers and proposed synsedimentary-diagenetic models (e.g. McClay, 1982, Valenta, 1994).

The recently delineated George Fisher deposit represents a key addition to the group of sediment-hosted deposits in Northern Australia, as it provides an opportunity to address the controversy surrounding Mount Isa-style Zn-Pb-Ag and Cu within a Cu-poor portion of the system, and thus, further our understanding of the complex metallogenesis of the Mount Isa-McArthur region as a whole. The aim of this PhD study is to document and place constraints on the genesis of Zn-Pb-Ag ore at the previously undescribed George Fisher deposit.

THESIS STRUCTURE

This thesis is presented as three separate parts written in extended paper format, with the assumption that they are read in sequence.

The main objective of Part A is to describe the geological setting, and constrain the relative timing of Zn-Pb-Ag mineralization. It includes a description of the regional and local geological setting of the deposit, and details deposit-scale geological features with emphasis on the nature of the host rocks of the ores, and the structural and textural setting of sulphides and their distribution.

A detailed paragenetic study is presented in Part B, and is complemented by analysis of metal distribution patterns and lead and sulphur isotope geochemical characterization of Zn-Pb ore. Constraints on the temperature of formation of Zn-Pb sulphides are derived from bitumen reflectance data and illustrate that previous interpretations of the thermal history of the Urquhart Shale require significant reinterpretation. The model for Zn-Pb-Ag mineralization is refined as a consequence of these data.

The first comprehensive textural and geochemical study of carbonate constituents of the Urquhart Shale throughout the Mount Isa mineralization system is presented in Part C. An SEM study of the textural evolution of carbonates at George Fisher, coupled with over 300 microprobe analyses, and carbon and oxygen isotope geochemistry reveals three carbonate populations. Textural, chemical and isotopic characterization of these distinctive carbonates provides evidence for a previously-unrecognized diagenetic hydrothermal system. Comparisons are made with carbonates from the Hilton and Mount Isa deposits, and from sites peripheral to economic accumulations of Zn-Pb-Ag and Cu. Variations in carbonate constituents of the deposits in the Mount Isa system are interpreted as reflections of variable superposition of separate Zn-Pb-Ag and Cu hydrothermal systems.

PART A

GEOLOGY, SETTING AND MINERALIZATION STYLES OF THE GEORGE FISHER ZN-PB-AG DEPOSIT, MOUNT ISA, AUSTRALIA.

ABSTRACT

The George Fisher deposit contains one of the world's largest *in situ* Zn resources (107Mt @ 93 g/t Ag, 5.4% Pb and 11.1% Zn). It is situated 25km north of Mount Isa and hosted by the ~1653Ma Urquhart Shale in the Western Fold Belt of the Mount Isa Inlier. The nature and distribution of Zn-Pb-Ag sulphides and metal-structural associations point towards a syndiagenetic timing for Mount Isa-style mineralization, followed by a protracted history of regional folding.

Economic Zn-Pb-Ag mineralization is hosted by rhythmically laminated pyritic siltstones and separated by barren dolomitic and calcitic mudstones. Two styles of carbonate banding also typify the sequence. Carbonates occur as the major constituent of anastomosing and displacive nodular layers that occur specifically in rhythmically laminated pyritic siltstones, and also as layer-parallel, millimetre-thick bands interbedded with all units except medium-bedded mudstones.

Eleven mineralized stratigraphic intervals have been identified in which sulphides occur as stratabound lenses that subparallel bedding, bifurcate, and pinch out along the extent of the main economic zone. Mineralization styles represented in each interval include stratiform sphalerite-dominant, stratabound sphalerite-dominant and stratabound galena-rich styles. Stratabound styles include vein- and breccia-hosted varieties and volumetrically constitute the bulk of ore at the deposit. Stratiform sphalerite mineralization styles are dominated by finely layered, rhythmically laminated siltstone-hosted sphalerite and nodular carbonate-hosted sphalerite. Stratiform styles are spatially associated with stratabound mineralization styles but alone, do not contain economic Zn-Pb-Ag grades.

The predominance of vein- and breccia-hosted sulphides, and bedding parallelism exhibited by stratabound styles indicates that ore-forming fluids were introduced via fluid conduits that were preferentially developed subparallel to bedding in an at least semiconsolidated sedimentary pile.

Stratiform sphalerite is interpreted to be the product of bedding-subparallel fluid migration. Its enveloping surface is discordant to bedding and cross-cuts chronostratigraphic marker horizons. This mimics relationships recorded at meso- and microscales and can not have been produced by exhalation. The diversity of sphalerite-dominant mineralization styles is interpreted to be essentially due to variation in permeability and porosity of host layers. Stratiform styles are believed to be hosted by units which had low permeability and porosity compared with bedding-parallel fractures. Fluid flow was thus preferentially channelled along fractures rather than sedimentary fabrics.

Medium to coarse-grained vein- and breccia-hosted sphalerite and galena styles are abundant to the south whereas stratigraphically equivalent ore lenses to the north consist predominantly of stratabound, fine-grained sphalerite and galena breccias. The continuity of ore lenses discounts the possibility that this zonation is the product of separately developed structural fluid channelways. However, zoning does correspond with increased small-scale fold development from south to north in the deposit. Fine-grained breccias are characterized, not only by a relative decrease in sulphide grain size, but also by rounded breccia clasts with preferred orientation. These features are typical of mechanically deformed sulphides and suggests that the breccia style zonation pattern results from heterogeneous post-mineralization strain. Sphalerite breccia-veins were introduced prior to the regional D_1 event and onset of regional folding whilst fine-grained sphalerite breccias lie in regional D_3 structural sites and provide further evidence of sulphide deformation and mobilization.

Comparison of the stratigraphic sequence at Mount Isa, Hilton and George Fisher

illustrates that all three deposits are situated within a portion of the stratigraphy characterized by the presence of barren, medium-bedded mudstones that separate rhythmically laminated pyritic siltstone intervals. However, George Fisher is shale-poor compared to Mount Isa where carbonate banding is rare. Furthermore, the number and thickness of medium-bedded mudstones varies between deposits indicating that depositional conditions differed at each locality. Therefore, although there was a profound bedding-control on mineralization at all three deposits, this does not appear to have been a direct product of sedimentation. It is proposed that primary Zn-Pb mineralization at all of these deposits occurred in sites of greatest rheological heterogeneity produced by large- and fine-scale bedding variations which enabled infiltration of large volumes of metal-bearing fluids.

INTRODUCTION

The world class Mount Isa, Hilton and George Fisher deposits are hosted by the Urquhart Shale of the Mount Isa Group within the Western Fold Belt of the Proterozoic Mount Isa Inlier (Fig. 1). George Fisher (107Mt @ 93 g/t Ag, 5.4% Pb and 11.1% Zn), situated 25km north of Mount Isa and 2km north of Hilton, represents the northern extent of known economic sulphides. Combined, these deposits represent one of the world's largest accumulations of sediment-hosted base metal mineralization and yet the origin of the ores is controversial. Synsedimentary-exhalative, syndiagenetic and syntectonic models, that span a geological time frame of ca. 150Ma have been proposed for the origin of Mount Isa-style mineralization (e.g. Finlow-Bates and Stumpfl, 1979; McGoldrick and Keays, 1990; Valenta, 1994; Perkins, 1997.)

Zn-Pb-Ag sulphides at George Fisher occur as stacked, stratabound lenses hosted by pyritic siltstones, which is also the case at the Mount Isa and Hilton deposits. However, the deposit is distinguished from Hilton and Mount Isa on the basis of sedimentological characteristics and metal content. It is the shale-poor and Zn-rich end-member of the set of deposits. George Fisher can be further distinguished by the paucity of syn-late tectonic

vein- or breccia-hosted Cu mineralization and associated silica-dolomite alteration and brecciation (cf. Perkins, 1990).

This paper presents a geological model for the previously undescribed George Fisher deposit. It includes descriptions of the Urquhart Shale, analysis of mineralization styles on the basis of sedimentological, mineralogical and structural associations, and effects a comparison with the Mount Isa and Hilton deposits. A syndiagenetic timing for Zn-Pb-Ag mineralization at George Fisher is proposed in light of these data.

REGIONAL GEOLOGICAL SETTING

The Mount Isa Inlier and McArthur Basin in northwest Australia represent the remnants of an intracontinental extensional basin system (Fig. 1) that was active from about 1800 to 1600Ma (Blake, 1987; Etheridge and Wall, 1994). Stratigraphic correlations can be made between the two basin systems, however it is likely that they were separated by an elevated portion of basement rock (represented by the Murphy Inlier) during basin development (e.g. Jackson et al., 1998).

The sedimentary succession in the McArthur area is essentially unmetamorphosed and weakly deformed whilst much of the Mt Isa Inlier has been subjected to metamorphism and intense deformation associated with the Isan Orogeny. As a result, the Mt Isa Inlier is subdivided into three broad tectonic units including the Eastern and Western Fold Belts (Carter et al., 1961) and intervening Kalkadoon-Leichhardt Belt (Blake and Stewart, 1992). These are further subdivided into tectonostratigraphic zones (Fig. 1) based on variable structural, metamorphic and geophysical characteristics (Blake et al., 1990).

Three major Proterozoic sequences have generally been recognized in the Mt Isa Inlier and all overlie older volcano-sedimentary basement rocks. These cover sequences (designated 1, 2 and 3) are associated with discrete episodes of rifting and post-rift subsidence (Blake, 1987) (Fig. 2). It is generally accepted that the majority of the volcano-

sedimentary basement rocks were deposited in an NNW-SSE intracratonic extensional basin system which was deformed and metamorphosed during the Barramundi Orogeny around 1870 Ma (Etheridge and Wall, 1994).

Recent investigations suggest a complex tectonostratigraphic history for the Mount Isa Inlier. McDonald et al. (1997) have proposed that igneous and metamorphic basement complexes of Late Archean to Early Proterozoic age south of Mount Isa were associated with subduction rather than intracratonic processes. O'Dea et al., (1997) identified a regional unconformity within Cover Sequence 3 of Blake (1987) and thus proposed a further subdivision of the Sequence into two discrete rift and sag cycles that they termed cover sequences 3 and 4 (Fig. 2). In their interpretation, Cover Sequences 1 and 2 are equivalent to those of Blake (1987).

Cover sequence 1 consists predominantly of felsic volcanic rocks that are exposed within the Kalkadoon-Leichardt Belt and associated with contemporaneous granitic intrusions that formed around 1875 to 1850 Ma (Blake et al., 1990; Page and Sweet, 1998). It is possible that extensive igneous activity at this time was linked to the termination of the earlier extensional basin sequence (Blake et al., 1990). Cover sequence 2 consists predominantly of sedimentary and bimodal volcanic rocks which were deposited around 1790 to 1740 Ma (O'Dea et al., 1997), probably in association with (N)NE-(S)SW extension during the Leichardt Event of Etheridge and Wall (1994). Rocks of this age are exposed in the Eastern Fold Belt and Leichardt River Fault Trough of the Western Fold Belt.

Cover sequence 3 of Blake (1987) is characterized by abundant fine-grained carbonate and siliciclastic sedimentary rocks with minor bimodal volcanic rocks. These include the Mount Isa and McNamara Groups exposed in the Leichardt River Fault Trough and Lawn Hill Platform respectively, in the Western Fold Belt, and Fullarton River and Soldiers Cap Groups in the Eastern Fold Belt (Page and Sun, 1998), all of which host economically significant occurrences of base metals (Figs 1 and 2). Basin development

around this time was the product of predominantly N-S extension during the McArthur Event and was associated with extensive thermal subsidence after 1670Ma (Etheridge and Wall, 1994). SHRIMP U-Pb age dates from zircons obtained by Page and Sweet (1998) indicate that this sedimentary sequence spans a time frame from approximately 1710 to 1595 Ma consistent with the complex basin history proposed by O'Dea et al., (1997).

Basin development during the McArthur Event was culminated by the onset of the Diamantina Orogeny, one of two major orogenic events to have affected the Mount Isa Inlier (e.g. MacCready et al., 1998). Three major deformation episodes (denoted D_1 , D_2 and D_3) were associated with these orogenic events, and are variably expressed across the Mt Isa Inlier (Bell, 1983). The onset of the Diamantina Orogeny has been placed around 1610 to 1590 Ma (Page and Bell, 1986, Page et al., 1994) for D_1 north-south thrusting. The second major deformation episode marks the onset of the Isan orogeny (e.g. Bell and Hickey, 1998). D_2 produced steeply dipping folds with N-S trending axial planes during east-west compression around 1537±7Ma (Page et al., 1994). Further east-west compression around 1510±13Ma (Page and Bell, 1986) resulted in the reactivation of D_2 folds and the local development of D_3 steeply dipping, N-S trending folds. Peak metamorphism is generally considered to have been coincident with the D_2 event (e.g. Connors and Page, 1995) although there is evidence of a thermal event in the southeastern Mt Isa Inlier at 1584 Ma which appears to have been associated with D_1 (Page and Sun, 1998).

Bell and Hickey (1998) presented evidence for north-south compression between D_2 and D_3. Effects of this event, $D_{2.5}$, are pronounced in the Mount Isa area where they are associated with the development of micro- to macroscopic fold structures associated with the rotation of D_2 axial planes into subhorizontal orientations. These structures lack a mesoscopic foliation, however, they are overprinted by D_3 folds and associated S_3 cleavage.

LOCAL GEOLOGICAL SETTING

The George Fisher, Hilton and Mount Isa deposits occur along a 25km strike length of Urquhart Shale Formation of the Mount Isa Group (Cover Sequence 4). The Mount Isa Group consists of basal quartzites overlain by a sequence of fine-grained siliceous, carbonaceous, tuffaceous and dolomitic siltstones and shales that unconformably overlie sandstones, quartzites and metabasalts of the Haslingden Group of Cover Sequence 2 (Neudert, 1983; Domagala et al., 1998: Figs 3 and 4). Uranium-Pb SHRIMP results obtained from zircons in tuffaceous beds of the Mount Isa Group at Mount Isa and Hilton Mines provide depositional ages of the Urquhart Shale of 1652±7Ma and 1654±5Ma respectively (Page and Sweet, 1998).

Earliest workers proposed that the fine-grained and carbonaceous nature of the Mount Isa Group was the product of deep water sedimentation (e.g. Mathias and Clark, 1975). However, the recognition of features including nodular and discoidal sulphate pseudomorphs and carbonate crusts in the Urquhart Shale, and halite casts and stromatolites in the Upper Mount Isa Group has led to the general consensus that hypersaline and semi-emergent conditions were periodic during deposition of the sedimentary sequence (McClay and Carlisle, 1978; Neudert and Russell, 1981; Neudert, 1983). A comprehensive study of the Mount Isa Group as a whole is presented in Neudert (1983) who interpreted the entire sequence to represent an ancient saline lake complex (Neudert, 1986).

Mount Isa Group rocks crop out in a north-south trending, west-dipping zone that lies on the western limb of a regional D_2 anticline in the Mount Isa area (Winsor, 1986). The sedimentary package as a whole is some 4000+m thick but decreases in thickness northwards, across the Transmitter Fault, and some elements are missing as a result of abundant cross-cutting faults in the Hilton area (Valenta, 1994: e.g. Figs 3 and 4). The upper formations of the Mount Isa Group are truncated to the west by the Paroo and Mount Isa faults and variably fault-bounded to the east (Fig. 3).

Metamorphic grade increases from biotite to sillimanite-K-feldspar zone towards the Sybella batholith, west of the Mount Isa and Paroo fault zones. The Sybella batholith was emplaced at 1660±4 Ma to 1655±5 Ma (Connors and Page, 1995). The Mount Isa Group form a N-S corridor of lower grade sedimentary rocks (Rubenach, 1992). A peak metamorphic temperature of 330°C has been estimated for the formation of phlogopite+calcite within the Mount Isa mine environment (Waring, 1990b) and studies of organic matter from ore zones suggest that temperatures exceeded that required for hydrocarbon generation (Saxby and Stephens, 1973, Saxby, 1981).

Recent studies of the deformation history in the Mount Isa area have been undertaken by Bell (1983), Winsor (1986), Bell et al. (1988), Valenta (1994) and Bell and Hickey (1998). The major regional deformation events (including $D_{2.5}$) are recognized in the area but variably developed from Mount Isa to Hilton and George Fisher (Table 1). The effects of D_1 thrusting are most pronounced in the Lake Moondarra area and include the development of an E-W trending near vertical foliation (Winsor, 1986) whilst the oldest fabric developed in the Hilton area is a bedding parallel cleavage that is stylolitic in nature and thus may have formed earlier and during compaction of the Mount Isa Group (Valenta, 1994). D_2 produced a penetrative cleavage subparallel to bedding in most of the region and is associated with the development of abundant folds and faulting in the Hilton area (Valenta, 1994). In contrast, D_3 folds associated with a penetrative cleavage are widespread at Mount Isa Mine (Bell et al., 1988) but only locally developed at Hilton (Valenta, 1994). Rotation of D_2 folds by $D_{2.5}$ has been recorded locally at a mesoscopic scale in underground exposure at Mount Isa, Hilton (Bell and Hickey, 1998) and George Fisher (see below). The major manifestation of post-D_3 deformation in the mine environments is brittle faulting that was associated with the reactivation of Paroo and Mount Isa faults (e.g. Valenta, 1994). The Paroo Fault is interpreted to have formed during D1 thrusting (e.g Bell, 1983). The Mount Isa Fault was active during D_2 and final reverse movement on this fault, which juxtaposed higher metamorphic grade sedimentary rocks of Cover Sequence 2 and Mount Isa Group sedimentary rocks, is constrained to have occurred after 1460Ma (Perkins et al., 1999).

DEPOSIT GEOLOGY

George Fisher is separated from the Hilton Mine by approximately 1.5km of stratigraphically older Urquhart Shale due to offset on the Gidyea Creek Fault (Fig. 4). Mineralization at George Fisher extends from the Gidyea Creek Fault in the south to the Spring Creek Fault in the north (Fig. 4). Several ferruginous, limonitic siltstone and chert ridges bearing minor cerrusite and smithsonite outcrop at the surface and the deposit has been partially oxidized to a depth of about 250m (Mullens, 1993).

The presence of Zn-rich mineralization within the vicinity of George Fisher has been known of since the 1940's (e.g. Blainey, 1960). However, the site was not deemed potentially economic until the 1980's during which time several surface drilling projects were undertaken by Mount Isa Mines Ltd. An underground feasibility study was undertaken from 1995 to 1997 which included the development of an underground drive from Hilton Mine, that accessed George Fisher at the eastern edge of the ore-bearing sequence on 12 level (Figs 5 and 6). A series of 40m- to 80m-spaced drill fans were drilled out from 6900mN to 8200mN and collared along this drive. The bulk of the data presented in this paper are derived from diamond drill core produced during the underground feasibility study (Fig. 5). Mine development commenced at George Fisher in mid-1998, 50 years after the first drill hole.

GENERAL OREBODY FEATURES

The bulk of economic mineralization at the George Fisher deposit occurs within a 350m thick stratigraphic package and extends over a strike length of 1.2 km to a known depth of approximately 1 km (Mullens, 1990). Economic mineralization is truncated at depth to the west by the Hanging Wall Fault and to the south by the Gidyea Creek Fault (Figs 5 and 6). Furthermore, the orebodies are segmented into a series of N-S trending blocks with maximum lengths of about 100m by a prominent set of post-D_3, NE-SW to NNE-SSW faults (see below).

The George Fisher deposit contains eleven mineralized stratigraphic intervals which occur as stacked stratabound lenses hosted by laminated pyritic siltstones and separated by barren mudstones (Fig. 7). Mineralized stratigraphic intervals are named 1, 2 and A to I, from stratigraphically youngest to oldest and a significant portion of the ore reserve is contained within the C and D orebodies (58Mt @ 111g/t Ag, 5.9% Pb and 10.7% Zn, Aldroyd, 1998). Each interval can be distinguished by distinctive bedding permutations and tuffaceous marker beds which has enabled detailed stratigraphic correlation throughout the ore-bearing sequence.

Economic sulphide mineralization consists predominantly of sphalerite and galena. Minor native silver and rare tetrahedrite have been identified during this study. Chalcopyrite is the major contributor to subeconomic levels of Cu mineralization at the deposit. Gangue minerals include pyrite, pyrrhotite, calcite, variably ferroan dolomite and ankerite, K-feldspar, hyalophane, hydrophlogopite, quartz, phengitic muscovite, biotite and chlorite, with minor to rare bitumen, magnetite and stilpnomelane. Several individual orebodies can be distinguished on the basis of metal and gangue mineral assemblages (Fig. 7).

The orebodies are disrupted by a series of late-stage brittle faults including the J75 and L70 fault-types (Fig. 5). The J75 fault is an E-W dip slip fault with less than 5m of displacement, although drill hole fault intersections of up to several metres have been recorded (Jones, 1996). These faults are characterized by coarse carbonate ± quartz ± sphalerite fill. The later-stage L70-type fault system consists of a series of NE-SW to NNE-SSW strike slip faults that displace stratigraphy by up to 70m (Jones, 1996). These are anastomosing and splayed and represented by centimetre-thick graphitic gouges and pink calcite-fluorite-pyrite±sphalerite fill. The J75 fault is interpreted to be of D_3 age and is cross-cut by the L70 fault-types in underground exposure (Jones, 1996).

A 10-100cm thick bedding-parallel structure can be mapped in drill core in the southeastern end of the deposit (Fig. 5). It is variably filled by calcite, pyrite, sphalerite, quartz, bitumen and dolomite, which exhibit complex overprinting relationships and

probably represent infill formed during multiple generations of fluid influx. The timing of earliest infill in this structure is poorly constrained. However, the presence of folded contacts suggests that it may have developed prior to D_2 and peak metamorphism.

HOST ROCKS

The following subdivision of the Urquhart Shale at George Fisher is based on drill core relationships and augmented by thin section petrology and whole rock XRD analyses (Appendices I, II and III). Five major rock types and two styles of carbonate banding have been identified. Carbonate bands are included as independent mappable features in this classification scheme. Their origin is discussed in Part C of this thesis.

MUDSTONE VARIETIES

Medium-bedded, stylolitic mudstones (MM): Medium-bedded mudstones are typically 5 to 15m thick and consist of 5-10cm thick discontinuously or planar laminated, cross-bedded or massive bedding intervals (e.g. Figs 8 and 9a). Internal structures are poorly preserved in general and defined by diffuse carbonaceous material whilst bedding-parallel carbonaceous stylolites are a common feature of this rock-type. Mudstones are grey to light grey in hand specimen and consist of an anhedral mosaic of clay- to medium silt-sized carbonate and quartz grains. Mica and K-feldspar are accessory mineral components. The dominant carbonate constituent varies from dolomitic (typically 50-60%) to calcite (50-90%). Calcite-rich zones are typically coarser-grained and light grey or bleached in appearance. They vary from a few centimetres- to metres-thick, and are discontinuous. Medium-bedded mudstones can be correlated across the extent of the deposit, retain a consistent unit thickness and have a sheet-like morphology (Fig. 8). These mudstones typically have sharp contacts with most other rock types (e.g. Fig. 9a).

Banded mudstones (BM): Banded mudstones vary in thickness from 2 to 4 m and consist of interbedded, thin to medium-bedded, massive, finely laminated or graded, grey to dark grey, dolomitic or calcareous beds. The alternation of light grey, calcitic and dark grey

dolomitic beds on a centimetre-scale is a distinctive feature of several banded mudstone intervals (Fig. 9b and 9c). Massive beds make up more than 50% of this rock-type and commonly contain sub-mm thick and millimetre-long, discontinuous fleck-like carbonaceous seams. Bedding contacts vary from sharp and planar to irregular and stylolitic. Beds typically consist of 50 - 80% detrital quartz, 20-40% calcite or dolomite, 5-10% white mica and < 5% K-feldspar and plagioclase (Appendix III). Mineral constituents are typically clay- to fine silt-sized and form anhedral grain mosaics with abundant interpenetrative and sutured grain contacts. Banded mudstones form continuous sheet-like bodies and discontinuous elongate lenses (Fig. 8) and in some cases display metre-scale gradational contacts with most other rock types.

Shaly banded mudstones (SM): This rock-type is restricted to the I and H stratigraphic intervals at the George Fisher deposit (Fig. 8). Shaly banded mudstones contain the same bed-types as banded mudstones but are distinguished from the latter by the presence of centimetre to 10cm thick, planar laminated to massive black shales interbedded with 1-3cm thick, fine planar laminated shaly siltstone beds which preserve rare small-scale ripples and cross beds (Fig. 9d). Shales and shaly siltstones are similar in composition to banded mudstones but distinguished by the coarser-grained nature of detrital quartz and carbonate grains. Beds typically consist of 40-70% carbonate (calcite and/or dolomite), 20-50% quartz, less than 10% mica and feldspar, and accessory diffuse bituminous material and spheroidal pyrite. Shaly banded mudstones are typically less than 2m thick, are characterized by at least 30% shaly interbeds and occur as 10 to 100m long lensoidal and sheet-like bodies typically adjacent to, or contained within banded mudstone intervals.

SILTSTONE VARIETIES

Rhythmically laminated carbonaceous siltstones (CS): This siltstone variety consists of sub-mm thick, alternating light grey and dark grey wavy laminae and intermittent light-grey millimetre-thick planar laminations at a hand specimen scale (Fig. 9e and f). This rock type consists of similar proportions of fine to medium silt-sized, anhedral carbonate

(typically dolomitic), and medium to coarse silt-sized, subrounded and oval to blocky and angular quartz grains. Dark wavy laminations are characterized by abundant diffuse bituminous material which occurs interstitial to carbonate-quartz grains, but predominantly as diffuse to concentrated residues along discontinuous and anastomosing, wispy dissolution seams. Light grey planar laminae are distinguished by a greater abundance of coarse silt-sized detrital quartz and their continuous nature (Fig. 9f). Non-pyritic siltstones of this type are uncommon at George Fisher. They occur as centimetre-thick intervals sparsely and discontinuously distributed throughout banded mudstones, except in the B stratigraphic sequence where 10-50cm thick units consistently occur within a 3m interval (Fig. 8).

Rhythmically laminated pyritic siltstones (PS): The most common siltstone type at the deposit is similar to rhythmically laminated carbonaceous siltstones. Rhythmically laminated pyritic siltstones are characterized by the presence of fine-grained, spheroidal pyrite in carbonaceous laminae (Fig. 9d). This form of pyrite typically constitutes 15 to 45% of the whole rock. Rhythmically laminated pyritic siltstones occur as 1 to 5m thick sheet-like intervals in sharp contact with mudstones (Fig. 9a). They also occur as centimetre to 10's of centimetre-thick beds intercalated with banded mudstones over several metres. These mixed pyritic siltstone and banded mudstone intervals represent zones gradational between the two end-member rock types and are common throughout the sedimentary sequence at George Fisher (Fig. 8 and 9g). The proportion of spheroidal pyrite in pyritic siltstones within these zones, and the relative proportion of pyritic siltstones to banded mudstones varies along strike.

CHRONOSTRATIGRAPHIC MARKER BEDS

Numerous *tuffaceous marker beds* are present throughout the sequence (Fig. 7). Individual markers can be characterized by features including thickness, colour and host rocks. They can be distinguished from mudstones by their cherty appearance and tendency to cross-fracture. Tuffaceous marker beds occur interbedded with plain and pyritic laminated siltstones.

NATURE AND DISTRIBUTION OF CARBONATE BANDS

Nodular carbonate (Nod): White, fine to medium-grained carbonate (calcite or dolomite) is the dominant constituent of wavy and anastomosing, millimetre- to centimetre-thick, nodular layers that lie subparallel to, and are interwoven specifically with laminated pyritic siltstones (Fig. 9b and h). Nodular carbonate layers have not been recorded in non-pyritic laminated siltstone intervals. Contacts between nodular carbonate layers and pyritic siltstones are typically sharp at hand specimen scale, and stylolitic. The proportion of nodular carbonate layers in rhythmically laminated pyritic siltstones varies from minor to 40% by volume with considerable along-strike variation in thin pyritic siltstone intervals (Fig. 8). However, in thick pyritic siltstone intervals such as the H footwall and hanging wall ore zones which contain 20-30% nodular carbonate, the proportion of nodular carbonate is relatively consistent along strike. The enveloping surfaces of nodular carbonate occurrences in these zones are typically parallel to chronostratigraphic marker horizons. However, the distribution of nodular carbonate is highly variable along strike in mixed mudstone-pyritic siltstone intervals, and discordant to tuff marker beds (Fig. 8).

Layer-parallel white carbonate bands (WB): Bands of this type are 0.3-1.0cm thick, and consist of fine to medium-grained calcite or dolomite similar to that in nodular layers (Fig. 9i). White carbonate bands display sharp planar, stylolitic, and diffuse contacts with overlying and underlying beds which are locally discordant and are spatially associated with calcite nodules (Fig. 9c and j).

White carbonate bands display a range of associations with banded mudstones, rhythmically laminated pyritic siltstones and nodular carbonate layers. Some occur as solitary layers that are bounded by thin-bedded mudstones or underlie pyritic siltstones. Other white beds are coupled with homogeneous grey mudstones of similar thickness in banded mudstone intervals. These commonly occur sequentially in stacks consisting of 2 to 10 couplets separated by thin-bedded mudstones, over several centimetres and in zones up to 2m thick (Fig. 9j). A further association (termed a triplet after Clark, 1993) consists of a thin grey mudstone bed, overlain by a white carbonate band which is then overlain by

a rhythmically laminated pyritic siltstone (Fig. 9d and h). The laminated pyritic siltstone component may vary in thickness from 1 to several 10's of centimetres, but is typically 1-3cm thick. These pyritic siltstones also commonly contain interlayered nodular carbonate. Triplets also in part occur in repetitious stacks over centimetres to several metres. They are abundant in mixed pyritic siltstone and banded mudstone intervals, and are commonly developed peripherally to thick pyritic siltstone intervals (Fig. 8 and 9b).

Centimetre- to metre-thick intervals characterized by abundant white carbonate bands, intercalated with banded mudstones and rhythmically laminated pyritic siltstones can be mapped over 800m of strike length at George Fisher. However, white bands are also laterally discontinuous and in some instances this discontinuity mimics the distribution of nodular carbonate layers (e.g. Fig. 8a). The boundaries of continuous white band-bearing intervals lie parallel to tuffaceous marker beds whereas the distribution of less continuous zones transgresses stratigraphy at a low angle in a similar fashion to nodular carbonate distribution (Fig. 8).

STRUCTURAL GEOLOGY

The main objective of this preliminary structural study was to establish the number, sequence and style of deformation events. The methods used include:

1. Meso- to macroscale structural interpretation of drill fans J702, J718, J730 and K820 utilizing diamond drill core data from MIM Ltd and based on bedding to core axis angles in unoriented core, identification of hinge zones in core, and interpretation of enveloping surfaces defined by continuous sedimentary units.
2. Meso- to microscale interpretation, of the C ore zone, based on generalized underground mapping of the 7200mN cross-cut (Fig. 5) and analysis of oriented hand samples and thin sections collected within this ore zone. The C ore zone was selected for detailed analysis as it contained the widest variety of fold styles. Underground mapping and sample collection was limited by underground access.

Mesoscale observations for other ore zones in the cross-cut are augmented by MIM Ltd data.

MACROSCOPIC STRUCTURAL FEATURES

Four interpreted cross-sections are presented and illustrate the distribution of major rock types and an interpretation of macroscopic structural elements (Fig. 10). In general, the enveloping surfaces defined by the contacts of bedding units are parallel and exhibit variable dips from 30° to 80°W with small domains characterized by near-vertical to steeply east-dipping enveloping surfaces. Bedding steepens towards the hanging wall fault zone on all sections studied. There is also an apparent consistent decrease in the dip of the easternmost bedding envelopes northwards through the deposit (Fig. 10). This could indicate the presence of a north-plunging fold hinge immediately east of the ore-bearing sequence.

Two dominant styles of folding have been recognized at a macroscopic scale based on the identification of hinge zones in drill core and variation in bedding attitudes. Open folds with gently east-dipping axial planes are prominent on cross section 7020mN. However, the most common fold style that is locally developed on all studied sections consists of tight, east-verging upright folds. Folds of this type are developed at a macroscopic scale in the central portions of all sections but are most prominent to the north on cross section 7820mN (Fig. 10). Increased intensity of small-scale fold development characterizes cross-section 7820mN and is coincident with a change of bedding attitude that could be either the product of another fold event heterogeneously developed on a deposit-scale, or indicate a closer proximity to the hinge region of a large-scale fold east of the sections.

MESO- AND MICROSCOPIC DEFORMATION EFFECTS

A range of contrasting fold styles are heterogeneously developed in underground exposures. Thick mudstone intervals rarely exhibit mesoscale folds, and poorly mineralized pyritic siltstone intervals contain minor mesoscale folding. However, a variety of fold styles are coincident with Zn-Pb horizons in orebody intervals (e.g. Fig.

11). Thus, deformation intensity appears to be directly related to economic sulphide content. At least four deformation events have been identified in the C ore zone (Table 2.)

The earliest deformation event to have affected the studied samples (denoted D_1) produced a bedding parallel foliation that manifests itself as anastomosing and penetrative, carbonaceous seams in mudstones and as a slaty cleavage in rhythmically laminated pyritic siltstones (Fig. 12a and b). These fabrics are affected by the earliest mine scale folds.

Abundant millimetre- to centimetre-thick bedding parallel veins also formed early in the deformation history. They are symmetrically infilled by fibrous, medium to coarse-grained quartz-K-feldspar-carbonate along vein walls followed by irregular aggregates of sphalerite ± euhedral pyrite ± hydrophlogopite infill central to the vein (Fig. 12b). Features that indicate deformation of these veins includes the crenulate nature of vein margins, boudinage of ultra-fine veins and foliation intensification along vein margins (Fig. 12 a-c). Evidence of deformation at a grain scale includes strong undulose extinction displayed by quartz and carbonate, kinked hydrophlogopite laths, and development of serrated grain boundaries. These deformation effects are evident in veins that are folded by the earliest known fold generation. Hydrophlogopite laths within the vein lie partly subparallel to S_1 developed in adjacent mudstone layers which indicates that mineral growth, and thus vein development, may have been synchronous with D_1 fabric development (Fig. 12b). and therefore prior to fold development.

D_2 produced upright, tight to isoclinal, east-verging asymmetrically folds with N-S trending axial planes that vary in amplitude from 1-2m and are the dominant fold-style in underground exposure (e.g. Fig 11). A crenulation cleavage is developed in F_2 hinge zones. However, in limbs of D_2 folds, S_1 and S_2 are typically parallel producing an intense composite S_{1-2} fabric subparallel to bedding (Fig. 12d, 13). These structures are overprinted by the effects of a third deformation event, D_3, that produced N-S trending, tight to isoclinal folds with subhorizontal axial planes (Fig. 13). Folds of this type vary

from a few centimetres to metres in amplitude and are prominent in the C ore zone exposure. This deformation event appears to have been responsible for the rotation of F_2 folds into inclined and subhorizontal orientations (Fig. 11 and 14a). Abundant fibrous quartz-carbonate veins were produced during D_3 (Fig. 14b).

A fourth deformation event, D_4, was associated with the local development of small-scale, tight, subvertical to upright, NNW-SSE to NW-SE trending folds with a locally intense axial planar foliation (Fig. 13). D_4 folds are superimposed on composite D_2/D_3 fold structures forming complex refold patterns (Fig. 14c). Several styles of veining accompanied fold development and include quartz-carbonate fibre veins in fold hinges and carbonate-±chlorite±pyrite±sphalerite veins that are folded by and cross-cut D_4 folds (Fig. 13). However, the most common feature is a NW-SE to NE-SW trending conjugate vein set infilled by galena±carbonate±sphalerite that cross-cut flat-lying folds (Figs 14a, b and c) Veins of this type are typically tapered and continuous with fine-grained bedding-parallel breccias that consist of a fine-grained sphalerite±galena±pyrite matrix with fragments of quartz, carbonate and wall rock (Fig. 14d). Wall rock clasts commonly contain F_2 folds refolded during D_3 and clast orientations define linear zones which appear to be the product of shearing. Both the preservation of refolded clasts and orientation of the conjugate vein set suggests breccia and vein development was synchronous with the development of D_4 folds.

MINERALIZATION STYLES

Five major mineralization styles are discriminated that reflect variations in dominant sulphide species, grain size and sedimentological or structural setting of potentially economic mineralization. Further subdivision of these major groups reflects variation in sedimentological or structural setting and grain size (Table 3).

Stratiform mineralization styles in this classification scheme are defined as those that are contained within specific styles of sedimentary or carbonate layering at a millimetre- to centimetre-scale whilst, the term stratabound refers to vein- or breccia-hosted mineralization that may or may not be conformable with bedding, but are bound within a broader stratigraphic interval (after Bates and Jackson, 1987).

STRATIFORM SPHALERITE-DOMINANT MINERALIZATION STYLES

This style is characterized by very fine-grained honey-, light brown or red-brown sphalerite in specific carbonate-bearing sedimentary or carbonate layers. Distinct varieties in this category are defined on the basis of the host layering, include rhythmically laminated siltstone-hosted sphalerite, mudstone-hosted sphalerite and nodular carbonate-hosted sphalerite.

Rhythmically laminated siltstone-hosted sphalerite mineralization: Sphalerite occurs as fine to microcrystalline, subhedral to anhedral crystals dispersed within carbonate-quartz laminations, that alternate with pyritic or carbonaceous laminations in rhythmically laminated carbonaceous and pyritic siltstones respectively (Fig. 15a and b). Mineralized laminations typically consist of sphalerite - ferroan dolomite ± calcite ± K-feldspar ± quartz (predominantly detrital). The sphalerite-content of individual bands varies from less than 5% to as much as 50%. In sphalerite-rich layers, mineralization may be homogeneous or discontinuously distributed in fleck-like aggregates at a hand specimen scale. In sparsely mineralized layers, sphalerite typically occurs along layer margins adjacent to spheroidal pyrite or carbonaceous laminations. Sphalerite also fringes pyritic laminations as solitary crystals intergrown with pyrite, or as millimetre-sized, elongate aggregates that envelope spheroidal pyrite crystals.

Nodular carbonate-hosted sphalerite mineralization: Fine-grained to microcrystalline, anhedral sphalerite crystals and millimetre-sized irregular crystal aggregates are hosted by nodular carbonate layers in laminated pyritic siltstones (Fig. 15c and d). Sphalerite is typically associated with, and displays planar to ragged grain contacts against the

coarsest-grained carbonate component (typically calcite) in nodular layers. Other sulphides that occur with sphalerite include euhedral, microcrystalline to fine-grained pyrite and less commonly pyrrhotite. Sphalerite rarely occurs with spheroidal pyrite along pyritic laminations or with carbonate (typically ferroan dolomite) that constitutes light grey wavy laminations in this style.

Shale-hosted sphalerite mineralization: This style is characterized by the presence of irregular disseminated fine-grained sphalerite hosted by black shale beds in shaly banded mudstones (Fig. 15e). Sphalerite crystals are typically anhedral and occur with calcite - euhedral pyrite ± bitumen ± pyrrhotite ± quartz ± K-feldspar and rare galena ± white mica. This association typically occurs in sub-mm to millimetre-sized, elongate pod-like zones that are variably distributed along layers (Fig. 15f). Sphalerite varies in grainsize from less than 5μm to 100μm and occurs interstitial to coarser grained carbonates, silicates and euhedral pyrite. Bitumen is typically finer than 25μm and occurs interstitial to, or intergrown with sphalerite.

Shale-hosted sphalerite typically occurs adjacent to spheroidal pyrite mineralized layers within adjacent and equivalent shaly bedding intervals. However, sphalerite mineralization occurs independently of spheroidal pyrite at a microscopic scale in the manner of rhythmically laminated siltstone- and nodular carbonate-hosted mineralization.

Mudstone-hosted mineralization: Sphalerite and/or galena occur as ultrafine-grained anhedral crystals that form irregular interlocking crystal aggregates with carbonate (ferroan dolomite and/or calcite) ± K-feldspar ± quartz ± hydrophlogopite ± euhedral pyrite ± pyrrhotite in millimetre- to centimetre-thick mudstone bedding intervals. Sulphides may be regularly dispersed throughout the entire mudstone (Fig. 15a) or occur in bands that are discontinuous and exhibit ragged boundaries at a hand-specimen scale. Elsewhere, mineralization occurs in irregularly dispersed fleck-like aggregates, or as fine concentrations that mimic the distribution of bedforms (Fig. 15g). Either galena or sphalerite is the dominant sulphide species and constitutes < 5 to 50% of individual

mudstone layers. Galena is typically finer-grained than sphalerite and is equivalent in size to surrounding mineral phases (avg. 10-20μm) whilst sphalerite is typically coarser grained (i.e. 10-70μm). Mudstone-hosted sphalerite is common, and sphalerite-rich layers are typically honey-coloured to pale orange. In contrast, mudstone-hosted galena is rare and only present in feldspathic mudstones. Galena-bearing zones are steel grey in appearance (Fig. 15h). Mudstone-hosted sphalerite and galena both occur in association with stratabound styles of mineralization (next section). Some tuffaceous marker beds and white carbonate bands contain disseminated sulphides, most commonly sphalerite, that display similar associations to mudstone-hosted mineralization.

SPHALERITE-DOMINANT STRATABOUND MINERALIZATION

Sphalerite is typically coarser-grained in this second style, and generally brown to red-brown.

Banded, breccia-vein -hosted sphalerite mineralization: This variety is characterized by semi-massive fine to medium-grained, crystalline sphalerite in layer-parallel bands at a hand-specimen scale (Figs 15h and 16a). Bands vary in thickness from 1mm-30cm (avg. 1mm-3cm) and occur as solitary layers or in stacks that consist of an average of 5-10 bands. Sphalerite bands are hosted by rhythmically laminated carbonaceous or pyritic siltstones, shaly banded mudstones and occur along contacts between banded mudstones and rhythmically laminated pyritic siltstones. They have parallel planar and or folded margins at a hand-specimen scale and are bounded by continuous sedimentary layers at this scale. They also locally contain fragments of wall rock. Band contacts are typically sharp. However, bounding sedimentary layers locally also contain abundant disseminated red-brown sphalerite, resembling that of the stratiform sphalerite mineralization styles.

Thin sections reveal that sphalerite-rich bands consist of a range of minerals with consistent textural relationships. Sphalerite is the dominant constituent of the bands (50 - 95%) and occurs interstitial to, or microbrecciates non-sulphide phases (e.g. Fig. 12b). Non-sulphide phases include quartz - calcite ± K-feldspar ± hyalophane ±

hydrophlogopite ± ferroan dolomite that occur as fine-grained, subhedral to euhedral crystals distributed along band margins or as fine to coarse-grained, anhedral to subhedral crystals irregularly distributed within the band (Fig. 16b). Fine-grained euhedral pyrite less commonly lines band margins whilst pyrrhotite ± galena occur as fine-grained inclusions in sphalerite.

The term 'breccia-vein -hosted' has been used for this style of mineralization for two reasons. Firstly, the morphology and distribution of the majority of non-sulphide phases in the bands suggests that these phases precipitated into open space. At least some of the sphalerite is interstitial and thus deposited after carbonate and silicate infill. However, a significant proportion of the silicate and carbonate phases are corroded and enveloped by sphalerite or brecciated by sphalerite. This indicates that sphalerite occurs as both breccia matrix and replacements within the band. Thus, this style of mineralization appears to be the product of a complex paragenetic and structural history.

Fine-grained breccia-hosted sphalerite mineralization: Several distinctive features enable differentiation of this mineralization style from the vein-breccia -hosted style. These include the finer-grained nature of sphalerite, abundance of breccia clasts, and layer-parallel preferential orientation exhibited by these clasts in drill core and thin section (Fig. 16c and d). However, there are shared features insomuch that these breccias, like breccia-vein-hosted sphalerite are commonly conformable, have planar to wavy margins and vary in thickness from several millimetres to 10cm.

Very fine-grained, light- to red-brown sphalerite with minor pyrrhotite and rare galena form the matrix of these breccias (e.g. Fig. 14a), and a wide variety of clasts have been recorded. These include fragmented carbonate veins with coarse-grained sphalerite along margins, laminated pyritic siltstone and mudstone fragments, monomineralic clasts including calcite, ferroan dolomite, K-feldspar, hyalophane and hydrophlogopite (reminiscent of infill in the breccia vein-hosted style) and fragments that contain stratiform sphalerite (e.g. Part B, Fig. 14). Clasts are typically irregular or tabular in shape,

subrounded, vary in length from sub-mm to 2cm and represent 5 to 30% of individual breccia layers by volume.

GALENA-RICH MINERALIZATION STYLES

Discordant vein-hosted galena mineralization: Discordant veins host fine to coarse-grained galena±pyrite±sphalerite±pyrrhotite and rare carbonate. Galena is subhedral, occurs interstitial to euhedral pyrite and forms irregularly interlocking crystal aggregates with sphalerite and pyrrhotite. These veins are typically less than a few millimetres thick, have irregular to planar margins and are commonly discontinuous at a meso-and microscopic scale (Fig. 16a). Veins typically occur in sets that are either irregularly distributed, or occur as orthogonal networks. Structurally continuous vein sets are developed at a scale of 1 to 10cm, although numerous sets occur within metre-thick intervals. Orthogonal vein networks consist of veins that lie both subparallel and perpendicular to bedding. Subparallel veins are typically superimposed on preexisting sphalerite mineralized layers whilst veins exhibiting a greater degree of discordancy cross-cut adjacent unmineralized layers (typically mudstones). These discordant veins generally taper away from adjacent subparallel veins (Figs 10a and h). A sub-set of veins within this group have galena±carbonate±sphalerite infill and are distinguished by the development of millimetre to sub-mm thick, discontinuous galena±sphalerite alteration selvages. These veins are specifically developed in feldspathic host rocks. Like the majority of galena-rich veins, they are developed orthogonal to bedding, and are discontinuous. Furthermore, like other veins, their extent appears to be solely dependent on the width of the bed which they cross-cut (e.g. Fig. 14a cf. Part B, Fig. 15a and b).

Medium- to coarse-grained galena breccias: The matrix to breccias of this type consists predominantly of galena±euhedral pyrite (Fig. 16e). Galena constitutes at least 40% of the breccia and pyrite less than 10%. Galena is medium to coarse-grained and occurs as irregular interlocking crystal aggregates or interstitial to medium to coarse-grained cubic pyrite. Breccias contain clasts that vary in length from sub-mm to a few centimetres. Larger clasts are typically blocky and subrounded and consist predominantly of

fragmented mudstone, and to a lesser extent pyritic siltstone and stratiform and stratabound sphalerite. Smaller clasts are commonly only evident in thin section and include wall rock fragments and irregular, subrounded monomineralic clasts composed of a variety of silicates, carbonates or sphalerite.

Medium- to coarse-grained galena breccias vary in thickness from 1-100cm but are mostly 2-10cm thick. They commonly occur as concordant bands with planar and parallel margins. However, they are also structurally continuous with orthogonal galena vein-sets that pierce adjacent wall rock and pinch out in drill core or grade into irregular discordant galena vein networks that have anastomosing and irregular margins.

Fine-grained galena breccias: Fine-grained galena breccias have a dull lustre in hand specimen compared with the other styles of galena (Fig. 16a). Galena occurs as matrix and constitutes at least 40 and up to 75% of the breccia. Variation in the composition and size of breccia clasts is essentially equivalent to that reported for medium- to coarse-grained galena breccias. However, clasts are typically ovoid to spheroidal in shape, have smooth to irregular margins that are rounded, and may exhibit a bedding-parallel preferred orientation (Fig. 16f). Fine-grained galena breccias are also distinguished by their typical occurrence as conformable bands with planar and parallel margins. These breccias generally vary in thickness from a few millimetres to 15cm.

Mixed sphalerite-galena-pyrrhotite-pyrite breccias: Mixed sulphide breccias contain variable proportions of fine-grained galena, sphalerite, pyrrhotite and pyrite as matrix components which constitute at least 70% of the breccia. The sulphides are typically irregularly distributed through the matrix such that specific sulphide-rich domains can be distinguished within the breccia at a hand-specimen scale (Fig. 16g). The morphology of these domains is variable from elongate to wavy and flame-like. Breccia clasts vary from sub-mm to several centimetres in size, are typically well-rounded and include fragments of mudstone, black shale, laminated pyritic siltstones, laminated siltstone-hosted stratiform sphalerite mineralization, fine-grained sphalerite breccia and monomineralic

calcite, ferroan dolomite and quartz. Mixed sulphide breccias are typically a few centimetres to 10cm thick and have sharp, wavy margins that lie subparallel to bedding.

CHALCOPYRITE-BEARING MINERALIZATION STYLES

Chalcopyrite-pyrrhotite-carbonate±pyrite±sphalerite±galena±chlorite±biotite±K-feldspar veins: Veins containing permutations of these minerals are commonly less than 1cm thick and occur in bifurcating sets and regular vein networks. Vein sets are commonly superimposed on and microbrecciate preexisting carbonate veins or are developed along planar or folded bedding surfaces (Figs 15e and 16h). Very fine-grained sulphides are the dominant constituent with either calcite or ferroan dolomite. Ankerite and siderite also occur as infill in association with ferroan dolomite. Biotite and chlorite occur as vein infill, but are restricted in occurrence to the A and B stratigraphic intervals. Chalcopyrite-bearing veins have diffuse alteration selvages that predominantly consist of millimetre-sized pyrrhotite laths, minor fine-grained chalcopyrite, sphalerite and rare galena. Biotite and chlorite are locally abundant as selvage constituents and occur as fine disseminations and as millimetre-sized disc-shaped clots with pyrrhotite and chalcopyrite.

Medium-grained pyrrhotite±chalcopyrite breccias: Breccias of this type consist of semi-massive fine to medium-grained pyrrhotite with microcrystalline inclusions of pyrite and chalcopyrite. Pyrrhotite matrix represents greater than 70% of the breccia and breccia clasts are rounded to irregular, sub-mm and millimetre-sized (Fig. 16h). In common with the previously described breccia types, these contain a diversity of clasts including host rock fragments and monomineralic carbonate, silicate and sulphide fragments. These breccias are typically developed along bedding surfaces and vary in thickness from several millimetres to 15cm. Breccia contacts vary from planar to irregular and are locally connected to veinlets with diffuse pyrrhotite selvages.

FAULT-HOSTED MINERALIZATION

Coarse-grained calcite-quartz-dolomite-sphalerite -dominant fault-fill: This occurs as medium to very coarse-grained infill in the J75-type fault zones that vary in thickness

from a few centimetres to several metres. Either grey dolomite or white calcite is the dominant fill constituting up to 70% of the assemblage. Sphalerite constitutes 5 to 20% and commonly occurs interstitial to carbonate and quartz. Sphalerite is typically the only sulphide phase present, however in the southern portion of the deposit a drill hole I698 WI#3A intersected a 40cm zone that was infilled by very coarse-grained galena-pyrite-chalcopyrite-pyrrhotite in addition to sphalerite, dolomite, quartz and minor calcite (Fig. 16i).

Calcite-sphalerite-galena±native silver fault-fill: Coarse-grained sphalerite± galena ± pyrite± fluorite and rare native silver with tetrahedrite occur as infill with pink and white calcite, in L70-type fault zones at localities where faults intersect mineralized zones. Sphalerite typically occurs as the first stage of infill in the fault and is generally honey-coloured. Galena and pyrite are commonly interstitial to sphalerite and calcite (Fig. 16j). Native silver is intergrown with galena and further contains microscopic intergrowths of tetrahedrite. Mineralized fault zones observed in drill core vary from a few to 15cm thick and generally consist of several veins as well as carbonaceous fault gouge.

MINERALIZATION STYLE AND METAL DISTRIBUTION PATTERNS

The main objectives of this section are to:

1. Describe the distribution of sphalerite and galena-dominant mineralization styles within a range of stratigraphic intervals and along the extent of the main economic zone at George Fisher.
2. To compare the distribution of sphalerite and galena mineralization styles to the distribution of Zn and Pb grades in the same intervals to ascertain which mineralization styles contribute to potentially ore grade mineralization.

GENERAL DISTRIBUTION PATTERNS

The distribution and relative proportions of stratiform and stratabound sphalerite-dominant, and stratabound galena-dominant mineralization styles are plotted with Zn and

Pb assay data and superimposed on stratigraphic outlines for the F-E and D-C-B ore zones from diamond drill holes located on sections 7180mN, 7220mN, 7300mN, 7660mN, 7740mN and 7820mN (Fig. 17). The thickness of assay splits varies from 0.9-9m but is typically 0.9-2.0m and half-core was sampled (unpub. MIM Ltd data). Correlation of mineralized zones illustrates that they are elongate lenses that exhibit maximum thicknesses to the south and are consistently contained within 2-20m thick stratigraphic intervals along strike. However, lenses anastomose, bifurcate, pinch-out and cross-cut stratigraphy within each respective stratigraphic interval (e.g. F2 interval, Fig. 17a, D interval, Fig. 17b). The styles of mineralization that constitute individual lenses are variable along strike. However, sphalerite-dominant and galena-dominant mineralization styles are present in all ore zones.

RELATIONSHIPS IN THE F-E STRATIGRAPHIC INTERVAL

The F and E stratigraphic interval consists of four, 2-12m thick, rhythmically laminated pyritic siltstone intervals (denoted F1 to 3 and E) that host mineralization and are separated by unmineralized banded or medium-bedded mudstones (Fig. 17a). The interval has a maximum thickness of 48m. However, it is disrupted by late-stage faults that have removed portions of the stratigraphy.

A range of mineralization styles are represented throughout this stratigraphic interval. Stratabound breccia-vein -hosted sphalerite and fine grained sphalerite breccias of the stratabound sphalerite-dominant style, are volumetrically most abundant throughout the entire interval. One of these textural types represents the dominant variety of stratabound sphalerite-dominant mineralization in each ore lens. The distribution of these textural varieties does not systematically vary with respect to northing or host rock type in the F2, F3 or E intervals. However, the distribution of breccia-vein -hosted sphalerite and fine-grained sphalerite breccias does vary with northing in the F1 lens. Breccia-vein -hosted sphalerite is dominant in the southernmost drill hole (J718 WI#4), whilst fine grained sphalerite breccias are dominant in all other drill holes (Fig. 17a). In addition, the relative

abundance of stratabound sphalerite-dominant mineralization decreases to the north irrespective of the dominant textural variety.

Stratiform sphalerite mineralization and stratabound galena-dominant mineralization styles are relatively abundant and widespread to the south, and decrease in abundance to the north, similar to stratabound sphalerite-dominant mineralization. However, the distribution of these mineralization styles varies throughout the studied drill holes. The relative abundance and stratigraphic position of stratiform sphalerite and stratabound galena styles is fairly consistent in the F2 and E intervals but erratic in the F1 and F3 intervals (Fig. 17a).

Highest Zn grades are most consistently developed in the lower portion of the F2 lens, but otherwise, the distribution of Zn mineralization is variable along strike and other high Zn occurrences vary with respect to stratigraphic position. Highest Pb coincides with highest Zn. However, Pb grades are relatively low overall and restricted throughout the entire interval compared with Zn. The mineralization styles that are consistently responsible for highest grades of Zn and Pb are fine-grained sphalerite breccias and fine grained galena breccias respectively. Other varieties of stratabound mineralization including breccia-vein -hosted sphalerite and discordant galena veins, and stratiform mineralization styles are locally abundant in high grade zones. In such cases, they are not the most abundant mineralization style. In lower grade ore lens, these mineralization styles locally dominate, but such occurrences do not constitute relatively high grade intersections.

RELATIONSHIPS IN THE D-C-B STRATIGRAPHIC INTERVAL

The D through to B stratigraphic interval similarly consists of alternating rhythmically laminated pyritic siltstones that host mineralization, are variably intercalated with banded mudstones, and separated by unmineralized banded or medium-bedded mudstones. However, the D-C-B interval can be distinguished from the F-E interval by its greater total economic metal content and increased abundance of galena. The D-C-B interval has a maximum thickness of about 110m but is disrupted by late-stage faulting in

northernmost drill holes. Mineralization style distributions and assay data plots illustrate that all sphalerite-dominant and galena-dominant mineralization styles are present in the interval and highest grades are evenly distributed (Fig. 17b).

The most striking feature of the D-C-B interval is the variation in the distribution of different sphalerite and galena breccias. Coarse-grained sphalerite and galena are dominant to the south, especially within the D and C zones, whilst fine-grained sphalerite and galena breccias are dominant to the north (Fig. 17b). This variation does not coincide with changes in the nature of the host rock, but more closely mimics variation in intensity of meso- to macroscopic folds (cf. Fig. 10). Furthermore, these mineralization styles are the major contributor to highest grades of Zn and Pb throughout the sequence. In contrast, stratiform sphalerite and discordant vein-hosted galena alone, do not form high grade intersections of a scale significant to mining. These mineralization styles are irregularly dispersed and the enveloping surfaces to zones containing either of these mineralization types are discordant to sedimentary layering and cross-cut tuffaceous marker beds at moderate to high angles.

The variation in dominant style of mineralization from south to north is mimicked by a decrease in the number and thickness of relatively high grade Zn and Pb intersections (Fig. 17b). This is most evident on the distribution plot of galena mineralization styles which illustrates the decrease in thickness of stratigraphically equivalent galena-rich zones from several metres in the south to tens of centimetres in the north (Fig. 17b).

DISCUSSION AND CONCLUSIONS

The Urquhart Shale Formation at the George Fisher deposit consists of a regularly alternating sequence of variably bedded dolomitic and calcitic mudstones, rhythmically laminated pyritic siltstones and intervals characterized by intercalations of banded mudstones and rhythmically laminated pyritic siltstones. The sequence is further

characterized by abundant carbonate banding which occurs in two forms. Nodular carbonate occurs as millimetre thick anastomosing layers specifically superimposed on rhythmically laminated pyritic siltstones whilst layer-parallel white carbonate bands occur as millimetre- to centimetre-thick planar bands in banded mudstones and rhythmically laminated pyritic siltstone intervals.

Zinc-Pb-Ag sulphides occur as stacked anastomosing and stratabound lenses hosted by specific rhythmically laminated pyritic siltstone intervals. Stratabound sphalerite-dominant mineralization styles (sphalerite breccia-veins and fine-grained breccias) and stratabound galena-rich mineralization styles (medium and fine-grained galena breccias) are the most volumetrically-significant and responsible for essentially all economic zones. Stratiform sphalerite, including finely layered, rhythmically laminated siltstone-hosted sphalerite and nodular carbonate-hosted sphalerite are locally abundant and spatially associated with stratabound mineralization styles. However, isolated occurrences typically only constitute lower grade intersections with typical Zn grades of about 5%.

A fundamental sedimentological control on the distribution of sphalerite and galena is indicated from the superposition of economic sulphides on rhythmically laminated pyritic siltstones at a deposit scale, and at fine-scale, the preferential development of stratiform sphalerite mineralization in specific sedimentary layers. Furthermore, stratabound mineralization styles exhibit a strong bedding subparallelism at a fine-scale, as do ore lenses at a deposit-scale.

The fact that the bulk of mineralization is contained within veins or breccias, commonly with planar and parallel margins, indicates that one of the key factors in the localization of *ore* was the development of structural fluid channelways after sedimentation and at least, partial consolidation of the sedimentary pile. One of the major differences between barren mudstones and rhythmically laminated pyritic siltstones is the scale of bedding units. It is likely that surfaces such as laminations in rhythmically laminated pyritic siltstones or bedding contacts between banded mudstones and rhythmically laminated siltstones in

intercalated intervals acted as mechanical heterogeneities within the stratigraphic sequence along which fluid channelways, and thus zones of high permeability, were preferentially developed.

ORIGIN OF STRATABOUND VARIETIES OF SPHALERITE AND GALENA

The variation in abundance of medium- to coarse-grained versus fine-grained stratabound sphalerite and galena breccias in the deposit can not be explained on the basis of variably developed fluid channelways or variation in host rock. The lack of any major variation in the host rock sequence and relatively continuous nature of mineralized lenses along strike illustrates that a fundamental bedding control persisted along the extent of the mineralization system.

A meso- to microscale structural analysis of the 7200mN cross-cut C ore zone intersection identified four major ductile deformation events. Breccia-vein -hosted sphalerite was probably likely emplaced during, or prior to, the earliest deformation event, D_1 (pre-regional D_1 event) and folded by D_2 (correlated with regional D_2 event). In contrast, discordant vein-hosted galena, fine grained breccia-hosted galena and fine-grained sphalerite breccias, cross-cut flat-lying folds formed during D_3 and lie in D_4 structural sites (Table 2). The development of these various textures thus spans a time frame of at least 100Ma. This indicates either that mineralization was introduced at different times, or that the range in mineralization styles at the deposit are a product of sulphide deformation and mobilization.

Macroscale structural interpretation suggests large-scale heterogeneity in the development of fold zones. Deformation intensity and fold development correlate with the distribution of sphalerite and galena-rich zones in the southern portion of the economic portion of George Fisher whereas small-scale folds are widespread to the north. This variation in fold intensity coincides with the change in dominant breccia-style from medium/coarse-grained to fine-grained sphalerite and galena varieties from south to north. Thus, it is

possible that variation in breccia styles is a result of deformation rather than representing primary textural variation.

Features of fine-grained sphalerite, galena or mixed sulphide breccias that could be interpreted to be a product of sulphide deformation include the relative decrease in grain size of sulphides, rounded to elongate nature and preferential orientation of breccia clasts, lineations within breccias defined by the distribution of pyrrhotite and development of flame-like sulphide aggregates in mixed sulphide breccias. All of these features are diagnostic of *durchbewegung* structure formed as a result of the milling of materials with varying rheological properties (e.g. Gilligan and Marshall, 1987; Marshall and Gilligan, 1989).

Further evidence that fine-grained breccias represent mechanically deformed ore is the contradictory structural timing of sphalerite breccia-veins and fine-grained sphalerite breccias (i.e. approximately 100Ma) although the sulphide, silicate and carbonate components of both of these stratabound sphalerite-dominant varieties of mineralization are the same (Table 3). If sulphides in these textural settings were derived from separate fluid generations then they also formed in substantially varying geologic environments. A diversity of gangue minerals would be predicted, reflecting variation in fluid composition and P/T conditions during each episode of mineralization. The absence of any mineralogical variation suggests that fine-grained sphalerite breccias did not form from a separate fluid event. The most probable scenario is that fine-grained sphalerite breccias represent the mechanically deformed equivalent of breccia-vein -hosted sphalerite mineralization.

In contrast to the contradictory timing exhibited by stratabound sphalerite-dominant mineralization styles, discordant coarse-grained galena ± sphalerite veins and fine-grained galena breccias are both situated in D_4 structural sites and are structurally continuous with layer-parallel coarse-grained galena breccias. This could be interpreted to mean that galena in these textural settings was introduced to the ore environment late in the tectonic history

of the region in fluid channelways quite distinct from sphalerite. However, the intimate spatial relationship and grade distribution patterns exhibited by galena and sphalerite mineralization at a deposit-scale strongly suggests that they were introduced via the same structural fluid channelways as part of a single mineralization system. Furthermore, the textural similarities between fine-grained sphalerite and galena breccias suggests these textures had a common origin. Thus, it is possible that the presence of coarse-grained galena±sphalerite in D_4 structural sites is also the result of mechanical and/or chemical sulphide mobilization. It is a well known fact that galena is one of the weakest and most ductile common sulphides (Marshall and Gilligan, 1987 and references therein). It is therefore likely that galena preferentially accommodated strain through ore mobilization during regional shortening at the deposit. Textural evidence for the redistribution of galena from original layer-parallel sites includes the pinched-out nature of discordant galena veins and their structural continuity with stratabound galena breccia zones which is typical of piercement structures in deformed ores (cf. Marshall and Gilligan, 1989). In contrast, the small number of discordant galena veins with galena alteration selvages developed in feldspathic mudstones must have formed by precipitation from an infiltrating fluid. Whether these veins formed during D_4 as a result of fluid-facilitated galena redistribution or earlier as a primary precipitate is not clear. The timing and origin of this texture is discussed in Part B. However, the occurrence of fine-grained galena breccias with discordant vein-hosted galena veinlets (remobilized sulphide) and breccia-vein - hosted sphalerite (*in situ* sulphide) in southern portions of the deposit (e.g. Fig. 17b) further suggests that galena preferentially accommodated strain whilst sphalerite essentially remained in original textural sites.

ORIGIN OF STRATIFORM MINERALIZATION STYLES AND RELATIONSHIP TO STRATABOUND SPHALERITE

The variation in textural setting of sphalerite at George Fisher reflects variation in the chemical and/or physical environment of metal deposition. The finely layered nature of rhythmically laminated siltstone-hosted sphalerite has previously been interpreted to represent exhalative mineralization at Mount Isa (e.g. Finlow-Bates and Stumpfl, 1979). If this is the case for stratiform mineralization at George Fisher, then variation in

sphalerite textures reflects gross variation in the environment of deposition of sphalerite. Alternatively, stratiform sphalerite may have formed as a result of fluid flow along bedding-controlled mechanical heterogeneities after sedimentation, similar to stratabound sphalerite.

The close spatial association between stratiform and stratabound mineralization styles at all scales suggests a fundamental link in their development. Features of stratiform mineralization that indicate a post-sedimentation timing for sulphide deposition include:

1. The discordant and discontinuous nature of mudstone-hosted mineralization at a bedding scale and the replacement of carbonate layers by sphalerite which defines current-produced bedforms in these layers (e.g. Fig. 15g).
2. The discordant nature of enveloping surfaces to rhythmically laminated siltstone-hosted and nodular carbonate-hosted mineralization as developed in the B stratigraphic interval (Fig. 17b).
3. Microtextural relationships which indicate that sphalerite commonly occurs interstitial to carbonate in carbonate bands and sedimentary beds.
4. Evidence that breccia-vein -hosted sphalerite and stratiform sphalerite are paragenetically equivalent events at the deposit (see Part B, Table 1).

Furthermore, the only compositional variation between sedimentary layers that host stratiform mineralization (including finely layered varieties) and their unmineralized counterparts is the addition of metals. The absence of mineralogical diversity between unmineralized and mineralized Urquhart Shale contrasts with exhalative deposits that are actively forming on the seafloor today. The latter are characterized by hydrothermal sediments that consist of fine-grained sulphide mixtures and a diversity of minerals (carbonates, sulphates, clays, other phyllosilicates, metal oxides) that are texturally and mineralogically distinct compared with clastic sediments that reflect ambient deposition (e.g. Zierenberg and Shanks, 1983; Pottorf and Barnes, 1983). In contrast, the absence of mineralogical contrasts between mineralized and unmineralized layers has been documented for the Proterozoic sediment-hosted HYC Zn-Pb-Ag deposit at McArthur

River which is interpreted to have formed as a result of bedding-controlled brine influx in the shallow subsurface (Hinman, 1996).

These data indicate that stratiform mineralization at George Fisher does not represent exhalative mineralization. Thus, variation in sphalerite textures can not be explained by invoking variation in the geological environment of metal deposition from the seafloor to sub-seafloor.

Two major differences between stratiform and stratabound mineralization styles that must be accounted for in any metallogenic model include the variation in the nature of the host layering (vein versus sedimentary and carbonate layering) and Zn grade (high versus low). Key factors in the formation of an ore deposit include the permeability and porosity characteristics of a potential sink and the ability to focus mineralizing fluids (Hobbs, 1987). It follows that porous and highly permeable media will likely represent zones of greatest metal deposition, low permeability zones of equivalent or lower porosity will represent zones of lesser metal deposition and impermeable zones with low or no porosity will represent fluid- and metal-absent zones. In this simplistic view, variation in grade exhibited by stratiform and stratabound sphalerite could simply be explained by variation in the permeability and porosity of the layers that host sphalerite. Certainly, fractures that host highest grades of sphalerite as infill represent zones of structurally-enhanced permeability and porosity that had the ability to focus significant volumes of mineralizing fluids. In contrast, sedimentary and carbonate layers represent zones of lower permeability and porosity.

Thus, the most logical explanation for variation in the textural style of sphalerite at George Fisher appears to be variation in the permeability and porosity of layers that host mineralization. In this scenario, veins represent the fill of fracture zones that had highest permeability and porosity and the greatest ability to channel large volumes of fluids, which accords with the fact they host the bulk of sphalerite.

DISTRIBUTION OF STRATIFORM VERSUS STRATABOUND MINERALIZATION STYLES

A key question in studies of deformed sulphide deposits is how far have the metals moved (e.g. Marshall and Gilligan, 1987). Possibilities range from: 1) complete redistribution of the metals from the site of original deposition and movement at a scale of kilometres, 2) redistribution at a scale of hundreds of metres potentially resulting in relocation of high grade zones, to 3) redistribution at a scale of less than several metres producing new ore shoots in some cases, but essentially preserving original zones of greatest metal precipitation.

The presence of primary metal precipitation sites indicates the George Fisher deposit is the original locus of ore deposition. However, it is possible that high grade ore is the product of metal redistribution at a scale of hundreds of metres. Highest grades of Zn and Pb are developed in the southern end of the George Fisher deposit and grade decreases northwards. Highest grade zones are characterized by abundant medium- to coarse-grained sphalerite breccia-veins and galena breccias whilst lower grade zones to the north are dominated by fine-grained sphalerite and galena breccias (milled sulphide breccias). Two characteristics of the system suggest that the pattern of decreasing grade from south to north is not secondary, namely:

1. If highest grade zones of sphalerite formed as a result of metal redistribution then breccia-vein -hosted sphalerite should not appear as one of the youngest textural varieties of stratabound sphalerite.
2. The northward decrease in grade of both Zn and Pb is uniform in high and low grade intervals. This relationship seems too consistent unless the entire deposit has been reconstituted and original high grades were located to the north. If this was the case, it seems highly unlikely that abundant primary sphalerite in breccia-veins or stratiform varieties would be preserved at all, particularly within the northern limits of the system.

Thus, the distribution of mineralization styles and current variation in metal grade at George Fisher appears to reflect primary fluid fluxes at the deposit. Structural analysis of

ore textures illustrates that metals, and in particular galena, migrated at a scale of millimetres to centimetres. Further evaluation is required to determine whether migration at a scale of tens of metres was a significant process at the deposit.

SIGNIFICANCE OF VARIATION IN MINERALIZATION STYLES

The nature, distribution and structural associations of sphalerite and galena rich mineralization styles has strong implications for the genesis of the George Fisher deposit. The abundance of breccia and vein-hosted mineralization strongly suggests that mineralization was introduced after deposition into, at least, a semi-consolidated sedimentary pile. The distribution of mineralization styles at all scales invokes a fundamental bedding-control on the migration of fluids whilst variation in most pristine styles illustrate that local perturbations in permeability and porosity of host layers played an important role in the localization of ore. Furthermore, the heterogeneous development of mineralization styles at a deposit-scale is best explained as a result of heterogeneous sulphide deformation during regional folding that did not involve large-scale remobilization of metals (Part B). Therefore, it seems most likely that economic mineralization at the George Fisher deposit occurred prior to regional folding, in a flat-lying sedimentary pile some time during diagenesis and within a time frame that post dates deposition around ~1653Ma but predates the onset of regional deformation around ~1600Ma. This is distinct from both syngenetic and syntectonic models proposed for Mount Isa by Finlow-Bates and Stumpfl (1979) and Perkins (1997) respectively. However, it accords with a syndiagenetic timing for Zn-Pb-Ag mineralization at Hilton Mine as proposed by Valenta (1994).

COMPARISON WITH MOUNT ISA AND HILTON

Host Rocks: Comparison of representative stratigraphic columns from Mount Isa to Hilton and George Fisher (Fig. 18) reveal significant sedimentological variations and broad similarities between the deposits including:

1. The most distinguishing feature of George Fisher is the apparent increase in proportion of layer parallel nodular carbonate (and possibly layer-parallel white carbonate bands) in the direct host rocks to mineralization.
2. There is a decreased proportion of black shale throughout the sequence from Mount Isa to George Fisher as previously indicated by Clark (1993).
3. The dominant host rocks to mineralization throughout the system are rhythmically laminated pyritic siltstones (irrespective of nodular carbonate content).
4. The portion of Urquhart Shale that contains economic Zn-Pb mineralization is characterized by large-scale intercalations of medium-bedded, stylolitic mudstones and rhythmically laminated pyritic siltstones. These thick mudstones vary in thickness and number at each deposit and thus do not appear to be continuous at a kilometre-scale. Poorly mineralized portions of stratigraphy in each mine environment lack thick medium-bedded mudstone intervals.

The variation in distribution of black shale reflects either variations in organic matter production and/or preservation at each site which could simply be a product of sedimentation rate or water depth (e.g. Selley, 1985). Variations in thickness and number of medium-bedded siltstones between each deposit illustrates that sediment depositional and transport mechanisms also varied. These variations can be accounted for by depositional models that invoke both deep water and hypersaline, shallow to emergent ephemeral lake depositional settings as previously suggested for the Urquhart Shale (e.g. Finlow-Bates and Large, 1978: cf. Neudert, 1983). More importantly, they simply illustrate fundamental variations in sedimentological characteristics at each site of metal deposition which are not accounted for in sedimentary-exhalative models of ore genesis (e.g. Mathias and Clark, 1975). The fact that mineralization at all of these deposits is consistently developed in finely laminated beds, and that each site is characterized by the alternation of medium-bedded mudstones and finely laminated siltstones, illustrates that a host rock control applies throughout the system as a whole. At George Fisher, these bedding permutations produced rheological heterogeneities that enabled the focussing of

mineralizing fluids along permeable layers. The similarities exhibited by each deposit suggests that this could have been a fundamental control at each of the deposits.

In contrast, the presence or absence of nodular carbonate and layer-parallel carbonate bands does not appear to have affected mineralization at each deposit. The origin of both styles of carbonate banding is not clear. They have been interpreted to represent the products of sedimentation, metamorphism and hydrothermal alteration (Neudert, 1983; Waring, 1990a; Perkins, 1997). At George Fisher, carbonate banding is discontinuous and enveloping surfaces that define its distribution are discordant to chronostratigraphic marker horizons. This suggests these bands are not depositional features and that the variable distribution of zones of abundant carbonate banding from Mount Isa to George Fisher may reflect post-depositional modification of the sedimentary pile. Their origin, and relationship to mineralization, is discussed in Part C of this thesis.

Metal Budget: Resource estimates for the Mount Isa, Hilton and George Fisher deposits (Table 4) reveal several key differences. Firstly, the deposits can be differentiated on the basis of Zn/Pb ratios, which increase systematically to the north. Furthermore, Mount Isa is the largest of the Zn-Pb-Ag deposits on the basis of pre-production estimates. George Fisher is second to Mount Isa in size, although George Fisher and Hilton combined probably contained a pre-production resource equivalent in size to Mount Isa, and possibly even richer in metals.

Mineralization Styles: A preliminary comparison of mineralization styles reveals little variation in the textural setting of sphalerite and galena between the deposits although terminology varies considerably (cf. Grondijs and Schouten, 1937; McClay, 1979; Valenta, 1988; Tuesley, 1993; Perkins, 1997). In fact, the only pronounced variation is the absence of stratiform, rhythmically laminated siltstone-hosted galena mineralization at George Fisher. Both very fine-grained galena or sphalerite have been recorded as the dominant sulphide in an equivalent style at Mount Isa mine, locally referred to as 'finely laminated sphalerite or galena' (e.g. Solomon, 1965; Perkins, 1997).

Of all possible variations, the absence of rhythmically laminated siltstone-hosted galena at George Fisher is potentially the most profound with respect to the formulation of genetic models for Mount Isa-style Zn-Pb-Ag mineralization. 'Finely laminated' mineralization at Mount Isa has previously been interpreted to represent exhalative mineralization (e.g. Solomon, 1965; Finlow-Bates and Stumpfl, 1979; Russell et al., 1981). Its absence at George Fisher strongly questions the validity of the exhalative model. Furthermore, the similarity in styles of stratabound mineralization types supports the possibility that mineralization was emplaced prior to regional deformation, during diagenesis, and subjected to a protracted deformation history at all of these deposits.

PART B

EVOLUTION OF ZN-PB-AG AND CU MINERALIZATION AT THE GEORGE FISHER DEPOSIT, MOUNT ISA, AUSTRALIA.

ABSTRACT

The George Fisher deposit is the most recently recognized of the Mount Isa group of deposits hosted by the ~1653 Ma Urquhart Shale in the Western Fold Belt of the Proterozoic Mount Isa Inlier. It is the Cu-poor end-member of the group, and its documentation has revealed hitherto-unrecognized characteristics of a syndiagenetic Zn-Pb-Ag hydrothermal system in the Mount Isa region.

Zinc-Pb-Ag mineralization at George Fisher was the final stage of a complex syndiagenetic alteration paragenesis initiated by fluid flow during early stages of burial, prior to chemical compaction of the sequence. Extensive calcite occurred prior to spheroidal pyrite alteration which is a characteristic feature of the Urquhart Shale in the Mount Isa area. Spheroidal pyrite is selectively developed in rhythmically laminated carbonaceous siltstones that contain stratabound Zn-Pb-Ag ore lenses. Abundant calcite-quartz and Ba-K-feldspar -rich veins are developed in pyrite-altered intervals. Sphalerite, galena, euhedral pyrite, hydrophlogopite (a regularly interlayered vermiculite-phlogopite) and bitumen formed during a later episode of hydrothermal fluid flow that utilized these preexisting fracture systems. Zn-Pb-Ag orebodies are folded and the preferential accommodation of strain by galena at a deposit-scale is illustrated by its apparent syn- to late-tectonic paragenetic setting. However, a Pb-isotope model age of ~1653Ma suggests the early timing of metal concentration.

Fluid evolution of the Zn-Pb-Ag hydrothermal system has been constrained from textural associations and mineral chemistry. The alteration parageneses reflect the influx of at least three chemically-distinct fluids. Ore-forming metals were transported in slightly oxidized,

near neutral brines. The source of sulphur was either sulphate, transported with metals and reduced at the site by an organic compound such as CH_4, or alternatively as H_2S transported to the site in a separate reduced brine.

The maximum temperature of hydrothermal mineralization is constrained to be ~200°C, based on reflectance of migrabitumens that are coeval with sphalerite and galena and occur interstitial to carbonates in host rocks. These migrabitumens exhibit mesophase textures which indicates thermal overprinting after their emplacement. Thus, reflectance data can be further used to constrain peak temperatures attained during regional deformation in the region to ~200°C. A second migrabitumen population occurs in veins and is texturally distinguished by devolatization pores and grain zonation defined by variable anisotropy from core to rim. Textural zonation of these grains is atypical of textures developed by thermal overprinting and probably records chemical alteration of bitumens as a result of a later fluid event.

Subeconomic Cu was emplaced some 75-125Ma after Zn-Pb-Ag mineralization. Fluid flow at this time was mainly restricted to the western, fault-bounded margin of the deposit. Pyrrhotite, biotite, chlorite and ankerite alteration are dominant manifestations of this event which is deduced to have occurred at temperatures of 250-300°C based on phyllosilicate mineral stability. This temperature is some 30-80°C lower than temperatures reached during Cu formation at Mount Isa.

The partial superposition of late tectonic Cu mineralization on a syndiagenetic Zn-Pb-Ag hydrothermal system has resulted in complex mineralogical-temporal-temperature deposit-scale zonation at George Fisher not been recognized at Hilton or Mount Isa. This suggests superposition of late tectonic Cu mineralization may have homogenized syndiagenetic hydrothermal signatures at the latter deposits.

INTRODUCTION

George Fisher (107Mt @ 93g/t Ag, 5.4% Pb and 11.1% Zn) is the northern site of economic Mount Isa style Zn-Pb-Ag ore hosted by the Proterozoic Urquhart Shale. The origin of Mount Isa-style Zn-Pb-Ag mineralization and its relationship to syn-late tectonic Cu mineralization at Mount Isa is unresolved (e.g. Finlow-Bates and Stumpfl, 1979, Neudert, 1983, Perkins, 1997). George Fisher is the Cu-poor end member of the mineralization system and thus provides an opportunity to examine the Zn-Pb ores where the effects of Cu mineralization are minimal.

Recent examination of the George Fisher deposit reveals that the bulk of economic Zn-Pb-Ag mineralization is vein- and breccia-hosted (Part A). Furthermore, mineralization style distribution patterns and a range of structural timing relationships between different mineralization styles at the deposit, are probably the product of structural overprinting on a syndiagenetic ore system (Part A). These deposit characteristics do not conform with synsedimentary or syn-late tectonic genetic models previously applied to the Mount Isa deposit.

The main objective of this paper is to refine the genetic model for the deposit based on description of the paragenetic evolution, and constraints on the nature of ore-forming fluids from mineral associations and chemistry.

PARAGENESIS

Nine stages of alteration and mineralization paragenesis have been delineated at the deposit (Table 1). Textural interpretations are based in part on hand specimen relationships observed in underground drill core and specimens collected from the 7200mN cross-cut . These have been augmented with thin section petrology and scanning electron microscopy whilst mineral identification has been confirmed using thin section, electron microprobe analysis and X-ray diffraction (Appendices I, III and IV). Alteration distribution patterns presented in this section are derived from graphic drill logs of select

stratigraphic intervals, including the H, F-E and D-C-B intervals in a series of drill holes that are spaced along the extent of the main economic zone (Part A, Fig. 5). These were selected for detailed analysis as they exhibit a wide range of differences in host rocks, mineral assemblages and metal content (Figs 1, 2 & 3). Detailed descriptions of alteration assemblages are also included in this section to complement textural descriptions of sphalerite and galena given in Part A.

STAGE I - CALCITIZATION, NODULE AND STYLOLITE DEVELOPMENT

Calcite is a major rock-forming component of all mudstones, layer parallel white carbonate bands, nodular carbonate and to a lesser extent rhythmically laminated pyritic siltstones. However, in each of these various textural settings, calcite displays consistent timing relationships with respect to ferroan dolomite and detrital quartz host rock constituents.

Calcite alteration in mudstones and siltstones : Calcite alteration typically imparts a bleached appearance and is irregularly or pervasively distributed at a hand specimen scale (Fig. 4a and b). Calcite is typically fine grained, but coarser than ferroan dolomite and detrital quartz host rock components (Fig. 4c). Key textural features that suggest that calcite is an alteration product in mudstones and siltstones include the discordant distribution of calcite-rich zones along strike (Figs 1, 2 and 3), the preservation of irregular dolomitic clots, poor preservation of bedforms in calcite-rich zones, and coincident development of calcite nodules at a hand-specimen scale (e.g. Fig. 4b). No differential compaction of bedding was detected around these nodules which indicates that they formed in well-consolidated sediments.

Nodular calcite bands: Calcite is the major constituent of coalescing and displacive nodular layers (in contrast to singular oval-shaped nodules developed in mudstones), selectively developed in rhythmically laminated pyritic siltstones (Fig. 4d). These layers consist predominantly of very fine to coarse grained, anhedral to euhedral calcite which is locally intergrown with K-feldspar, and envelopes irregular aggregates of ferroan

dolomite-quartz (Fig. 4d, e and 5a). Several features suggest that calcite in these layers is an alteration product. Coarse-grained calcite aggregates locally truncate and are discordant to ferroan dolomite-detrital quartz layering (Fig. 4d) and ferroan dolomite-quartz aggregates included in calcite within the bounds of the nodular layer have sharp to irregular and diffuse outlines (Fig. 4d). They are interpreted to represent relicts of both *in situ* and fragmented wall rock that have been partially replaced by calcite. Thus it is evident that calcite post-dates the formation of quartz and ferroan dolomite. Relict cavities lined by microcrystalline rhombohedral calcite in nodular layers are common at a microscopic scale (Fig. 4e and 5b) indicating that a component of calcite also formed as open-space infill in nodular layers.

Layer-parallel white carbonate bands : These bands typically consist of at least 70% calcite with minor K-feldspar and ultrafine quartz-ferroan dolomite aggregates. They exhibit sharp planar contacts with surrounding beds, but also exhibit diffuse upper and lower contacts which are defined by the distribution of calcite (Fig. 5c). This mineral distribution pattern is not typical of primary depositional structures produced by either suspended sediment deposition or current load deposition. Thus, it is probable that the calcite component of these bands is an alteration product like that in nodular layers and mudstones. Quartz-ferroan dolomite aggregates are interpreted to be relict constituents of the protolith to calcite alteration which was probably a thin sedimentary bed.

Whole rock mineral abundances: Further evidence for replacement and infill by calcite during Stage I calcitization comes from whole rock mineral abundance relationships. Representative samples of all major rock types and carbonate bands are included in plots of total whole rock quartz versus whole rock carbonate and whole rock quartz versus whole rock calcite (Fig. 6). A near 1:1 negative correlation is evident in all samples examined between these mineral constituents for plots of ferroan dolomite+Stage I calcite versus quartz (Fig. 6a). The trend defines a mixing line between a quartz-rich versus carbonate-rich rock. Thus, Stage I calcite-bearing bands (layer-parallel white calcite bands and nodular calcite) that plot to the lower far right of the plot either represent replacement

of previously carbonate-enriched layers or that quartz has also been replaced during the alteration process. Mudstones bearing Stage I calcite alteration contain 45 - 85% total calcite (cf. Fig. 6b). This suggests that either the protolith to alteration for each of these samples varied considerably in original carbonate content, or that quartz was also lost during calcitization.

The abundances of whole rock quartz versus calcite are plotted in Figure 6b. Two linear trends are evident. A mixing line between a pure carbonate and quartz-rich end member (~ 80% quartz) is defined by the distribution of layer-parallel white calcite bands and mudstones. The bulk of the samples plot towards the carbonate-rich end member suggesting the protolith to calcitization in these samples was carbonate-rich. In contrast, nodular calcite defines a separate mixing trend between a pure carbonate and a relatively quartz-poor end member. This indicates that either another mineral phase was present in these layers prior to calcitization, or that additional calcite was introduced to the rock. Trends exhibited by rhythmically laminated pyritic siltstones and normalized rhythmically laminated siltstones illustrate the effect on mixing by a third major mineral component (i.e. pyrite, Fig. 6a). No third major component, that may have been entirely replaced, has been detected in nodular calcite layers. However, a component of nodular calcite occurs as infill as well as replacement of ferroan dolomite. Thus the mixing trend defined by nodular calcite on a plot of total calcite versus quartz potentially reflects the proportion of calcite infill versus replacement in each layer.

The data illustrate that the various textural forms and distribution of Stage I calcite alteration are related, at least in part, to the original layering. Thus, the selective distribution of Stage I calcite reflects that of preexisting carbonate and/or, primary variation in the permeability and porosity characteristics of original layers.

Stylolitization: High amplitude carbonaceous stylolites are developed throughout medium-bedded mudstones whilst carbonaceous microstylolites and solution seams are common in banded mudstones and rhythmically laminated pyritic siltstones (e.g. Figs 4c and 5d).

These stylolites lie parallel to bedding and tuffaceous marker beds, and are affected by the oldest folds. They therefore formed prior to regional deformation some time during burial of the sedimentary pile and are interpreted to represent the products of basin compaction. The onset of chemical compaction in mixed carbonate-siliciclastic mudstones is highly variable and has been documented at depths from approximately 300 to 1500m (e.g. Moore, 1989). Calcite-altered intervals in mudstones and layer-parallel white bands are cross-cut and juxtaposed by stylolites (Fig. 4a,c and 5d). Thus, calcitization of ferroan dolomitic host rocks could have occurred at any time from shallow to deep burial diagenesis.

STAGE II - PYRITIZATION

The Urquhart Shale Formation is distinguished from all other formations in the Mount Isa Group by the abundance of a fine grained variety of pyrite. A detailed account of the morphology of this pyrite at Mount Isa is given in Perkins (1998). A close spatial association exists between the distributions of spheroidal pyrite and carbonaceous units at George Fisher. This pyrite is a rock-forming constituent of rhythmically laminated pyritic siltstones (typically 10 - 25%) in which it is irregularly distributed along millimetre to sub-mm thick carbonaceous laminations that alternate rhythmically with light grey carbonate-rich laminations (e.g. Fig. 4d). Pyrite is also locally disseminated along carbonaceous layers in shaly banded mudstones and along carbonaceous stylolites (e.g. Fig. 5d). Fine-grained pyrite crystals vary in diameter from sub-μm to 25μm and are typically spheroidal or dodecahedral (Fig. 5a, b and d). This variety of pyrite is referred to as spheroidal to differentiate it from other younger and texturally distinct forms.

Timing with respect to calcitization: Spheroidal pyrite and calcite are for the most part developed in different sedimentary layers at a variety of scales at George Fisher (e.g. Fig. 5a). However, consistent paragenetic relationships are displayed where these two minerals occur together. Spheroidal pyrite occurs preferentially along carbonaceous stylolites that developed after calcitization (Fig. 5d). Furthermore, stringers of spheroidal

pyrite cross-cut nodular layers (Fig. 4d). Both these associations suggest that the spheroidal pyrite formed after calcite alteration at the deposit (Table 1).

STAGE III - CELSIAN-HYALOPHANE-K-FELDSPAR VEINS AND ALTERATION

Zoned celsian-hyalophane-K-feldspar occurs in younger portions (hanging wall) of the stratigraphic sequence from the D stratigraphic interval upwards as a constituent in veins, mudstones and siltstones (Fig. 3b). It is rare, and only at significant depth, in the I to E stratigraphic intervals. Zones in which Ba-K-feldspars occur as a rock constituent are distinctively buff-white coloured (e.g. Figs 7a & b), several metres wide and present as discontinuous and bifurcating, stratabound lenses that are discordant to tuffaceous marker beds and extend for tens to hundreds of metres (Fig. 3b).

Zoned celsian-hyalophane-K-feldspar crystals occur as fine to medium-grained infill in bedding-parallel and locally discordant veins with calcite and/or ferroan dolomite and quartz. Barium-K-feldspars typically constitute 10-50% of the vein, carbonate infill varies from 20-70% whilst quartz is least abundant (typically < 10%). A key feature of the infill association is the chemical zonation from celsian to hyalophane to K-feldspar or K-feldspar to celsian to hyalophane to K-feldspar from core to rim (Appendix IV). Up to five growth bands have been differentiated within individual grains, using scanning electron microscopy, defined by variation in Ba content of feldspars (Fig. 8a and b). Quartz and ferroan dolomite typically predate feldspar whilst calcite generally infilled prior to and after feldspars (see below).

The feldspars also occur as very fine-grained alteration preferentially developed in banded mudstones (Figs 8c). Anhedral to euhedral feldspar crystals in these layers display sequential chemical zonation of Ba exhibited by vein infill (Fig. 8d). Feldspars are typically developed along quartz, ferroan dolomite or calcite grain margins in mudstone layers and are both regularly dispersed through layers or preferentially developed adjacent to, and along bedding planes (Fig. 7a and 8c). The very fine-grained nature of these feldspars makes it difficult to ascertain what proportions are alteration products of

preexisting carbonates and/or silicates, as opposed to infill in microvein arrays that utilized preexisting structural weaknesses at grain margins and bedding contacts. However, it is clear that at least a component of feldspar occurs as an alteration product since it pseudomorphs elongate objects in several thin sections sampled from the D ore zone (Fig. 9a). It is possible that these are relict of felsic glass shards such as occur in tuffaceous marker beds (e.g. Croxford, 1964). Calcite rarely occurs as an alteration component with Ba-K-feldspar (e.g. Fig. 9b). Quartz and ferroan dolomite alteration have not been recorded in association with Stage III Ba-K-feldspar-bearing veins.

Timing with respect to calcitization and stylolite development: Discordant Ba-K-feldspar-bearing veins locally cross-cut pyritized stylolites (Fig. 9b). Furthermore, the absence of concentrations along stylolites in calcite-bearing layers and absence of stylolitic surfaces superimposed on veins suggests that the feldspars formed after stylolite development.

Timing with respect to pyritization: Veins infilled by Ba-K-feldspar are commonly developed along contacts between rhythmically laminated pyritic siltstones and banded mudstones (e.g. Fig. 8c). These veins locally cross-cut pyritized stylolites (Fig. 9b). Thus, it is likely that spheroidal pyrite precipitation occurred prior to Ba-K-feldspar vein development.

Calcite-ferroan dolomite-quartz veins in footwall stratigraphic intervals: Bedding-parallel veins infilled by calcite and/or ferroan dolomite, and quartz are typically 1-2mm thick and developed in rhythmically laminated pyritic siltstones in footwall portions of the sequence. These veins mineralogically differ only by the absence of Ba-K-feldspar infill, but exhibit equivalent timing associations to spheroidal pyrite and stylolitization as Ba-K-feldspar -bearing veins. They are included as part of Stage III as a result.

STAGE IV - SPHALERITE MINERALIZATION

This was the earliest and main stage of sphalerite mineralization at George Fisher. It has been subdivided into five substages which are heterogeneously developed and defined on the basis of the dominant mineral constituent.

Stage IVa - Migrabitumen

Two populations of migrabitumen (classification after Jacob, 1989) have been identified at George Fisher. The first is epi-impsonite that has an average BRo_{max}=1.45% (maximum bitumen reflectance in oil, see Appendix VIII), suggesting maximum palaeotemperatures of approximately 200°C (cf. Barker and Goldstein, 1990, Barker and Pawlewicz, 1986). This type of migrabitumen is brownish-grey under reflected light and most grains display mesophase textures in the form of small domains characterized by a pin-point anisotropy. It occurs as:

1. Micro- to cryptocrystalline infill in intergranular pore spaces in all major rock types but is most common in shaly banded mudstone intervals (Fig. 10a).
2. Irregular particles that contain spheroidal pyrite inclusions, occur interstitial to, or are intergrown with sphalerite and galena in shaly banded mudstones (Fig. 10b).
3. As a major constituent of alteration selvages developed around hairline fractures with microcrystalline sphalerite and brassy pyrite (see below) and superimposed on calcite alteration zones (Fig. 10c).

Six whole rock total organic carbon (TOC) analyses range from approximately 0.3 to 3.6% (Appendix IX). Highest TOC occur in shaly banded mudstones and are in the range estimated for evolved oil source rocks (e.g. Selley, 1985). Thus it is possible that the migrabitumen disseminated throughout the host rocks at George Fisher is a thermally matured residue of locally sourced liquid hydrocarbons.

The second migrabitumen population was identified in several satellite veins in the I stratigraphic interval. It occurs as variably fragmented solid matter that formed before sphalerite, galena, pyrite, pyrrhotite, calcite and/or quartz infill (Table 1, Figs 10d & e).

This type of migrabitumen is also a common, although minor, constituent of a large calcite-dolomite-quartz -filled bedding-parallel structure that is a prominent feature in the I stratigraphic interval in the southern portion of the deposit. However, it has not been recorded as infill in veins in any of the major ore lenses. It ranges from meso- to cata-impsonite, with two samples yielding BRo_{max}=2.91% and 5.31% respectively, that imply minimum palaeotemperatures of at least 280°C (cf. Barker and Pawlewicz, 1986, Barker and Goldstein, 1990). Meso- to cata-impsonite occurs as fine to medium-grained blocky and angular grains that contain abundant devolatization pores and exhibit distinctive internal textural zonation patterns. Cores of the grains are typically isotropic. Irregular rims can be distinguished from isotropic cores by the systematic development of mesophase textures (Fig. 10e). The inner portions of these rims form a gradational contact with isotropic cores and are texturally distinguished by the presence of small domains with fine pin-point anisotropy. This texture zones outwards over a few microns to coarser anisotropic domains, which in turn form sharp contacts with irregularly developed, microcrystalline, fibrous anisotropic outer rims.

A plot of the maximum and minimum reflectance values from three samples, representing both migrabitumen populations, displays a positive, linear trend with slope slightly greater than 1 (Fig. 11). This trend is typical of regionally matured rather than thermally-altered bitumens in which graphitization is advanced (e.g. Goodarzi et. al., 1992).

Stage IVb - Brassy pyrite alteration

Brassy pyrite develops a distinctive brassy tarnish on exposed surfaces. The dominant manifestation of this paragenetic stage is brassy pyrite alteration of rhythmically laminated pyritic (spheroidal) siltstones. Most brassy pyrite alteration bands are a millimetre to several centimetres thick and semi-massive in appearance (Figs 7a and 12a). They consist of spheroidal pyrite enveloped by sub- to euhedral brassy pyrite grains with cubic faces that vary in length from 20μm to a few millimetres. Several intervals in the upper parts of the stratigraphy contain metre-thick lenses of massive brassy pyrite (Fig. 7, Part A). Brassy pyrite alteration is most commonly developed as selvages to rhythmically

laminated siltstone-hosted sphalerite, nodular calcite-hosted sphalerite and breccia-vein-hosted sphalerite. In such instances it may also occur as minor infill, which formed before sphalerite, in veins or vughs in nodular calcite (e.g. Fig. 12b).

Brassy pyrite is less common in mudstone intervals though textural associations in these rare cases, further constrain its timing and mineralogical associations. Firstly, brassy pyrite and sphalerite occur together as replacement of celsian-hyalophane-K-feldspar (Fig. 9a and b). Furthermore, brassy pyrite-sphalerite-migrabitumen associations occur as alteration of Stage I calcite-altered mudstones (Fig. 10c). This indicates that brassy pyrite post-dates all aforementioned paragenetic associations, and formed prior to, and during sphalerite mineralization (Table 1).

Stage IVc - Hydrophlogopite

Hydrophlogopite ($K_2(Mg,Fe)_{5.5}\ Al_{1.8}\ Si_{6.4}\ O_{20}(OH)_4.4H_20$) is a Mg-rich, interstratified phlogopite-vermiculite and was identified using general area detector diffraction system (GADDS) and electron microscopy (Appendices III and IV). It forms microcrystalline euhedral laths that vary in length from sub-μm to 100μm, and occur either as:

1. infill (typically 2-10%) in bedding-parallel veins and sphalerite microbreccias that formed after Stage III calcite±celsian-hyalophane-K-feldspar±quartz±ferroan dolomite but prior to sphalerite (Figs 8b, 12c and d),
2. alteration, with sphalerite, in mudstones (Fig. 12c, Table 2).

Hydrophlogopite grains nucleated on brecciated Ba-K-feldspar and carbonate crystals in microbreccias (Fig. 8b) and hydrophlogopite consistently predates sphalerite in these settings (e.g. Fig. 9b). However, hydrophlogopite occurs in the same fluid-structural channelways as sphalerite and is thus included as part of Stage IV.

Stage IVd - Stratiform and breccia-vein -hosted sphalerite mineralization

Sphalerites in stratiform mineralization styles and stratabound, breccia-vein -hosted sphalerites have similar timing relationships. Stage IVd sphalerite forms the oldest

economic sulphide concentrations at the deposit and was emplaced prior to regional folding, either synchronously with, or prior to the earliest deformation event (D_1; Part A, Table 1).

Breccia-veins that host 'banded' sphalerite exhibit a prolonged and complex paragenetic and structural history which culminated in the precipitation of sphalerite. Sphalerite occurs as infill in microbreccias that formed after hydrophlogopite and brassy pyrite infill, and is localized by, and microbrecciates preexisting Stage III feldspar and carbonate-quartz veins (e.g. Figs 8b and 12e). Microbreccias locally cross-cut adjacent wall rock and have sphalerite-rich alteration selvages in which sphalerite predominantly occurs as replacement of Stage II spheroidal pyrite, Stage IV brassy pyrite, Stage III Ba-K-feldspar, and carbonate (e.g. Figs 12 b, c, d and 13). Selvages are developed in rhythmically laminated siltstones, mudstones and shaly banded mudstones and characterize stratiform mineralization styles. Sphalerite (± brassy pyrite) occurs either as alteration of, or infill after Stage I calcite in nodular layers (e.g. Figs 4e and 5a).

STAGE V - FERROAN DOLOMITE VEINS AND STAGE VI - FINE-GRAINED SPHALERITE BRECCIAS

Fine to medium-grained, subhedral, sugary, ferroan dolomite is the major constituent of a common vein set at the deposit. Sphalerite and galena are locally minor vein constituents and occur as infill interstitial to ferroan dolomite grains and as alteration of ferroan dolomite. Veins vary from a few millimetres to a centimetre thick, have planar and parallel margins and are typically discordant (Fig. 14a). These veins cut all major rock types and are most abundant in the F-E and D-C-B stratigraphic intervals (Figs 2 and 3a).

Ferroan dolomite veins provide key constraints on the timing of fine-grained sphalerite breccias (described in Part A). Veins cross-cut stratiform and breccia-vein -hosted sphalerite mineralization, whilst blocky to elongate fragments of sugary dolomite are common in fine-grained sphalerite breccias (Fig. 14a and b). This relationship indicates that these fine-grained sphalerite breccias formed after sugary ferroan dolomite vein

emplacement. However, some sugary dolomite veins also cross-cut fine grained sphalerite breccia margins (Fig 14a and b).

Fine-grained sphalerite breccias have been interpreted to be the product of deformation of preexisting breccia-vein -hosted sphalerite (Part A). Thus, it is likely that contradictory timing relationships exhibited by sugary ferroan dolomite veins and fine-grained sphalerite breccias are a result of this deformation. Features including the preferential deformation of ferroan dolomite veins in fine-grained sphalerite-rich bands compared with adjacent mudstone layers suggests that deformation was partitioned into sphalerite-rich layers after ferroan dolomite vein emplacement (Fig. 14b).

STAGE VII - GALENA MINERALIZATION

Galena occurs in a range of textural settings including coarse-grained and fine-grained matrix to breccias, as coarse-grained infill in discordant veins and as fine disseminations in mudstones (Part A). Both coarse- and fine-grained galena breccias are in nearly all cases superimposed on sphalerite-rich zones at all scales (e.g. Fig. 15a-i, Part A, Fig. 17a and b). A range of textural associations allow the timing of each of these to be established relative to sphalerite mineralization:

1. Coarse-grained galena breccias contain a variety of clast types (Part A). The presence of banded sphalerite, stratiform sphalerite, and Ba-K-feldspar altered mudstone clasts illustrates that these breccia post-date the formation of Stage III and IV alteration and mineralization. Furthermore, clasts having the latter compositions exhibit single generation folds and refold patterns (D_2, D_3 and D_4?; e.g. Fig. 15a and b). In contrast, galena breccia margins do not mimic folded structures exhibited by clasts. Coarse-grained galena breccias therefore formed syn- to post- fold development (Table 1). Sphalerite and carbonate aggregates and monocrystalline fragments commonly exhibit ragged boundaries and it is commonly difficult to piece clasts back together (Fig. 15c and d). This suggests that a component of galena occurs as alteration of sphalerite and carbonate.

2. Discordant coarse-grained galena±sphalerite veins cross-cut banded and mudstone-hosted sphalerite, and are commonly discordant to D_2 and D_3 folds that affect sphalerite-bearing horizons (e.g. Part A, Figs 14a and 16a). Structural timing relationships indicate their emplacement as a result of mechanical mobilization of preexisting galena during D_4 (Part A).

The timing of discordant galena±carbonate±sphalerite veins with galena±sphalerite alteration selvages is less clear. Veins commonly occur in planar sets orthogonal to bedding, and in conjugate arrays particularly around fold hinges (Fig. 15a and b) which mimics the orientation of aforementioned D_4 discordant galena veins. Furthermore, there is no textural evidence that unequivocally demonstrates that veins with selvages formed prior to folding. Therefore, they are included in Stage VII of alteration and mineralization paragenesis.

3. Fine-grained galena breccias developed after Stage IV and VI sphalerite as they contain clasts of banded sphalerite, mudstone-hosted sphalerite, and most commonly, fine-grained sphalerite breccias (e.g. Fig. 15g and h).

4. The intergrowth of galena-sphalerite-bitumen illustrates that galena in this textural setting (stratiform, shale-hosted) formed as part of Stage IVa of the paragenesis. However, the timing of mudstone-hosted galena is less clear simply for the fact that it is spatially associated with discordant galena veins with alteration selvages and both are preferentially developed in Stage III Ba-K-feldspar -altered mudstones. Some galena-bearing layers are displaced by discordant galena veins (Fig. 15b). However, galena in alteration selvages is texturally equivalent to mudstone-hosted galena suggesting a common origin (Fig. 15e). Combined, the relationships suggest a temporal association between the development of the veins and galena alteration bands.

Interconnectivity of galena mineralization styles: The various textural styles of galena display interconnectivity. Medium- to coarse-grained galena breccias typically grade

outwards into discordant coarse-grained galena-rich vein arrays. This association is most evident where galena breccias abut mudstones at a hand specimen scale (e.g. Fig. 15a, b and f) but is also developed within pyrite and sphalerite-rich rocks. Discordant galena veins are also structurally continuous with fine-grained galena breccias (e.g. Fig. 15g). The structural connectivity displayed by galena suggests that the various textural styles had a common origin.

Mineralogical associations: A third generation of pyrite occurs as infill with galena in coarse-grained galena breccias and discordant galena veins (Fig. 15i). It has a distinctive bright yellow tarnish in hand specimen (denoted 'yellow pyrite', Table 1), is fine to very coarse-grained and typically euhedral. Sphalerite±pyrrhotite±calcite±ferroan dolomite also locally infilled in discordant veins prior to precipitation of coarse-grained galena (e.g. Fig. 15i) and pyrrhotite±galena commonly occur as microcrystalline inclusions in breccia-vein -hosted sphalerite (Fig. 12d and e).

STAGE VIII - COPPER MINERALIZATION

Chalcopyrite is the dominant Cu-bearing phase, but is limited to minor vein infill and alteration (e.g. Fig. 16a). In contrast, Stage VIII pyrrhotite, ferroan dolomite and ankerite are more widespread and biotite, chlorite, muscovite and phengite are locally abundant (Fig. 1, 2 and 3). Sphalerite, pyrite, galena, magnetite, greenalite, siderite, quartz, and calcite also formed during Stage VIII as vein infill or alteration components that are locally abundant (Tables 1 and 2).

Stratabound phyllosilicate-pyrrhotite±magnetite±chalcopyrite alteration

One of the striking manifestations of Cu mineralization at George Fisher is the presence of stratabound pyrrhotite - biotite - muscovite - chlorite -bearing alteration zones. These bifurcate and pinch-out along strike, and are superimposed on Ba-K-feldspar alteration zones in younger portions of the stratigraphy from the C ore zone upwards (Fig. 3b). In places, they can be distinguished by the identification of micas and sulphides in hand

specimen, but more commonly by a change in colour of the host rock from grey or buff - coloured to pale green, blue-green or yellow (Fig. 16b & c).

Three alteration assemblages are evident in these zones. Brittle vein sets infilled by pyrrhotite ± biotite ± chalcopyrite ± pyrite ± sphalerite ± galena ± ferroan dolomite ± ankerite ± siderite microbrecciate Stage III veins and alteration zones and cross-cut breccia-vein -hosted and stratiform sphalerite (Fig. 16b and d, Table 2). This vein set has millimetre to sub-mm thick and irregular pyrrhotite-biotite±sphalerite±galena alteration selvages and outer selvages with disseminated lens-shaped pyrrhotite-biotite±sphalerite grain aggregates (Fig. 16d & e). Sphalerite, pyrrhotite and galena typically occur as an alteration of biotite in these selvages (e.g. Fig. 16f). Chlorite - muscovite ± phengite ± ferroan dolomite ± ferroan ankerite ± siderite ± magnetite ± pyrite ± chalcopyrite ± sphalerite ± galena ± pyrrhotite ± greenalite ± quartz alteration is also spatially associated with vein networks (Table 2). This assemblage is commonly pervasive at hand specimen scale, in contrast to pyrrhotite-biotite±sphalerite±galena alteration (Fig. 16b&c). Furthermore, alteration selvages of this type may either be carbonate, chlorite or muscovite-rich and variation in mineral development appears to be dependent on protolith composition (e.g. Fig. 16 b & g). Chlorite and greenalite typically occur as an alteration of biotite in such zones.

Pyrrhotite breccias are also common in these alteration zones. They cross-cut coarse and fine-grained galena breccias, breccia-vein -hosted sphalerite and fine-grained sphalerite indicating they formed after economic Zn-Pb mineralization (Fig. 16c).

Pyrrhotite-dominant alteration zones

Discordant pyrrhotite ± chalcopyrite ± pyrite ± sphalerite ± galena ± calcite vein sets associated with pyrrhotite±calcite±sphalerite alteration are a major manifestation of Cu mineralization outside of stratabound phyllosilicate zones (e.g. Fig. 16h). Sphalerite is the second most common sulphide component in these zones, although it is limited in occurrence. Alteration zones contain abundant lens-shaped pyrrhotite aggregates or

spotted sphalerite both of which may be rimmed by relatively coarse-grained calcite (e.g. Fig. 16i). Evidence for a later generation of sphalerite-calcite in these zones includes the presence of inclusion-free sphalerite-calcite rims developed on sphalerite cores riddled with microcrystalline carbonate and/or galena (Fig. 16i & j).

Ferroan dolomite - ankerite - ferroan ankerite ± siderite alteration

Stage I calcite is the dominant constituent of layer parallel and white calcite bands in the I to C stratigraphic intervals. However, there are numerous zones at George Fisher in which ferroan dolomite-ankerite-ferroan ankerite locally predominate (Figs 1, 2 & 3). The relative abundance of 'dolomitic' banding and absence of Stage I calcite in such bands is most pronounced in the hanging wall of the deposit. Furthermore, stratabound phyllosilicate alteration is only developed in such zones (Fig. 3b). The nature and origin of 'dolomitic' banding is demonstrated to be directly linked with Stage VIII Cu mineralization in Part C.

STAGE IX - BRITTLE FAULT -RELATED MINERALIZATION

Occurrences of J75- and L70-type fault-hosted sphalerite ± galena ± pyrite ± pyrrhotite ± chalcopyrite ± native silver ± tetrahedrite are described in Part A and summarized in Table 2. Sulphides hosted by J75-fault types (Stage IXa) may have been emplaced synchronously with Cu mineralization based on the fact that both Cu mineralization and J75 fault-development coincide with the regional D_3 deformation. Thus L70-type fault-hosted mineralization (Stage IXb) paragenetically represents the youngest sulphide mineralization at the deposit (Table 1).

METAL DISTRIBUTION PATTERNS

An evaluation of metal grade and metal ratio distribution patterns has been undertaken to determine whether systematic deposit-scale spatial associations exist between Zn, Pb and

Cu mineralization events at George Fisher. Metal grade distribution patterns are also compared with alteration distribution patterns.

METAL GRADE DISTRIBUTION

Plots illustrating variation of % Zn with Pb, % Cu with Zn and % Cu with Pb are presented for all stratigraphy and individual stratigraphic intervals from the H through to A intervals (Fig. 17 a-d). Assay values have been plotted for diamond drill holes J702 WI#5, J710 WI#1, J718 WI#4, J722 WI#2, J730 WI#1, K766 WI#2, K774 WI#1 and K782 WI#2 which were logged as part of this study. The thickness of assay splits varies from 0.9-9m but is typically 0.9-2.0m (unpub. MIM Ltd data). Plots for specific stratigraphic intervals contain a variable number of sample points (e.g. Fig. 17b). This predominantly reflects variation in stratigraphic thickness of each respective interval.

Plots for all stratigraphic intervals (Fig. 17a) illustrate:

1. Maximum grades for Zn, Pb and Cu in the selected diamond drill holes are about 33%, 25% and 0.8% respectively.
2. Sample points on the plot of Zn versus Pb define a positively trending wedge-shaped field with a near vertical upper boundary defined by a Zn/Pb $\approx$ 6 and a lower boundary defined by a Zn/Pb $\approx$ 0.8.
3. Lack of covariation between Cu and Zn or Pb.

Comparison with plots for stratigraphic intervals H through to A illustrates heterogeneity in the distribution and abundance of metals between stratigraphic intervals. This is most pronounced with respect to Zn and Pb (Fig. 17b). Three distinct relationships are evident:

1. Zinc versus Pb defines a linear trend with a slope of $\approx$ 4 for the F and E stratigraphic intervals. There are a lack of Pb intersections with grades >5%, and lower maximum Zn% compared with all other stratigraphic intervals. The predominance of stratiform and stratabound sphalerite and localized distribution of stratabound galena in these stratigraphic intervals is evident from graphic logs (refer Part A, Fig. 17a).

2. Zinc versus Pb defines a linear trend for values of Zn ≤10%, Pb ≤5%, and Zn/Pb >2, that diverges into a fan-shaped field at higher grades with Zn/Pb ratios that vary from 1 to 2 in the H, C, B and A intervals. The greatest density of high Zn grades (i.e. Zn >20%) is exhibited by the H interval whilst the greatest density of high Zn and Pb grades (i.e. Zn >15% and Pb >10 %) is exhibited by the C interval. Such a pattern could reflect that galena is typically only locally abundant in these stratigraphic intervals other than the southern portions of the C ore zone (e.g. Part A, Fig. 17b, C and B interval). The high grade nature of Pb intersections most likely reflects the fact that galena is breccia-hosted and these breccias typically contain 40-75% galena by volume.

3. In the D and G intervals Zn versus Pb defines a wedge-shaped field in which Zn/Pb ratios vary from 0.5 to 3 and upper and lower boundaries of the wedge-shaped field are linear. The D interval displays greatest number of intersections with Pb >15%. It is possible that the relatively continuous increase in grade from low to high levels reflects the fact that galena mineralization persists along strike, although they vary in grade, throughout the main economic zone (refer Part A, Fig. 17b). In contrast, Pb values in intervals such as the C and B interval die out over a shorter distance to the north of the deposit (refer Part A, Fig. 17b).

Thus, the main differences between these patterns are the relative abundances of Pb between, and diversity of Pb grades within, each stratigraphic interval. The E and F intervals represent Zn-rich end-members with low total Pb. Trends exhibited by these intervals are equivalent to the correlations exhibited at lower grades in the H, C, B and A intervals. The latter stratigraphic intervals differ in that high grade Pb intersections are also present (more abundant in hanging wall intervals than H interval). However, the bulbous nature of the fan-shaped fields illustrates that Pb-grades are heterogeneously distributed within these intervals. In contrast, the wedge-shaped fields defined by the D and G intervals reflect a continuous range of Pb% from low to high grades.

locally highly irregular in nature (Fig. 18a). Furthermore, Zn/Zn+Pb ratios systematically vary between orebodies. Highest ratios are exhibited by the H orebody and values of Zn/Zn+Pb consistently decrease from the H to the D orebody. This relationship is reversed from the D to A orebodies although values of Zn/Zn+Pb from 0.8 - 1.0 are not abundant in the C to A orebodies compared with the H to F orebodies.

The symmetrical zonation pattern displayed by Zn/Zn+Pb ratios and centred around the D interval is not mimicked by the total metal content of respective stratigraphic intervals. For example, although the D ore zone is one of the richest and highest tonnage intervals, the neighbouring E and F stratigraphic intervals contain low total metal content and also a limited number of high grade Zn or Pb intersections (Fig. 17b). However, hanging wall and footwall stratigraphic intervals can be subdivided into relatively Pb-rich versus Pb-poor orebodies (Fig. 17b). This general subdivision is mimicked by variation in Zn/Zn+Pb ratios and illustrated by the lack of ratios in the range 0.8-1.0 in hanging wall orebodies.

Distribution of Cu/Cu+Pb ratios : Long sections of Cu/Cu+Pb illustrate the restricted distribution of Cu mineralization at George Fisher (Fig. 18b).

Localized Cu-bearing pods exhibiting a range of ratios characterize the H to C intervals. Pods occur at similar northings and relative depths between each orebody. However, the size of and ratio exhibited by each pod is variable. In contrast, relatively continuous Cu-bearing zones are prevalent in the deeper to central portions of the A and B orebodies. The enveloping surface of Cu-bearing zones in these orebodies is subhorizontal and gently plunges southwards although contour outlines are very irregular. Ratios in both orebodies increase with decreasing depth and increase from south to north. However Cu is restricted in occurrence at shallow levels. Highest Cu/Cu+Pb ratios are located in the A orebody and concentrated to the north. The increased relative Cu-content in these intervals correlates with elevated Cu grade (e.g. Fig. 17d).

The distribution of Cu is also heterogeneous. The A and B intervals are the only two with arrays above 0.1wt% Cu. Plots of Cu versus Zn and Pb versus Zn for these intervals further illustrate a lack of equivalent covariation between Cu and Zn or Pb (Fig. 17c and d).

LONG SECTION ANALYSIS

Ratios of Zn/Zn+Pb, and Cu/Cu+Pb have been plotted on long sections for stratigraphic intervals H to A (Figs 18a and b) to determine whether there is any along strike or down dip variation in the distribution of metals.

Ore-bearing zone outlines : All outlines exhibit N-S elongation and have irregular, subhorizontal upper and lower boundaries (Fig. 18a). Hanging wall zones (D to A inclusive) exhibit similar maximum vertical thicknesses of about 500-600m that are consistent along the extent of strike examined. In contrast, footwall zones (H to E inclusive) exhibit variable maximum vertical extents of 400-550m to the south and generally thin northwards. Most orebodies are disrupted by subvertical to inclined breaks defined by an absence of assay data in the vicinity of 7000mN to 7200mN and the vertical thickness of footwall orebodies varies by 50 to 150m across this break. The break correlates with an abundance of late-stage L70-type transverse faults that are known to displace stratigraphy up to 70m to the southern end of George Fisher (refer Part A, Fig. 5). Thus, it is likely that the discontinuity of orebodies across this break, at least in part, reflects displacement as a result of late-stage faulting.

Distribution of Zn/Zn+Pb ratios : Zn/Zn+Pb ratios exhibit values predominantly in the range of 0.4 to 1.0. Their distribution within orebodies and at a deposit-scale define two types of zonation. Each orebody displays a vertical zonation of metal ratios. Lowest Zn/Zn+Pb occurs at the base of the orebody interval. This correlates with the deepest portions of the deposit in the west in three dimensional space. Ratios decrease systematically upwards through each orebody by 0.2 to 0.3. Contours reflecting variations are approximately horizontal to slightly north-plunging, although they are

SUMMARY OF METAL ZONATION PATTERNS

Interrelationships between the distribution of Zn, Pb and Cu in the A and B stratigraphic intervals on the basis of long section ratio analysis indicates that these intervals are zoned with respect to Cu, Pb and Zn. Metal grade plots illustrate no covariation of Cu with Pb+ Zn combined though Zn and Pb grades exhibit positive covariation. The other stratigraphic intervals also show no systematic relationship between the distribution of combined Zn+Pb and Cu whilst Zn and Pb vary systematically throughout. This indicates that fundamentally different factors control the distribution of Zn-Pb and Cu.

COMPARISON WITH ALTERATION DISTRIBUTION PATTERNS

The distribution of Stage I calcite, Stage III Ba-K-feldspar and Stage VIII phyllosilicate and ferroan dolomite - ankerite - ferroan ankerite ± siderite alteration types can be summarized in terms of the following deposit-scale relationships:

1. Footwall stratigraphic intervals (E and lower) contain abundant Stage I calcite alteration which is interdigitated with lenses and bands of Stage VIII ferroan dolomite-ankerite-ferroan ankerite±siderite alteration at a scale of 10 to 100 metres (e.g. Figs 1 and 2).
2. Hanging wall stratigraphic intervals (D and higher) are characterized by lenses of Stage III Ba-K-feldspar alteration and interdigitation of Stage I calcite and Stage VIII ferroan dolomite - ankerite - ferroan ankerite ± siderite alteration (e.g. Fig. 3a and b).
3. The A and B stratigraphic intervals are characterized by the development of Stage VIII phyllosilicate alteration lenses superimposed on preexisting Stage III Ba-K-feldspar alteration and pervasive development of Stage VIII ferroan dolomite - ankerite - ferroan ankerite ± siderite alteration (Fig. 3a and b).

Stage VIII phyllosilicate alteration and pervasive ferroan carbonate alteration in the uppermost stratigraphic intervals correlates directly with zones of relatively abundant Cu. Furthermore, the sporadic distribution of Stage VIII ferroan carbonate alteration throughout the lower stratigraphic sequence mimics the distribution of Cu mineralization

in these zones. Phyllosilicate alteration is locally present in the C and D stratigraphic intervals where it is superimposed on Stage III celsian-hyalophane-K-feldspar alteration zones (Fig. 3b). However, it is not present in lower stratigraphic intervals like Stage VIII ferroan carbonate alteration. It is possible that its distribution reflects the absence of Stage III Ba-K-feldspar -rich precursors in lower portions of the stratigraphy.

Stage III Ba-K-feldspar alteration is developed in hanging wall stratigraphic intervals that also display lowest Zn/Zn+Pb ratios and greatest number of high Pb intersections. In contrast, Stage I calcite alteration predominates in footwall stratigraphic intervals associated with Zn-rich portions of the stratigraphy. Thus, the distribution of Pb and Zn is mimicked by these earliest alteration parageneses whilst Stage VIII Cu mineralization and associated alteration is asymmetrically superimposed on preexisting mineralization and alteration.

LEAD AND SULPHUR ISOTOPE GEOCHEMISTRY

The main objectives of a lead and sulphur isotope study were to determine:

1. Whether galena from different textural settings and paragenetic stages derived their Pb from a single source.
2. Whether sulphur isotope variations exist between sulphides from different textural settings and/or paragenetic stages.

SAMPLING AND ANALYTICAL PROCEDURE

Galena samples for lead isotope analysis were selected on the basis of ore texture and paragenetic setting and include Stage VII galena from medium- to coarse-grained breccias, discordant galena veins and fine-grained breccia. Two galena samples were collected from Stage IXa J75-type fault fill, one of which is associated with chalcopyrite-sphalerite-pyrite-pyrrhotite and the other with sphalerite only. Lead samples were prepared for isotopic analysis at the CSIRO laboratories and analysed in a fully automated single

collector VG54E Thermal Ionisation Mass Spectrometer (Appendix VI). Analyses are plotted with respect to an analytical error ellipse which represents the total of analytical errors produced as a result of variable degrees of fractionation, incurred during analysis, between $^{206}Pb/^{204}Pb$ and $^{207}Pb/^{204}Pb$ combined with counting errors incurred as a result of the small quantities of ^{204}Pb.

Sulphur isotope analyses were undertaken on sulphides including:

1. Mixed Stage IV brassy and Stage II spheroidal pyrite from rhythmically laminated siltstones adjacent to Stage IV nodular carbonate-hosted sphalerite. Separation of the two pyrite types was not possible.
2. Adjacent occurrences of Stage IV breccia-vein -hosted sphalerite and Stage VI medium- to coarse-grained breccia-hosted or discordant vein-hosted galena.
3. Stage IXa sphalerite-galena infill that coprecipitated with chalcopyrite, pyrrhotite and pyrite from a Stage IXa J75-type fault zone.

Relatively coarse-grained mineral separates for sulphur isotope analysis were handpicked from crushed specimens using a binocular microscope. Fine-grained pyrite samples were treated with dilute HCl to remove carbonate and nodular carbonate-hosted sphalerite was extracted from crushed samples as AgS using the extraction method for acid-soluble sulphides of Hall et al. (1988). Samples were analysed at the University of Queensland's Stable Isotope Geochemistry Laboratories. Isotopic data are reported in per mil relative to the Cañon Diablo Troilite and analytical uncertainties are ± 0.3 $\delta^{34}S_{CDT}$ or better (Appendix VII).

LEAD ISOTOPE RESULTS

Lead isotope plots of $^{208}Pb/^{204}Pb$ versus $^{206}Pb/^{204}Pb$ and $^{207}Pb/^{204}Pb$ versus $^{206}Pb/^{204}Pb$ illustrate that all samples display a high degree of homogeneity and can not be differentiated within analytical precision on the basis of textural or paragenetic setting

(Fig. 19a and b). The field defined by $^{207}Pb/^{204}Pb$ versus $^{206}Pb/^{204}Pb$ is also represented relative to the Pb-isotope growth curve derived by Sun et al. (1994) and compared with other deposits from the Northern Australian Proterozoic (Fig. 19c). The Pb-isotope growth curve is adapted from that of Cumming and Richards (1975) which assumes a steady state increase in $^{238}U/^{204}Pb$ and utilizes zircon U-Pb ages of volcanic rocks in the region as bench-mark control points (Sun et al., 1994). A lead model age of about 1653Ma for the George Fisher deposit can be derived from this Pb growth curve. This age closely approximates the ~1650Ma age derived for Pb-Zn ore at the Mount Isa deposit and is some ~10Ma older than Pb-Zn ore at the McArthur River deposit (Fig. 19c).

SULPHUR ISOTOPE RESULTS

Sulphide $\delta^{34}S$ ranges from 5.4 to 14.2‰ and adjacent sulphides exhibit variable relationships depending on the paragenetic setting of sulphide species (Fig. 20a and b). Mixed brassy-spheroidal pyrite $\delta^{34}S$ ranges from 8.3 to 10.6‰ which falls within the range of isotope compositions described for equivalent pyrite mixtures at Mount Isa (cf. Painter, et al., in press). Nodular sphalerite $\delta^{34}S$ varies from 8.7 to 9.7‰, values which are similar to, or lower than values obtained for sphalerite at Mount Isa (cf. Painter et al., in press). Adjacent sulphides of this type display differences in $\delta^{34}S$ of 1.4-1.9‰ (Fig. 20a).

Adjacent Stage IV breccia vein-hosted sphalerite and Stage VII breccia or vein-hosted galena have $\Delta^{34}S_{gn\text{-}sp}$ that vary from 0.3-0.8‰ with $\delta^{34}S_{Gn} \geq \delta^{34}S_{Sp}$. Sphalerite and galena of this type exhibit a total range of $\delta^{34}S$ of 9.6-13.4‰ and 9.9-14.2‰ respectively (Fig. 20a). Furthermore, texturally distinct styles of Stage IV sphalerite sampled from non-adjacent layers, but from the same northing at the deposit, exhibit zero or minor variation in $\delta^{34}S$ (Fig. 20b). The similarity in $\delta^{34}S$ of Stage IV sphalerites and Stage VI galenas suggests that these sulphides shared a common sulphur source and precipitated under

disequilibrium conditions (cf. Ohmoto, 1986). The range of sulphur compositions for sphalerite and galena fall within the field defined by Mount Isa ores (cf. Smith et al., 1978, Painter et al., 1996). However, $\Delta^{34}S_{gn\text{-}sp}$ at Mount Isa varies from 1.5 to 5.0 ‰ with $\delta^{34}S_{Gn} < \delta^{34}S_{Sp}$ for all samples (cf. Smith et al., 1978, Painter et al., in press).

Coexisting Stage IXa sphalerite-galena pairs, sampled from the same vein in which they coprecipitated with chalcopyrite, exhibit greatest differences in, and lowest values of, $\delta^{34}S$ (Fig. 20a and b). Less positive sulphur isotope compositions are only repeated by a few galena samples at Mount Isa (cf. Painter et al., in press). Both sphalerite samples have $\delta^{34}S$ of 7.6% whilst galena varies from 5.4 to 6.1‰ and thus $\delta^{34}S_{Gn} < \delta^{34}S_{Sp}$. Fractionations between sphalerite-galena mineral pairs from the same vein give temperatures of isotopic equilibrium at 260° and 375°C (Friedman and O'Neil, 1977). This broad temperature range suggests that isotopic equilibrium was not achieved, but that these samples approached equilibrium more than the sulphides from earlier parageneses (cf. Oliver et al., 1992).

DISCUSSION

Nine stages of alteration and mineralization have been delineated at George Fisher. They span a geological time frame from some time during diagenesis to late-stage tectonism. Metal and alteration distribution patterns are irregular and define complex spatial-temporal-temperature zonation that closely mimics the stratigraphic age of mineralized intervals and relative proximity to the hanging wall fault zone (Fig. 21).

TEMPERATURE CONSTRAINTS

Stage IV Migrabitumen

Interparticulate migrabitumen (population 1) at George Fisher represents an alteration of organic material. Its restricted distribution is interpreted to reflect a local source. Maximum temperatures yielded by the first migrabitumen population exceed those

expected for hydrocarbon maturation in accordance with the results of previous studies of organic matter at Mount Isa (Saxby and Stephens, 1973; Saxby, 1981). However they also most closely approximate ambient maximum temperature (e.g. Jacob, 1989). Reflectance data indicate migrabitumens were subjected to maximum temperature of 200°C. In addition, the development of mesophase textures within migrabitumens further indicates that this maximum temperature was elevated relative to temperatures of bitumen emplacement. Therefore, this is a maximum temperature constraint for Stage IV sphalerite mineralization and peak metamorphism at George Fisher.

The selective development of mesophase textures along grain margins in solid migrabitumen grains of population 2 is atypical of natural or experimentally produced coke-like textures developed in transitional organic matter (e.g. Robert, 1988). However, equivalent texturally-distinctive rims on migrabitumens with reflectances of 2.0% or greater, have been reported to occur with hydrothermal mineralization in several of the Carboniferous Irish Zn-Pb-Ag deposits (Parnell et al., 1996). Mesophase texture development is not typically considered to form until materials are subjected to at least greenschist facies or equivalent P/T conditions (e.g. Rantitsch, 1995). However, Parnell et al. (1996) determined that initial development of mesophase textures in the bitumens occurred at temperatures lower than 200°C, similar to population 1 migrabitumens. They proposed that the texture formed as a result of rapid heating enhanced by hydrothermal processes. If this is the case, then it is possible that the second migrabitumen population at George Fisher was exposed to locally elevated temperatures which may have alone been responsible for rim development. Alternatively, fibrous rims could represent a chemical precipitate or reaction interface (P. Crosdale, pers. comm. 1998). Thus, the second migrabitumen population may represent an alteration product of migrabitumen population 1 associated with ongoing or later hydrothermal activity at higher temperatures.

Stage IV Hydrophlogopite

Hydrothermal magnesian vermiculite has been identified as a marine deposit in the Atlantis II Deep (Singer and Stoffers, 1981), and interstratified mica-Mg-vermiculites have been interpreted to form by hydrothermal or supergene alteration of phlogopite and talc in veins in Mg-rich skarn (Justo et al., 1987). The good euhedral outlines exhibited by hydrophlogopites in veins and relatively uniform degree of hydration and consistent mineral chemistry suggests that hydrophlogopite at George Fisher formed as a result of direct precipitation from a hydrothermal fluid saturated with respect to Mg (cf. Singer and Stoffers, 1981; Justo et al., 1987). The temperature of formation of vermiculite-phlogopite in hydrothermal environments can be constrained to be less than 200-300°C which is the upper stability limit of vermiculite in hydrothermal regimes (Roy and Romo, 1957; Komarneni and Roy, 1981; Justo et al., 1987) implying temperatures less than 300°C during sphalerite mineralization. Whilst this temperature is not well constrained, it is consistent with reflectance data obtained from bitumens coeval with sphalerite.

Phyllosilicate alteration temperature constraints

The assemblage greenalite+quartz has a maximum temperature of formation of 250-300°C and is only stable at restricted and low values of Xco_2 adjacent to the stability field for magnetite+siderite (Tracy and Frost, 1991). In contrast, vein and alteration assemblages including talc+calcite and tremolite+calcite have been reported south of Lake Moondarra, some 8km southwest of George Fisher, in association with dolerite intrusions, and constrain temperatures in the range of 300 to 350°C at low Xco_2 (Johnstone, 1994). Furthermore, calcite-phlogopite (phlogopite composition; > 80 mol.% Mg/(Mg+Fe)) occurs as a product of the K-feldspar-dolomite reaction at Mount Isa and has a minimum temperature of formation of 330°C at low Xco_2 (Waring, 1990b). Waring (1990b) further estimated that the minimum temperature of biotite-calcite from the K-feldspar-ankerite reaction is 350°C.

None of the latter assemblages are recognized at George Fisher which suggests maximum temperatures were below 330°C. Furthermore, the absence of the assemblage biotite-

calcite suggests that the locally abundant biotite did not form as a product of decarbonation. Biotite typically forms between 300 to 400°C in pelitic assemblages via the reaction chlorite + K-feldspar = muscovite + quartz + biotite + H_2O (Spear, 1993). The reaction proceeds at 300°C in rocks with Fe-rich bulk compositions (Spear, 1993). Frey (1987) described biotite formation via the reaction stilpnomelane+chlorite+K-feldspar = biotite + quartz+ H_2O during burial metamorphism of initially glauconite-bearing sediments. Both reactions demonstrate the formation of biotite at relatively low temperature, which is implicated for the George Fisher deposit by the absence of biotite-calcite assemblage. The intimate spatial association of Stage VIII biotite with Stage III K-feldspar is thus interpreted to reflect the formation of biotite as an alteration product of K-feldspar, possibly via the reaction:

$$2KAlSi_3O_8 + 6M^{2+}(aq) + 8H_2O \rightarrow K_2M^{2+}{}_6Si_6Al_2O_{20}(OH)_4 + 12H^+(aq)$$

where M^{2+} represents Fe^{2+} and Mg^{2+} derived from infiltrating hydrothermal fluids rather than host carbonate rocks. It is proposed that this reaction took place at temperatures below 350°C to account for the absence of coexisting calcite-biotite and that maximum temperatures during Stage VIII Cu mineralization were lower than 330°C to account for the absence of calcite-phlogopite.

TEMPERATURE COMPARISONS FROM SULPHUR ISOTOPE GEOCHEMISTRY

Distinct variations in sulphur isotope compositions are evident between adjacent Stage IV sphalerite-Stage VII galena and Stage IXa sphalerite-galena pairs, even though a restricted number of isotope analyses were undertaken. However, galena from Stage IXa veins can not be differentiated from Stage VII galena on the basis of lead isotopes within the precision of analyses. The homogeneous Pb-isotope composition suggests that galena at George Fisher had a common lead source. Variation in sulphur isotopic composition could represent isotopic evolution of a sulphur source with time. However, this seems highly unlikely considering the amount of time ($\geq$ 75Ma) that separates the development of Stage IV sphalerite and late-stage brittle veins (Part A). Thus variation in sulphur isotope composition between Stage IV sphalerite - Stage VII galena and Stage IXa galena-

sphalerite most likely reflects change in sulphur source. The fact that the latter sulphur isotope compositions have more closely approached equilibrium than older galena and sphalerite is consistent with a higher temperature of precipitation (e.g. Ohmoto, 1986, Oliver et al., 1992). This suggests that the temperature of Cu-bearing fluids was elevated compared with Stage IV sphalerite (and probably Stage VII galena).

$\Delta^{34}S_{gn\text{-}sp}$ exhibited by Stage IV and VII- equivalent sphalerite and galena at Mount Isa vary considerably compared with George Fisher. In fact, $\Delta^{34}S_{gn\text{-}sp}$ of Stage IXa sphalerite-galena more closely approximate $\Delta^{34}S_{gn\text{-}sp}$ exhibited by Stage IV and VII equivalent sphalerite and galena at Mount Isa. This indicates that either Pb-Zn ores were precipitated at lower temperatures at George Fisher, or that sulphur isotope compositions of Pb-Zn ores at Mount Isa have been partly homogenized during a later thermal event as suggested by Smith et al. (1978) (cf. Oliver et al., 1992). Evidence for thermal overprinting by late-stage Cu mineralization presented here suggests that sulphur isotope compositions of Pb-Zn ore may have been homogenized at Mount Isa, and thus are not accurate measures of Zn-Pb ore-forming conditions.

TIMING OF GALENA MINERALIZATION EVENT

The late paragenetic textural setting of galena needs to be considered in light of the Pb-isotope model age of ~1653Ma for all galena mineralization styles at George Fisher. The paragenetic-isotopic age relationship indicates that lead used in the formation of all galena was transported to its current sites during deformation but was derived from a uniform lead source that formed early in the geological history of the area. This probably occurred in one of three ways;

1. Dispersed lead-bearing minerals in the sedimentary package were dissolved by syntectonic fluids and concentrated at George Fisher.
2. A preexisting, concentrated body of galena located at some distance from George Fisher was relocated and reconcentrated at George Fisher by syntectonic fluids.

3. Lead was initially concentrated at George Fisher and redistributed mechanically and/or chemically at a local scale as a result of deformation.

Textural varieties of galena that account for the bulk of Pb include layer-parallel coarse-grained breccias, discordant vein-hosted galena and fine-grained galena breccias. Fine-grained galena breccias and discordant vein-hosted galena formed late in the structural history of the region and represent ore that has been sheared and mobilized out of layer parallel coarse-grained breccia zones respectively (Part A). Therefore, the Pb in these textural varieties of galena was locally derived and not transported in solution by late-tectonic fluids from a separate source region. In fact, it is possible that it was only redistributed at the scale of centimetres.

Coarse-grained galena breccias have been interpreted as original layer-parallel galena concentrations from which late-tectonic galena was mechanically derived (Part A). The late paragenetic setting of coarse-grained galena and evidence for fluid-facilitated galena precipitation in Stage VII veins and selvages suggests the galena has been texturally modified. This leads to the question of the source and transport mechanisms for lead in galena in coarse-grained breccias and discordant veins with galena selvages.

The intimate spatial association between galena and sphalerite, absence of a new suite of alteration minerals associated with galena mineralization that would indicate a separate fluid origin; and systematic distribution of Zn and Pb grades along the extent of the main economic zone, were presented as evidence for the formation of sphalerite and galena in a single mineralization event (Part A). Consistent vertical zonation of Zn/Zn+Pb ratios within the H to A stratigraphic intervals presented here also indicates that galena and sphalerite were probably concentrated during the same event. Thus, the current paragenetic setting of Stage VII coarse-grained galena breccias and discordant veins with galena selvages must also represent modified textural settings. Pb isotope investigations illustrate that galena precipitated in association with chalcopyrite and sphalerite in late Stage IXa veins also has a model age of ~1653Ma. The Pb in galena must have been

derived by fluid-facilitated chemical mobilization of previously crystallized Pb-bearing phases that had the same age as the mineralization event. There is no direct evidence that the Pb in this galena was derived from the dissolution and reprecipitation of preexisting galena. However, the results suggest that 1653Ma-old Pb was mobile during Cu mineralization.

Solution-precipitation creep is a deformation mechanism by which material is mobilized under low grade metamorphic conditions by solute-diffusion either in a static fluid network or as a result of the introduction of a migrating fluid (Cox et al., 1987). Material can be redistributed at a local grain-scale, and at a cm-scale into local fracture networks via this process. Textural features of sulphides which suggest that solution-precipitation creep was significant during deformation include the development of equant, recrystallized grains rather than elongate grain fabrics (Cox, 1987). The relatively coarse-grained and equant nature of galena grains in breccias, and development of alteration selvages along discordant veins that are structurally continuous with breccias suggests that solution-precipitation creep was at least a locally significant deformation mechanism. Thus, it seems probable that Pb in these textural settings was also locally derived, and not introduced via syntectonic fluids from an external source. The distribution of folds at a deposit-scale could also reflect primary galena concentrations to the south of the deposit which preferentially accommodated strain via grain reequilibration. The lower abundance of galena in the northern part of the deposit may have suppressed strain accommodation by solution-precipitation creep alone, resulting in plastic flow in sulphides and enhanced folding in unmineralized layers.

Thus, Stage VII galena is interpreted to result from the mechanical and chemical mobilization of locally derived Pb and S, and the model age of ~1653Ma derived from Pb-isotope data is interpreted to represent the time at which galena (and sphalerite) was originally concentrated in economic proportions at George Fisher. Original textural relationships between sphalerite and galena have probably been by deformation. It is possible that the only primary textural relationships between sphalerite and galena are

preserved in shale bands where bitumen, sphalerite and galena form irregular intergrowths.

EVIDENCE FOR COINCIDENT HYDROTHERMAL MINERALIZATION EVENTS

It has been clearly demonstrated that Cu mineralization at Mount Isa and Hilton occurred syn- to post- regional D_3 deformation (e.g. Perkins, 1984, Valenta, 1988). The following features of the Cu event at George Fisher suggest it is temporally equivalent to the Cu events at Hilton and Mount Isa, and superimposed on a preexisting Zn-Pb system;

1. The late-tectonic paragenetic setting of Stage VIII Cu mineralization.
2. Elevated temperature of Cu mineralization illustrated by stability of greenalite-quartz, compared with lower maximum temperatures exhibited by Stage IV sphalerite mineralization and accompanying alteration.
3. Sulphur isotope geochemistry, especially near-equilibrium compositions of Stage IXa sphalerite and galena that coprecipitated with chalcopyrite, compared with Stage IV sphalerite and VII galena.
4. Lack of covariation of Cu with Pb-Zn grades best illustrated in the A and B stratigraphic intervals combined with the dissociated distribution of metals at a deposit scale and illustrated by metal ratio plots.
5. The distinctive array of alteration assemblages that accompany chalcopyrite and chemical dissimilarities with alteration assemblages that predate and accompany Zn-Pb mineralization.
6. Early paragenetic setting of Stage IV sphalerite and preponderance of textural evidence that illustrates this event pre-dated the onset of regional deformation.
7. The derivation of a Pb-model age for galena of ~1653Ma compared with recently derived $^{40}Ar/^{39}Ar$ date of 1523Ma for Cu mineralization at Mount Isa (Perkins et al., 1999), which effectively separates the Zn-Pb and Cu mineralization events by ~ 60 -130Ma.

CHEMICAL EVOLUTION OF THE ZN-PB SYSTEM

The following section evaluates potential precipitation mechanisms and reaction pathways for the development of Stages II to IV of the alteration and mineralization paragenesis. Reactions are based on textural relationships determined during this study (Table 2).

Stage II spheroidal pyrite precipitation

Sulphur isotope compositions of spheroidal pyrite from Mount Isa Mine and unmineralized Urquhart Shale south of the Transmitter Fault suggest that sulphur was probably derived by thermochemical sulphate reduction (Painter, et al., 1996). However, these data do not show whether sulphate was derived *in situ* in the Urquhart Shale (e.g. from evaporites) or from a fluid source (seawater sulphate). Nodular carbonate layers have been proposed to be pseudomorphous after sulphate evaporites (Neudert, 1983) and thus may have provided a source of sulphur during metal precipitation (cf. Painter et al., in press). However, *in situ* evaporite sulphate reduction and concomitant metal precipitation has been clearly demonstrated to result in the replacement of the evaporite layer by metal sulphides, rather than adjacent laminae (Tompkins, 1994). In contrast, metals precipitated as a result of sulphate reduction by *in situ* organic matter are shown to be inimately mixed with degraded organic matter produced as a result of this process (Leventhal, 1990).

The intimate spatial association of spheroidal pyrite with bituminous laminae (degraded organic matter) at George Fisher and throughout the entire Urquhart Shale, illustrates that thermochemical reduction of fluid-derived sulphate by organic material was the most likely precipitation mechanism for the pyrite. It is interesting to note that at Mount Isa mine, nodular carbonate layers are not abundant in the mineralized sequence whilst spheroidal pyrite is clearly a dominant constituent of the host rocks (refer Part A, Fig. 18; Perkins, 1998). This supports the hypothesis that *in situ* reduction of sulphate evaporites associated with pyrite precipitation was an unlikely process in the Mount Isa system.

The following series of reactions may have induced pyrite precipitation.

Step 1: reduction of aqueous sulphate by reaction with *in situ* organic material (Machel, 1987). Minor bitumen precipitation occurs as a biproduct of organic matter (CH_2O) oxidation via this reaction but is not written into the equation.

$2CH_2O + SO_4^{=}(aq) \rightarrow 2HCO_3^{-} + H_2S$

Step 2: pyrite precipitation

$Fe^{2+}(aq) + 2H_2S + \frac{1}{2} O_2 \rightarrow FeS_2 + H_2O + 2H^{+}(aq)$

Stage III celsian-hyalophane-K-feldspar precipitation

The presence of barium feldspars but absence of barite illustrates that Ba^{2+} was introduced in a fluid with low to no $SO_4^{=}$ (aq) (Blount, 1977). Thus, fluids responsible for Stage III feldspar formation must have been chemically different, at least in terms of $SO_4^{=}$ (aq) concentrations, from those responsible for Stage II pyrite precipitation.

The bulk of Stage III feldspars precipitated into open space. Therefore the majority of ionic components were fluid-derived. Al^{3+} may have been transported as acetate or hydroxyl complexes, both of which are stable within the diagenetic environment at temperatures of 100-200°C and neutral to alkaline conditions (e.g. Benezeth et al., 1994). K-feldspar and celsian precipitation from solution can be expressed in the following reactions;

K-feldspar ; $Al^{3+}(aq) + K^{+}(aq) + 3H_2SiO_3(aq) \rightarrow KAlSi_3O_8 + 4H^{+} + H_2O$

Celsian; $2Al^{3+}(aq) + Ba^{2+}(aq) + 2H_2SiO_3(aq) + 2H_2O \rightarrow BaAl_2Si_2O_8 + 8H^{+}$

The equations illustrate that precipitation of K-feldspar and celsian will occur from a solution which had low activities of H^{+} relative to Al^{3+}, K^{+} and/or Ba^{2+}. Precipitation can also be induced by cooling (Giggenbach, 1981).

The zoning of Stage III feldspars illustrates that chemical conditions of feldspar formation changed with time. Partitioning of K-Ba between feldspars and aqueous chloride solutions has been investigated at high temperatures (e.g. Lagache, 1993). However, no studies are known to have been conducted in the temperature ranges pertinent to vein formation at George Fisher.

Stage IV Sphalerite precipitation

Model reactions based on textural and mineralogical evidence are diverse for sediment-hosted base metal deposits including Mississippi Valley-type deposits, for which a significant amount of fluid characteristics data are available (e.g. Beales, 1975; Anderson and Macqueen, 1988; Barnes, 1997). Models must account for metal and reduced sulphur availability at the site of ore deposition, and transport of these components to the ore site which requires further consideration of metal speciation (e.g. Barnes, 1997). The most widely accepted models for metal transport and precipitation are summarized in Table 3 and Figure 22.

Chloride is considered to be the main inorganic ligand able to transport ore-quantities of metals (e.g. Anderson, 1973; Barrett and Anderson, 1982). Reduced alkaline brines cannot transport ore-forming quantities of Zn and Pb complexed with either hydrosulphide, bisulphide or chloride complexes in solutions at low to moderate temperatures (e.g. Giordano and Barnes, 1981; Cooke and Large, 1998). However, Giordano and Barnes (1981) suggested that inorganic complexes are incapable of transporting quantities of Pb sufficient to account for the abundance of galena in some Mississippi Valley-Type deposits but illustrate that organometallic complexes of lead were significant. Several recent experimental studies further illustrate that carboxylate anions, and in particular acetate, in basinal brines are capable of transporting ore-forming quantities of metals (e.g. Giordano, 1992). Such complexes, at elevated concentrations, have been proposed to be significant in slightly oxidized, slightly acidic basinal brines (Fig. 22) over the temperature range of 100 to 200°C where [chloride]/[acetate] is less than about 10 (Giordano and Drummond, 1991; Giordano, 1992; Benezeth et al., 1994).

Several features of the George Fisher deposit can help to elucidate fluid characteristics and metal transport and precipitation mechanisms and are discussed below with respect to current metal transport and precipitation models.

Acid brine models

The reduced acid-brine model invokes the transport of metals and reduced sulphur in one fluid to the ore site (Table 3). Metal precipitation occurs as a result of cooling, dilution or neutralization (e.g. Anderson, 1973; Table 3; Fig. 24). In contrast, metal precipitation from an oxidized acidic brine will occur either by mixing with reduced sulphur or as a result of sulphate reduction (Table 3).

Neutralization of an acidic brine will occur at the first site of fluid contact with carbonate rocks (e.g. Barnes, 1997) irrespective of sulphur speciation. The carbonate-rich nature of the Urquhart Shale and spatial association of sphalerite and galena with carbonate-rich layers suggests that metals may have been introduced by a reduced acidic brine. If this was the case, then neutralization by reaction with carbonate would have been a viable precipitation mechanism;

$$2HCl(aq) + CaCO_3(s) \rightarrow CaCl_2 + H_2O + CO_2(g)$$

Acid is neutralized by reaction with carbonate.

$$M^{2+}(aq) + H_2S(aq) \rightarrow MS(s) + 2H^+$$

Metal solubilities in the presence of $H_2S(aq)$ decrease and metal sulphides precipitate as a result.

However, there is no evidence for deposit-wide carbonate dissolution (e.g. widespread macroscopic or microscopic secondary porosity and thus friable textures or a later paragenetic stage that recemented these pores, or solution-collapse brecciation) (cf. Beales, 1975; Barnes, 1997). Furthermore, it is interesting to note that in the B interval, a distinctive horizon of rhythmically laminated siltstones above the B TMB retains a consistent stratigraphic thickness despite the discontinuous nature of ore (see Part A, Figs

8c and 17b) implying that there was no volume loss at a deposit scale associated with mineralization. Also, if anything, stratigraphy thickens in major mineralized zones as a result of veining. This suggests that fluids were not strongly acidic.

Mixing and sulphate-reduction models

The spatial association of carbonates and metals, but lack of large-scale carbonate dissolution can be accommodated if metals are transported as either chloride or organic complexes in weakly acid to neutral solutions. Fluid mixing, replacement of preexisting sulphides or sulphate-reduction models are applicable in this case (Table 3). In such processes the quantity of acid produced during metal precipitation is negligible compared with acid brine mechanisms and is not considered likely to produce large-scale carbonate solution although neutralization by carbonate dissolution could occur (e.g. Barnes, 1997).

Possible metal precipitation reactions are listed in Table 4. The dominant types of sphalerite occur as infill in veins and carbonate replacements. Ore metal precipitation in these cases was induced either by mixing with H_2S-rich fluids or by *in situ* sulphate reduction. Sphalerite replacement of spheroidal pyrite is locally significant whilst intergrowth textures with bitumen are minor. Sphalerite replacement of pyrite implicates mixing with a preexisting reduced sulphur source whilst sphalerite-galena-migrabitumen intergrowths indicate sulphate reduction by *in situ* organic material.

Sulphate reduction by *in situ* organic material is not favoured as an ore precipitation mechanism, although it is demonstrated to occur locally, due to the absence of intimate spatial associations between organic material and sphalerite and galena in high grade zones (cf. Leventhal, 1990). In contrast, ore metals at both the Century and McArthur River deposits are intimately mixed with residual hydrocarbons and bitumen at a deposit scale and are good cases in which sulphate reduction by *in situ* organic material has been demonstrated (Hinman, 1996, 1998; Broadbent et al., 1998). Sulphate reduction by mixing with an acidic fluid at the site of metal deposition is also not favoured for the same

reasons given above regarding the lack of large-scale carbonate dissolution. Thus, sulphate reduction by mixing with a reductant such as $CH_4(g)$ is favoured.

An alternative proposition is that metals+sulphate were transported in near neutral, slightly oxidized brines as organic complexes (mainly acetate). However, rather than encountering a reductant at the site of metal deposition, sulphate reduction and metal precipitation was induced by destabilization of the organic complex. In such a scenario, metal precipitation would occur via a three-step process;

Step 1: Destabilization of organometallic complex by decarboxylation.

$ZnCH_3COO^+ \rightarrow Zn^{2+}(aq) + CH_4 + HCO_3^-(aq)$

Decarboxylation proceeds as a result of;

1. Destabilization by increasing temperature at $T \geq 130°C$ (e.g. Carothers and Kharaka, 1978; Surdham et al., 1989).
2. Change in pH by degassing, contact with carbonate-rich rocks or fluid mixing (e.g. Surdham et al., 1989).

Step 2: Sulphate in solution is reduced by methane produced during decarboxylation.

$$CH_4 + 2H^+(aq) + SO_4^{=}(aq) \rightarrow H_2S(aq) + 2HCO_3^-(aq)$$

Step 3: Reduced sulphur availability induces metal precipitation

$$Zn^{2+}(aq) + H_2S(aq) \rightarrow ZnS + 2H^+(aq)$$

No literature is known that has discusses the viability of this mechanism in nature. However, the transport of a 'hidden' reductant with metals and sulphate could account for some of the ongoing dilemmas surrounding base metal transport and precipitation mechanisms (cf. Giordano and Barnes, 1981; Anderson and Macqueen, 1988; Anderson and Garven, 1991; Giordano, 1992).

In summary, whilst available data allow both metal+sulphate and fluid mixing models for metal precipitation and transport, several constraints can be placed on the ore-forming system at George Fisher;

1. If the majority of metals were transported with sulphate, then sulphate reduction occurred as a product of reaction with a reductant such as CH_4 either in an aqueous or gaseous phase rather than *in situ* organic material.
2. If metals mixed with a reduced sulphur source, it is most probable that reduced sulphur was derived from an external source rather than preexisting sulphur-bearing minerals.
3. At least three major phases of fluid influx at George Fisher are responsible for the evolution of Stage II to IV alteration parageneses in order to account for chemical differences of each alteration stage.

SPATIAL EVOLUTION OF THE ZN-PB SYSTEM

The lack of primary textural relationships between sphalerite and galena and thus timing relationships poses problems for predicting fluid fluxes during mineralization. However, zonation of the Zn-Pb system can be reconstructed by unfolding the stratigraphic sequence, removing the effects of Cu mineralization and utilizing metal ratio and metal grade distribution patterns.

The systematic distribution of Zn/Zn+Pb ratios both at the scale of the deposit and within stratigraphic intervals, coupled with spatial links between galena and Stage III K-feldspar alteration and absence of deformation-induced transgressive remobilization indicates that the current metal ratio distribution patterns at the deposit closely approximate original metal distribution patterns (cf. Part A). Therefore, variations of bulk Pb/Zn between stratigraphic intervals probably reflect varying fluid access as the system evolved and Pb-rich ores were originally located to the west.

Lead is significantly less soluble than Zn in the presence of H_2S at low temperature (e.g. Barrett and Anderson, 1982). Thus, if galena precipitated prior to or along with sphalerite, then Pb-rich zones at the deposit indicate zones closest to the fluid source area

and zones of enhanced early fluid flow. If the fluid had high Zn/Pb ratios and was initially saturated with respect to sphalerite (cf. Sverjensky, 1984) then Pb-rich ore zones represent zones closest to the fluid source area and zones of enhanced fluid flow later in the evolution of the Zn-Pb stage. Combined with the fact that metal grade decreases northwards through the deposit (Part A), and lowest Zn/Zn+Pb ratios at the deposit are situated in the southwest portions of the D stratigraphic interval (Fig. 18a), the fluid source for the system can be predicted to have been located to the southwest.

SELECTIVE SUPERPOSITION OF CU MINERALIZATION EVENT

The proximity of Stage VIII Cu mineralization and accompanying alteration assemblages to the Hanging wall fault zone suggests fundamental links between the fault zone and fluid channelling during late tectonism. The distribution pattern is similar to, but more localized, compared with Cu mineralization at Hilton Mine and the latter can also be differentiated by the presence of a large dolerite dyke that intruded the sequence during regional folding (Valenta, 1988). Copper-bearing fluids at Hilton were focussed due to the combined effects of dilation on the Paroo Fault/Dyke Trace Fault zone (Part C, Fig. 2) intersection and enhanced layer-parallel shortening in Pb-Zn zones that enabled fluid flow into permeable horizons. Abundant faulting in the George Fisher area was also probably associated with dilation and bedding-parallel movement which enabled syntectonic, Cu-bearing fluid infiltration. The restricted Cu mineralization at George Fisher could reflect less favourable fault geometries and/or less abundant brittle fault development.

CONCLUSIONS

Base metal sulphides at George Fisher are the products of spatially-coincident syndiagenetic Zn-Pb-Ag and syn-late tectonic Cu mineralization separated by 75-125Ma. Zinc-Pb-Ag mineralization is constrained by a Pb-isotope model age of 1653Ma for ore-stage galena (Part B), and structural evidence that ore emplacement preceded the onset of the Diamantinan Orogeny at 1610-1590Ma (Part A). Furthermore, whilst the Pb-isotope model age approximates the depositional age of the host Urquhart Shale, paragenetic

studies do not suggest synsedimentary metal precipitation. Zinc-Pb-Ag mineralization was the final stage of a complex history of syndiagenetic fluid infiltration, signatures of which are preserved at George Fisher despite the fact that the region has been subjected to intense regional deformation and syntectonic hydrothermal fluid flow. In summary;

1. Stage I calcite occurs as an alteration of preexisting hydrothermal ferroan dolomite (Stage OI ferroan dolomite, Part C). These carbonates can be texturally, chemically and isotopically differentiated from carbonates that formed synchronously with Cu some 125Ma later (Part C). Chemical modelling indicates these carbonates formed as a result of infiltration of relativley hot, reduced, basinal brines (Part C) into a semi-consolidated sedimentary pile, and prior to chemical compaction which is estimated to have occurred at burial depths of a few hundred metres or more.

2. Stage II spheroidal pyrite alteration selectively developed in carbonaceous laminae after calcitization and chemical compaction. Pyrite precipitation occurred from thermochemical sulphate reduction by *in situ* organic material. These fluids were relativly oxidized and their sulphur may have been derived from either sea water or the dissolution of sulphate evaporites during diagenesis. It is unlikely that fluids responsible for carbonate and pyrite precipitation were derived from the same source region. Furthermore, the absence of Stage II sphalerite and galena during this time suggests that ore metals were not transported in these fluids.

3. Bedding-parallel calcite-quartz and Ba-K-feldspar-rich veins developed during Stage III. The Ba-rich association celsian-hyalophane-K-feldspar marks the infiltration of a third chemically distinctive fluid. The feldspars precipitated from neutral to alkaline, reduced and $SO_4^{=}$ -absent fluids, probably as a result of cooling. If these fluids were sulphur-bearing, the sulphur must have remained in a reduced form as either $H_2S(g)$ or $HS^-(aq)$ to account for the absence of barite at the deposit.

4. Ore metals were transported as chloride or organometallic complexes in slightly oxidized, near neutral fluids and were precipitated either as a result of sulphate reduction by CH_4, or by mixing with a H_2S -bearing basin-derived brine. Metal precipitation also occurred at a local scale as a result of mixing with sulphur derived from preexisting *in situ* spheroidal pyrite and by *in situ* organic matter-induced sulphate reduction. The temperature of ore formation was less than 200°C. Temperatures of hydrothermal mineralization may have been elevated relative to ambient conditions causing premature maturation of locally-sourced organic material.

5. The complex paragenesis and predicted variation in fluid chemistry demonstrates that the Urquhart Shale was a major locus of fluid flow during its burial history. In the earliest stages, fluids permeated the entire sedimentary sequence producing pervasive carbonate alterations (Part C). However, it is envisaged that extensive carbonate cementation and alteration, combined with chemical compaction, effectively sealed mudstone horizons throughout the sedimentary sequence. Fluid flow was consequently focussed with time as demonstrated by the selective distribution of spheroidal pyrite in rhythmically laminated siltstones and then, by the development of celsian-hyalophane-K-feldspar veins. These veins were major fluid conduits during Stage IV sphalerite and galena mineralization.

6. The key feature of the Urquhart Shale for the ore formation process throughout the Mount Isa district was the stacking pattern of sedimentary units. All ore intervals are hosted in portions of the sequence charactrerized by intercalation of rhythmically laminated, carbonaceous siltstones with medium- to thick-bedded mudstones (Part A). The contrasts in scale of bedding units combined with abundance of internal bedding heterogeneities in rhythmically laminated siltstones acted as permeability and porosity gradients (primary and secondary) within the sequence, which favoured focussed fluid flow.

7. The coincident zonation of district-scale hydrothermal, syndiagenetic carbonates (Part C) and Pb-Zn sulphide accumulations points towards the existence of a long-lived fault

system that was responsible for channelling of hydrothermal fluids. The existence of such a fault-system is a further key ingredient to the formation of the George Fisher deposit.

8. Zinc-Pb-Ag sulphides were deformed during the Isan Orogeny. The majority of galena and some sphalerite were mechanically and chemically mobilized at a scale of microns to metres during deformation and currently lie in syn- to late-tectonic structural settings. However, deposit-scale primary metal zonation of Zn and Pb is preserved and indicates fluids were sourced from the southwest prior to regional deformation.

9. Copper-bearing hydrothermal fluids were focussed along bedding-parallel fault zones in the waning stages of regional folding and infiltrated a restricted portion of the Zn-Pb-bearing stratigraphy. Temperatures of Cu formation were in the order of ~250-300°C, some 50-100°C higher than the Zn-Pb hydrothermal event, but some 30-80°C lower than peak temperatures during Cu formation at Mount Isa.

10. The preserved record of syndiagenetic hydrothermal alteration and mineralization at George Fisher is a result of restricted syn-late tectonic Cu mineralization at the deposit (Part C).

PART C

MULTIPLE EPISODES OF HYDROTHERMAL CARBONATE FORMATION IN THE PROTEROZOIC URQUHART SHALE AND SIGNIFICANCE FOR THE ORIGIN OF MOUNT ISA-STYLE ZN-PB-AG AND CU MINERALIZATION.

ABSTRACT

The Mount Isa, Hilton and George Fisher deposits are hosted by fine-grained, pyritic and carbonate-rich sedimentary rocks of the ~1653Ma Urquhart Shale in the Western Mount Isa Inlier, Australia. Textural and geochemical variations of carbonate component that are preserved result from heterogeneous superposition of syntectonic carbonate alteration accompanying Cu mineralization on syndiagenetic hydrothermal carbonates associated with Zn-Pb-Ag mineralization.

Finely crystalline, zoned dolomite-ankerite-ferroan dolomite is the oldest carbonate rock component and a major constituent of host rocks at the George Fisher deposit and in poorly mineralized horizons peripheral to the Mount Isa deposit. Textural associations indicate that early zoned dolomites probably formed as replacements of preexisting carbonate grains and matrix and were themselves replaced by calcite prior to stylolitization of the sequence. These calcites are major constituents of variably-bedded carbonate mudstones and displacive and coalescing nodular bands preferentially developed in pyritic siltstones. Distinctive textural zonation exhibited by earliest dolomites and alteration patterns exhibited by calcites can be correlated over some 20km. Reduced $(Fe,Mn)CO_3$-content of all carbonate types with increasing distance from Zn-Pb-Ag sulphides is evident and mimics chemical halos typical of other sediment-hosted deposits in the region.

Two carbonate populations accompany syntectonic Cu mineralization at Mount Isa. Dolomite-ferroan dolomite-ankerite alteration within the silica-dolomite hydrothermal

body that hosts Cu mineralization is coarse-grained and texturally destructive. Fine-grained and texturally-retentive ferroan dolomite-ferroan ankerite solid solutions and siderite alteration are major constituents of the Urquhart Shale in Zn-Pb-Ag mineralized zones marginal to the silica dolomite alteration envelope. Syntectonic ferroan carbonate alteration zones are distinguished by their association with phyllosilicate alteration and absence of syndiagenetic calcite. This population is the dominant constituent of subeconomic zones of Cu mineralization at Hilton and George Fisher.

Both syndiagenetic and syntectonic carbonates define inverted L-shaped fluid-mixing trends representing depletion of whole rock $\delta^{18}O$ and $\delta^{13}C$ relative to isotopically undisturbed examples of Urquhart Shale away from sites of economic Zn-Pb-Ag and Cu mineralization ($\delta^{18}O$ = 19.6 to 22.5‰, $\delta^{13}C$ = -2.2 to -1.9‰). However, syntectonic carbonates are distinguished by greater isotopic depletion ($\Delta^{18}O$~4 to 10‰, $\Delta^{13}C$~1 to -10‰) compared with syngenetic carbonates reflecting different isotopic signatures of infiltrating fluids.

Syndiagenetic zoned dolomites and calcites at George Fisher exhibit narrow ranges of whole rock $\delta^{18}O$ = 17.1 to 18.5‰ and $\delta^{13}C$ = -3.8 to -1.7‰, consistent with formation at elevated temperatures during deep burial. However, fluid mixing trends defined by isotopic depletion of syndiagenetic carbonates combined with chemical depletion is atypical of normal burial trends. The data are consistent with shallow burial emplacement by local infiltration of warm fluids into a cool sedimentary pile. Furthermore, the locus of infiltrating fluids correlates with sites of economic Zn-Pb-Ag mineralization implying that earliest preserved carbonate rock constituents of the Urquhart Shale are hydrothermal products formed at the onset of the Zn-Pb-Ag hydrothermal mineralization event.

The paucity of syndiagenetic zoned dolomites and calcite at Mount Isa and Hilton mine is interpreted to be a product of pervasive hydrothermal ferroan dolomite-ankerite-ferroan

ankerite-siderite alteration superimposed on Zn-Pb-Ag bearing horizons at these deposits. They are interpreted to be products of major fluid influx accompanying economic Cu mineralization. The dominance of syntectonic hydrothermal carbonates at Hilton Mine, just 2km south of George Fisher, reflects the more widespread occurrence of subeconomic Cu mineralization at the deposit.

INTRODUCTION

The Proterozoic Urquhart Shale hosts the Mount Isa Zn-Pb-Ag and Cu deposits, and Hilton and George Fisher Zn-Pb-Ag deposits. The deposits are situated within a 25km strike length of the sequence and combined formed a pre-mining Zn-Pb-Ag resource alone of at least 300Mt grading at 12% Zn, 6% Pb and 130g/t Ag (estimate based on Forrestal, 1990; Perkins, 1990; 1998 MIM report to shareholders).

Zinc-Pb-Ag mineralization at Mount Isa, Hilton and George Fisher is uniformly hosted by rhythmically laminated pyritic siltstones which are separated by barren mudstones. In contrast, Cu mineralization at Mount Isa is contained within a giant syntectonic hydrothermal silica-dolomite breccia and alteration system, tongues of which locally interdigitate with Zn-Pb-Ag ore bodies (e.g. Swager, et al., 1987; Perkins, 1994). The Cu and Zn-Pb-Ag ore bodies at Mount Isa Mine represent separate mineable entities although genetic models for the Mount Isa deposit invoke a range of temporal associations between the two styles of mineralization (e.g. Valenta, 1994, Perkins, 1997).

The association of syntectonic hydrothermal silica-dolomite alteration and Cu mineralization at Mount Isa, compared with paucity of Cu mineralization at Hilton and George Fisher is one of the most outstanding geological variations in the Mount Isa mineralization system (e.g. Mathias and Clark, 1975; Perkins, 1990; Perkins and Bell, 1998).

The George Fisher deposit is distinguished by an abundance of thin nodular and planar carbonate layers within the ore-bearing sequence, which attains similar significance elsewhere in the system within lower and poorly mineralized portions of the Urquhart Shale at Mount Isa mine (Part A, Fig. 18). Furthermore, the dominant carbonate constituent of these distinctive bands at George Fisher varies systematically throughout the deposit. Calcite is the dominant constituent near Zn-Pb-Ag mineralization and occurs predominantly as an alteration of host rock ferroan dolomite (Part B). However, texturally-distinctive carbonate bands in localized zones of syntectonic Cu mineralization at George Fisher are dominated by ferroan dolomite-ankerite-ferroan ankerite-siderite (Figs 1 and 2). Carbonate compositions of these bands at the deposit therefore appear to be related to the heterogeneous development of syntectonic alteration parageneses.

Calcite has only been recognized as a major constituent of mudstones or distinctive carbonate bands elsewhere in the Mount Isa area in poorly mineralized sedimentary rocks peripheral to the Mount Isa deposit (Neudert, 1983; Painter and Neudert, 1994). Furthermore, the carbonate component of the Urquhart Shale near Zn-Pb-Ag ores at Mount Isa and Hilton more closely resembles associations in Cu-bearing zones at George Fisher (Figs 3 and 4).

Numerous studies have addressed the origin of texturally distinctive carbonate bands and of carbonate minerals in the Urquhart Shale (Table 1). However, none of these studies can account for the heterogeneous distribution of texturally distinctive bands and calcite throughout the Urquhart Shale combined with distinctive zonation of carbonates and metals at the George Fisher deposit.

It is evident that the Urquhart Shale is a carbonate-rich sedimentary sequence and that two major carbonate rock-forming constituents are calcite and ferroan dolomite. However, as yet, no consistent explanation has been proffered for the origin of these major rock-forming constituents. This paper presents new petrological, geochemical and stable isotope data for carbonates from the George Fisher deposit and textural and geochemical

comparisons with a selection of carbonates from the Hilton and Mount Isa deposits. Chemical links are established between carbonate constituents and Zn-Pb-Ag and Cu mineralization at George Fisher, Hilton and Mount Isa. A model proposing multiple, temporally-distinct episodes of carbonate+metal formation is proposed to account for the distribution of carbonate minerals throughout the Urquhart Shale.

CHARACTERIZATION OF CARBONATE PHASES

The fine-grained nature of the sequence combined with the difficulty in identifying different carbonate phases using conventional thin section petrology has hampered the understanding of these carbonate types. This prompted a detailed electron microscope investigation of both major rock types and carbonate banding.

Three texturally and temporally distinctive groups of carbonate minerals have been identified as major rock-forming constituents of the Urquhart Shale at George Fisher. The textural, and general compositional characteristics of these carbonate groups and a comparison with poorly mineralized examples of Urquhart Shale located peripheral to the Mount Isa deposit are presented in this section. Terminology used to differentiate each carbonate population is based on the deposit paragenetic framework presented in Part B.

STAGE OI - EARLY DOLOMITE-FERROAN DOLOMITE-ANKERITE

Dolomite-ferroan dolomite-ankerite grains and matrix represent the earliest carbonate type in the Urquhart Shale. This group of carbonate minerals equates with previous references to host rock ferroan dolomite in this thesis.

Early carbonates constitute a matrix and grain component, the latter of which consist of a texturally distinctive array of dolomite, ferroan dolomite and ankerite. Blocky, planar, subhedral to rhombic dolomite (and rare ankerite) typically forms the cores of these grains (Figs 5 and 6a). This dolomite locally contains micron-sized inclusions, or shadow

outlines of a preexisting grain type (Fig. 6a and b). Core dolomites are sequentially enveloped by irregular to planar, 3-8 μm thick ankerite inner rims and by outer rims of ferroan dolomite and ankerite (Fig. 6a to c). Outer rim components may be mixed, or zoned from ferroan dolomite to ankerite and grain outlines respectively vary from irregular, non-planar and poorly defined, to rhombohedral. Outer rim-type, ferroan dolomite and ankerite also envelope quartz grains and this type of matrix is the most volumetrically significant rock-forming component in Stage OI early dolomite-bearing Urquhart Shale at George Fisher (Fig. 6b and d).

Paragenetic Interpretation: Key textural relationships developed throughout all Stage OI early dolomite-bearing Urquhart Shale include the preferential development of inner ankerite rims on dolomite rather than quartz grains. This indicates that ankerite probably formed as a specific replacement of dolomite. The presence of blocky, subrhombic ankerite grains probably reflects complete dolomite grain replacement. Rhombic outlines defined by outer rim ferroan dolomite and ankerite could also represent further grain replacement. However, it is most likely that the majority of the irregularly distributed ferroan dolomite and later ankerite represents an intergranular cement and/or replacement of a preexisting matrix or cement. The consistent morphology of dolomite grains, the preservation of rhombic dolomite crystals and of preexisting grain outlines strongly suggest that this core carbonate also represents a preexisting cement and/or grain replacement rather than a clastic rock component. Thus, Stage OI early dolomites are interpreted to be the products of one or more dolomitization events (Table 2).

STAGE I - CALCITE ALTERATION

Calcite is a dominant constituent of layer parallel, nodular and planar white bands and is locally a significant secondary constituent of mudstones, and to a lesser extent siltstones. Calcites from different major rock types and bands were defined as the first stage of an extensive alteration and mineralization paragenesis at George Fisher and consistently replace 'host rock ferroan dolomites' (Part B). Their relationship to these early dolomites is further examined here.

White band calcite and secondary calcite-rich zones contain variable amounts of quartz, K-feldspar and irregularly shaped quartz - dolomite - ferroan dolomite - ankerite grain aggregates. These aggregates have highly irregular grain outlines, are sporadically distributed in calcitic mudstones and white bands, and early dolomite core-rim-matrix relationships are truncated by calcite (Figs 7a and b). This confirms that calcite represents a replacement of Stage OI dolomite-ferroan dolomite-ankerite (cf. Part B).

Nodular calcite layers also contain relict detrital quartz, including coarse silt-sized grains typical of laminated units, K-feldspar, irregular clots of ferroan-magnesian carbonates and clusters of spheroidal pyrite (e.g. Part B, Fig. 5b). Calcite grains are typically blocky and irregular, although radiating, lath-shaped crystal aggregates are locally present (Fig. 7c). Contact relationships between nodular calcite layers and rhythmically laminated siltstones are variable at a microscopic scale. In places they are obscured by dense aggregates of spheroidal pyrite. However, sharp and irregular transitions are common (e.g. Fig. 7c). Furthermore calcite occurs as the matrix to microbreccias and veinlets that are continuous with nodular layers, are discordant to bedding, brecciate rhythmically laminated siltstones and also truncate core-rim-matrix relationships defined by dolomite-ferroan dolomite-ankerite (Fig. 7c). Microbreccia intensity decreases at micron scale away from nodular calcite margins and grades into ultrafine intergranular networks that are either the product of fracturing, or fluid infiltration along grain boundaries (Fig. 7d).

STAGE VIII SYNTECTONIC FERROAN DOLOMITE-ANKERITE-FERROAN ANKERITE-SIDERITE

The distribution and association of syntectonic ferroan carbonate alteration and veins with Stage VIII Cu mineralization in portions of the system that lack Stage I calcite was described in Part B and illustrated in Figures 1 and 2. Textural characteristics of late syntectonic matrix ferroan carbonate are presented here.

Medium-bedded mudstones, banded mudstones (including samples that have a bleached appearance typical of calcitic mudstones), rhythmically laminated pyritic siltstones and nodular bands from Stage VIII alteration zones have been examined. In all cases, textural

and compositional variations (Fig. 5) are evident between Stage VIII alteration zones and Stage OI early dolomite and Stage I calcite -bearing alteration zones.

Late ferroan carbonate rock constituents display irregular, subhedral to rhombohedral forms, vary in size from fine to relatively coarse-grained (10 to 100 μm) and form subhedral to euhedral-planar and irregular interlocking grain arrays (Fig. 8a - c). Individual crystals contain up to three growth zones which can be differentiated on the basis of $(Fe+Mn)CO_3$-content and zone outwards from ferroan ankerite to ankerite to ferroan dolomite (Fig. 8b). Zoned early dolomites occur locally in the samples (Fig. 8a) but calcite is not present in any form, even in nodular bands (Fig. 8c). Furthermore, contacts between nodular layers and pyritic siltstones could not be distinguished on the basis of carbonate content (e.g. Fig. 8c). A later generation of quartz is also present and some samples contain up to 80% very fine quartz. Quartz infills in veinlets and occurs as an alteration of zoned rhombs (Fig. 8d).

Stage VIII ferroan carbonates can be differentiated from Stage OI early dolomites by;

1. Opposing chemical zonation exhibited by carbonate grains and defined by variation in $FeCO_3$ content.
2. Mineralogical associations including the absence of Stage I calcite and presence of quartz veins and alteration in Stage VIII alteration zones.
3. The relatively coarse grained nature of Stage VIII ferroan carbonates although all carbonates are fine grained.
4. The association of Stage VIII ferroan carbonate alteration with ferroan carbonate veining.

COMPARISON WITH CARBONATES IN POORLY-MINERALIZED URQUHART SHALE

Calcite has been recognized as a volumetrically significant rock-forming component in poorly mineralized Urquhart Shale north of the Mount Isa Mine (Neudert, 1983, Painter and Neudert, 1994). Three banded mudstone samples from diamond drill holes located between 4 and 6 km north of Mount Isa Mine (Fig. 9), provided by M. Painter, have been

examined to determine whether carbonate types and grain relationships equivalent to those at George Fisher are also present in examples of unmineralized calcite-bearing Urquhart Shale.

Early zoned dolomite grains in these samples consist of subrhombic dolomite cores enveloped by several μm-thick ferroan dolomite or ankerite rims (Fig. 10a and b). Rim ferroan dolomite or ankerite is selectively developed around blocky, ultrafine-grained dolomite cores mimicking the associations at George Fisher. Ferroan dolomite forms the dominant matrix component and commonly occurs interstitial to detrital quartz grains. Ferroan dolomite matrix typically has a lower Fe-content than grain rims, similar to chemical variations exhibited by Stage OI early dolomites (Fig. 5)

Stage II calcite is abundant in several bedding intervals and in a discontinuous layer-parallel white band. In each case calcite is spatially associated with minor K-feldspar and has replaced Stage OI dolomite (Figs 10a and b).

PARAGENETIC ASSOCIATIONS

A modified paragenesis (cf. Part B) is presented in Table 2 and emphasizes the relative timing of the various carbonate groups presented above, with respect to vein-dominant carbonate forming events and mineralization at George Fisher. The most important points to note are;

1. Both early dolomite and calcite formation predate both chemical compaction of the sedimentary pile, and earliest sphalerite mineralization associated with migrabitumen emplacement. Furthermore, these minerals are major rock-forming constituents of the Urquhart Shale throughout Zn-Pb -rich portions of the deposit in the absence of syntectonic Cu mineralization.

2. Stage VIII ferroan carbonates are the dominant rock-forming constituent of mudstones, layer-parallel white carbonate bands and nodular carbonate bands of the Urquhart Shale in Cu-bearing zones.

3. Dolomite textures identified in samples located distal to Mount Isa Mine texturally correlate with, and exhibit similar increases in $FeCO_3$ content from core to rim and matrix as Stage OI early dolomites at George Fisher. Samples also exhibit equivalent paragenetic associations of dolomite to calcite. Thus calcite in the latter samples is also interpreted to be paragenetically equivalent to Stage I calcites at George Fisher (Table 2).

CARBONATE CHEMISTRY

Carbonate populations at George Fisher and in distal Urquhart Shale fall within three chemically and temporally distinctive groups; Stage OI dolomite-ankerite solid solutions, Stage I calcite, and Stage VIII ferroan dolomite-ferroan ankerite solid solutions (Fig. 5). Dolomites and ferroan dolomites have (Fe+Mg):Mg > 4, ankerite has Mg+Fe:Mg < 4, and ferroan ankerites contain at least 20 mol.% (Fe+Mn) (after Deer et al., 1989). Chemical characteristics of these different carbonate types are presented in Table 3, summarized below and are based on over 300 single-spot microprobe analyses (Appendix IV). Chemical characteristics of these carbonate groups are compared with a range of other carbonate types from George Fisher, Hilton and Mount Isa (Table 3). The location and timing relationships of different carbonate groups with respect to Zn-Pb-Ag and Cu mineralization within the Mount Isa system is used as a means of differentiating carbonate types as part of the comparison (Table 3).

Analyses are reported in mol.% and have been normalized to 100% for this comparison. They are derived from original analyses with analysis totals that vary between 98 to 102 wt% ($CaO+MnO+FeO+MgO+CO_2$) for dolomites and 97 to 103 wt% for calcites (Appendix IV). Average analytical errors are 0.2-0.3wt% for MnO, 0.4-0.8wt% for FeO, 0.6-0.8wt% for MgO and 0.7-0.8wt% for CaO in dolomites and 0.1-0.2wt% for MnO, 0.2-0.3wt% for FeO, 0.1-0.2wt% for MgO and 1.0-1.1wt% CaO in calcites.

STAGE OI EARLY DOLOMITES

All Stage OI early dolomites exhibit consistent chemical variations between dolomite-ankerite solid solution from core to rim and between rock types, independent of associations with economic grades of Zn-Pb-Ag mineralization and development of Stage I - III alteration (Table 3, Fig. 11a). Core dolomites are near-stoichiometric to Ca-rich (48 to 56 mol.% Ca). Rim and matrix ferroan dolomites and ankerites are also near-stoichiometric (48 to 53 mol.% Ca). Inner rim, outer rim and matrix ankerites exhibit consistent variations in $(Fe,Mn)CO_3$ content. Values range from 7 to 16 mol.% $(Fe,Mn)CO_3$ and typical fall within the range of 11 to 13 mol.% $(Fe,Mn)CO_3$. The $(Fe,Mn)CO_3$ content of outer rim and matrix ferroan dolomites ranges from 4 to 12 mol.% (Fig. 11a).

Plots of $FeCO_3/MnCO_3$ versus $MgCO_3$ mol.% and $FeCO_3$ versus $MnCO_3$ (mol.%) illustrate that separate linear trends are defined by core dolomites, outer rim and matrix ferroan dolomite, and inner rim, outer rim and matrix ankerites respectively and the main chemical variable is $FeCO_3$ (Fig. 11b and c). Mn concentrations vary from amounts lower than detection limits to 3.45 mol.%, are lowest in core dolomites, and display similar maximum values for ferroan dolomites and ankerites (e.g. Fig. 11c). However, the minimum content of $MnCO_3$ increases consistently from dolomites to ferroan dolomite to ankerite and defines a minimum $FeCO_3/MnCO_3$ ratio in all early dolomites of approximately 40 and $MgCO_3/(Fe/Mn)CO_3$ of approximately 10 (Fig. 11b and c). However, $FeCO_3$ and $MnCO_3$ do not clearly covary positively within each textural/compositional group except for the most $FeCO_3$-rich samples which display a weak positive covariation of $FeCO_3$ and $MnCO_3$ (Fig. 11c).

CALCITE ALTERATION

Alteration calcites are variably ferroan and manganiferous and their chemistry varies systematically irrespective of the host rock setting (Table 3, Fig. 12a). $(Fe,Mn)CO_3$ contents vary from 1 to 3 mol.% and the compositional range of each texturally distinctive calcite variety overlaps in the range of 1 to 2 mol.% (Fig. 12a). Nodular and white band

calcite have lower total $(Fe,Mn)CO_3$ whilst calcites from mudstones and siltstone intervals exhibit highest $(Fe,Mn)CO_3$ contents. All calcites contain some $MgCO_3$ which is typically present in mole proportions both lower and higher than total $(Fe,Mn)CO_3$ (Table 2).

Calcites define irregular to linear fields on plots of $FeCO_3/MnCO_3$ versus $MgCO_3$ and $FeCO_3$ versus $MnCO_3$ respectively (Figs 12b and c). On these plots, the most systematic trend is the positive covariation of $FeCO_3$ and $MnCO_3$.

LATE-STAGE FERROAN CARBONATES

Stage VIII alteration carbonates, incorporating carbonate vein infill, have $(Fe,Mn)CO_3$ contents in a huge range from 9 to 85 mol.% (Table 3). Samples spatially associated with subeconomic Cu mineralization and Stage VIII phyllosilicate alteration display consistently greater $(Fe,Mn)CO_3$ contents than unmineralized samples (Fig. 13a, Table 2).

The dominant Stage VIII carbonate rock constituents are ankerites (9-19 mol.% $(Fe,Mn)CO_3$) and ferroan ankerites (20 - 26 mol.% $(Fe,Mn)CO_3$). Carbonates that have replaced preexisting calcite bands include ferroan dolomite with total $(Fe,Mn)CO_3$ of 8 - 11 mol.% and ferroan ankerites with $(Fe,Mn)CO_3$ of 19 - 23 mol.%. Vein-filling carbonates associated with alteration include ferroan ankerite and magnesian siderite which exhibit the widest range of total $(Fe,Mn)CO_3$ (Fig. 13a).

The $FeCO_3$ and $MnCO_3$ contents of all late stage carbonates covary and whilst populations of Stage VIII carbonates lie in variably overlapping clusters, all samples plot within broad, negatively trending, linear fields on plots of $(FeCO_3/MnCO_3)$ versus $MgCO_3$ and $FeCO_3/MnCO_3$ (Fig. 13b and c). However, intersample variation in $MnCO_3$ is limited compared with $FeCO_3$ and ranges from 1 - 4.5 mol.% (Fig. 13c). Highest $MnCO_3$ contents and lowest $FeCO_3/MnCO_3$ ratios are exhibited by ankerites and ferroan dolomites sampled from nodular bands and mudstones. These carbonates are not accompanied by Stage VIII phyllosilicate alteration (Figs 13b and c, Table 3).

CARBONATES IN POORLY-MINERALIZED URQUHART SHALE

Early dolomites and calcites in samples located distal to the Mount Isa deposit plot in the same chemical fields as texturally equivalent Stage OI early dolomites and Stage I calcites at George Fisher (Fig. 14). However, several key chemical variations enable differentiation of early George Fisher carbonates from distal carbonates;

1. The $(Fe,Mn)CO_3$ content of rim and matrix early dolomites in distal Urquhart Shale is consistently lower than George Fisher carbonates although relative variations in $(Fe,Mn)CO_3$ contents of rim and matrix dolomites are similar to those at George Fisher (Fig. 11b and c).

2. Similarly, the $(Fe,Mn)CO_3$ content of calcites is also lower than Stage I George Fisher calcites, although most samples exhibit equivalent $FeCO_3$/ $MnCO_3$ ratios (Fig. 12b and c).

COMPARISON WITH GEORGE FISHER VEIN-HOSTED CARBONATES

Two stages of vein-related carbonates are common at George Fisher in addition to the three major host-rock carbonate groups. These are;

1. Stage III calcite and ferroan dolomite infill which occurs with zoned Ba-K-feldspar in bedding-parallel veins that post-date Stage I calcite and Stage OI dolomites and host Stage IV sphalerite.
2. Syntectonic sugary ferroan dolomite veins that post-date Stage IV sphalerite, but predate Stage VIII Cu mineralization (Tables 2 and 3).

The chemical characteristics of these carbonate groups are compared with Stage OI dolomites, Stage I calcites and Stage VIII ferroan carbonates (Fig. 14). The plots illustrate that trends exhibited by variation in $(Fe,Mn)CO_3$ content of Stage III carbonates mimic those defined by early carbonate populations at George Fisher. In contrast, Stage V sugary dolomite vein infill carbonates plot along a linear trend defined by lower and consistent Fe/Mn ratios. Ferroan dolomites in wall rocks to sugary dolomite veins are chemically similar to early Stage OI early dolomites.

COMPARISON WITH CARBONATE ASSOCIATIONS AT THE HILTON ZN-PB-AG MINE

A selection of chemical analyses of matrix and vein-filling dolomite-ankerite solid solutions and siderites are taken from Valenta (1988) and Tuesley (1993) (Table 3). These carbonates were sampled from the 1 to 4 hanging wall ore bodies at Hilton (nb. 4 o/b TMB correlates with the George Fisher B TMB, Fig. 18, Part A). The carbonates occur with minerals that typify Stage VIII Cu mineralization at George Fisher including chalcopyrite, magnetite and a range of phyllosilicates, but also occur in association with, or in horizons adjacent to economic Zn-Pb-Ag mineralization (Fig. 3, Table 3). Valenta (1988) proposed that the bulk of these carbonates formed during Cu mineralization. Tuesley (1993) proposed that siderites probably formed in association with Zn-Pb-Ag ore formation, but also favoured a syn- to late-tectonic model for Zn-Pb-Ag ore formation.

Chemical comparisons illustrate that Hilton carbonates are chemically similar to Stage VIII George Fisher carbonates, although a greater number of siderites typify the Hilton data set (Figs 15 and 16). Whilst some Hilton samples exhibit greater $MnCO_3$ contents relative to George Fisher carbonates, plots of $FeCO_3/MnCO_3$ ratios illustrate that the majority of Hilton samples lie within George Fisher Stage VIII carbonate fields or extensions of those fields (Fig. 16).

DOLOMITES FROM ZN-PB-AG -BEARING STRATA AT MOUNT ISA MINE

The field defined by whole rock carbonate analyses collected by Stanton (1963) define a continuum between compositions that probably represent variable mixtures of carbonates with compositions similar to Stage OI early dolomites and Stage VIII ferroan carbonates at George Fisher.

SILICA-DOLOMITE ALTERATION AT THE MOUNT ISA CU MINE

Carbonates related to the silica-dolomite alteration system are unquestionably associated with the emplacement of Cu mineralization at Mount Isa (e.g. Perkins, 1994). Chemical analyses presented here were collected by Waring (1990a) and include a range of texturally distinctive varieties (Waring, 1990a):

1. Fine-grained, recrystallized matrix dolomites that display sedimentary authigenic textures. However, it is not clear whether these dolomites are texturally equivalent to Stage OI early dolomites.
2. Fine-grained, variably ferroan and irregular crystalline dolomites accompanied by chalcopyrite-quartz. Typical carbonate grain sizes are in the order of 0.5mm which is very coarse relative to all George Fisher carbonate host rock constituents.
3. Zoned, white, variably ferroan dolomite that infills in quartz±chalcopyrite veins.
4. Porphyroblastic coarse grained dolomite.
5. Calcite-chalcopyrite veins associated with calcitic shales which predominantly occur south of the main Cu ore bodies at Mount Isa. A calcite-chalcopyrite association peripheral to the main subeconomic Cu zone has also been observed at George Fisher (Part B).

Chemical analyses illustrate that these carbonates fall within three groups; calcites, siderite-magnesite solid solutions and dolomite-ankerite solid solutions (Figs 15 and 16). Comparison with George Fisher and Hilton carbonates illustrates that;

1. Mount Isa calcites contain lower total $(Fe,Mn)CO_3$ (Fig. 15).
2. All dolomite-ankerites plot with constant $FeCO_3/MnCO_3$ along a positive linear trend that closely approximates the minimum $FeCO_3/MnCO_3$ defined by Stage OI early dolomites at George Fisher. However, they do not exhibit a similar broad range of $FeCO_3$ and $MnCO_3$ contents that distinguishes Stage OI early dolomites (Fig. 16a and b).
3. Magnesites cluster on a plot of $MnCO_3$ versus $FeCO_3$ and lie at the edge the field defined by Stage VIII ferroan carbonates at George Fisher and Hilton. However, they define a near-vertical field on a plot of $(FeCO_3/MnCO_3)$ versus $MgCO_3$, distinct from all George Fisher and Hilton carbonates (Fig. 16a and b).

STABLE ISOTOPE GEOCHEMISTRY

SAMPLING AND METHODS

Whole-rock carbonate samples were collected from a range of rock types for carbon and oxygen stable isotopic investigations. These include Stage OI early dolomites from banded and medium-bedded mudstone intervals, Stage I calcite from white bands, nodular layers and medium-bedded mudstones, and Stage VIII ferroan carbonates from nodular layers and banded mudstone intervals (e.g. Fig. 17). The majority of Stage OI and I carbonates were sampled from the southern portion of the I stratigraphic interval which is characterized by an abundance of early carbonates and subeconomic Zn-Pb-Ag mineralization (Fig. 17). A significant number of white band calcite or nodular layer calcite and whole rock mudstone dolomite were derived from adjacent layers (Fig. 18). Stage VIII carbonates were sampled from a localized Stage VIII alteration pod in the H stratigraphic interval and within hanging wall zone of pervasive subeconomic Cu mineralization (Figs 17 and 18).

Additional Stage OI and I carbonates from adjacent bands and beds were sampled from a poorly mineralized interval from the C stratigraphic zone collection (Figs 17 and 19) peripheral and up-dip from both the main Zn-Pb economic zone and a Stage VIII ferroan carbonate -enriched interval at 7540mN and 7660mN (see Fig. 1). The drill core samples were taken from the thesis collection of Clark (1993).

Carbonates were analysed at the University of Queensland Stable Isotope Geochemistry Laboratories using the orthophosphoric extraction method of McCrea (1950) and acid fractionation factors of Sharma and Clayton (1965) and Rosenbaum and Sheppard (1986). Analytical uncertainties are within ±0.1‰. $\delta^{18}O$ is reported with respect to SMOW and $\delta^{13}C$ is reported with respect to PDB (Appendix V).

RESULTS

Whole rock carbonate isotope analyses define three separate fields on a $\delta^{18}O$ versus $\delta^{13}C$ plot (Fig. 20). Stage OI dolomites from the I stratigraphic interval exhibit narrow ranges of $\delta^{18}O$ from 18.0 to 18.5‰ and $\delta^{13}C$ from -3.8 to -2.6‰. Stage I calcites closely approximate Stage OI dolomites with $\delta^{18}O$ from 17.1 to 18.0‰ and $\delta^{13}C$ from -4.1 to -1.7‰. Stage I calcites have similar to lower $\delta^{18}O$ and a broader range of $\delta^{13}C$ than Stage OI early dolomites.

Samples from the C stratigraphic interval display quite different isotopic trends and plot in a field in which $\delta^{18}O$ and $\delta^{13}C$ covary positively. Samples from this zone have consistently lower $\delta^{18}O$ than equivalent Stage OI dolomites and Stage I calcites in the I ore zone, although a single Stage I calcite from the I interval displays similar values to Stage OI early dolomites in the C interval. C stratigraphic interval Stage OI dolomites are enriched in $\delta^{18}O$ relative to calcite sampled from adjacent white bands and nodular layers, and exhibit minor isotopic variability. In contrast, calcite samples from white bands and nodular layers adjacent to Stage OI dolomite layers display the broadest range of $\delta^{18}O$ of 13.0 to 16.2‰. $\delta^{13}C$ in Stage OI dolomites ranges from -1.7 to -1.4‰ compared to $\delta^{13}C$ of -2.8 to -1.3‰ in Stage I calcites. A third field on the plot is wedge-shaped, is defined by Stage VIII ferroan carbonates and falls between the fields defined by early carbonates (Fig. 20).

COMPARISON WITH OTHER CARBONATES IN THE MOUNT ISA AREA

Carbonate $\delta^{18}O$ and $\delta^{13}C$ analyses of Stage V syntectonic vein-filling sugary ferroan dolomites, a Stage IXa chalcopyrite-dolomite vein and Stage VIII equivalent carbonates from Hilton Mine (Valenta, 1988), and Lake Moondarra area (Waring, 1990a) are plotted

for comparison (Fig. 21). Fields defined by data collected from the Mount Isa deposit are also illustrated (Waring, 1990a). The latter include analyses of silica-dolomite at variable northings within the mine and analyses of whole rock Urquhart Shale 'dolomites' that were sampled at various distances from economic Cu mineralization.

Whole rock and vein-filling carbonates in the Mount Isa mineralization system display a broad range of $\delta^{18}O$ and $\delta^{13}C$ and some systematic spatial variation. Groupings are summarized below and listed in accordance with nomenclature on Figure 21;

1 - 4. Mount Isa silica-dolomite samples exhibit greatest variation in $\delta^{18}O$ and $\delta^{13}C$ and the majority of samples, except for northernmost samples (4), are depleted in $\delta^{18}O$ and $\delta^{13}C$ relative to whole rock and vein-filling carbonates from George Fisher, Hilton and Lake Moondarra. Samples from southern portions of the Cu ore system exhibit greatest relative depletion.

5 - 9. The majority of whole rock Urquhart Shale dolomite samples are relatively depleted in $\delta^{18}O$ but display a similar range of $\delta^{13}C$ compared with carbonate samples from Hilton, George Fisher and Lake Moondarra except for distal Urquhart Shale dolomites sampled 4km south of Mount Isa Mine (Group 9, Fig. 21).

10 - 12. Hilton and George Fisher whole rock and vein-filling Stage VIII ferroan carbonates associated with subeconomic Cu mineralization, Stage OI and I equivalent carbonates from George Fisher north, and syn- to late-tectonic carbonate vein-fill occur within these fields. They are grouped together here as all the carbonates exhibit positive covariation of $\delta^{18}O$ and $\delta^{13}C$ signatures. Samples with lowest $\delta^{18}O$ and $\delta^{13}C$ overlap with fields defined by Mount Isa carbonates.

13. Stage OI and I whole rock dolomites and calcites sampled from the I stratigraphic interval and a single sample from Hilton Mine of an early vein-filling carbonate define a niche separated in $\delta^{18}O$ and $\delta^{13}C$ space from all other carbonate populations. The population is characterized by a narrow range of enriched $\delta^{18}O$ and $\delta^{13}C$ compared with Mount Isa and Hilton samples. The population is further distinguished by a lack of covariation of $\delta^{18}O$ and $\delta^{13}C$.

14. Samples from the Lake Moondarra area are representative of Urquhart Shale whole rock dolomite constituents furthest removed from Zn-Pb-Ag and Cu mineralization and are enriched in $\delta^{18}O$ compared with all other carbonates (Waring, 1990a).

DISCUSSION AND CONCLUSIONS

The study is the first to systematically examine characteristics of carbonates throughout the Mount Isa system as a whole. Thus, the main objectives of this discussion are to;

1. Examine causes for carbonate variations within the Mount Isa area in light of textural and chemical data derived from George Fisher carbonates, textural data, and carbonate-mineralogical associations at Hilton and Mount Isa.

2. Introduce a model that can be used to explain the heterogeneous development of carbonate minerals throughout the Urquhart Shale in the Mount Isa area, but furthermore, can enable workers to locate themselves in the system based on carbonate textures, mineralogical associations and chemical signatures.

SIGNIFICANCE OF VARIATION OF CARBONATE TYPES IN THE MOUNT ISA AREA

A huge range of texturally and chemically distinctive carbonate types constitute the Urquhart Shale in the Mount Isa mineralization system and are variably associated with carbonate vein systems. Three broad populations are distinguished on the basis of carbonate chemistry and paragenesis, and can be temporally linked with either Zn-Pb-Ag or Cu mineralization.

The oldest carbonates recognized as major constituents of the Urquhart Shale are replacive in origin and include Stage OI early dolomites and Stage I calcite at George Fisher and texturally equivalent carbonates in portions of the Urquhart Shale distal to Mount Isa Mine. Stage I calcite is the dominant constituent of layer parallel white bands and nodular layers in these stratigraphic intervals. Several key chemical and textural associations elucidate the origin of these early carbonate types.

Stage OI early dolomites

Dolomitization can occur under a range of physiochemical conditions in near-surface, shallow and deep burial diagenetic realms from a range of fluid types (e.g. Hardie, 1987; Purser et al., 1994; Malone et al., 1996). As a result, the textural and chemical characteristics of dolomites can be used to fingerprint environmental settings (e.g. Brand and Veizer, 1980; Curtis et al., 1986; Machel, et al., 1996). The main question surrounding the origin of early dolomites is whether these represent sequential periods of dolomite growth from separate episodes of fluid flow in changing diagenetic realms, or whether they represent a continuum of dolomite growth associated with a single dolomitization event (cf. Winter et al., 1995).

The Fe-rich nature of all Stage OI early dolomites is typical of burial diagenetic carbonates derived from reduced basinal fluids (e.g. Simo et al., 1994; Winter, et al., 1995). Furthermore, the absence of a textural hiatus between core dolomites and inner rim ankerites such as dolomite grain dissolution or precipitation of other authigenic mineral phases suggests that early dolomites may have formed as part of a progressive

dolomitization event (cf. Montañez, 1994). Variation in $(Fe,Mn)CO_3$ content of each successive generation of carbonate growth probably reflects fluctuating redox conditions (e.g. Dromgoole and Walter, 1990; Montañez, 1994). However, Stage OI rim and matrix dolomites in distal Urquhart Shale are relatively depleted in Fe and Mn relative to texturally equivalent Stage OI early dolomites at George Fisher. This suggests that dolomitizing fluids were consistently depleted in $Fe^{2+}(aq)$ and $Mn^{2+}(aq)$ when they reached the latter site of dolomite precipitation. Relative depletion of $(Fe,Mn)CO_3$ in carbonates of the magnitude exhibited by distal carbonates is not typically reported for dolomites formed as a result of regional-scale fluid flow generated as a natural consequence of mineral diagenesis and burial (e.g. Moore, 1990). However, zoning of $(Fe,Mn)CO_3$ in carbonates, at a scale of metres to kilometres is reported for several sediment-hosted Zn-Pb-Ag deposits in the Western Mount Isa Inlier and McArthur Basin and interpreted to reflect proximity to sites of economic mineralization (e.g. Hinman, 1996; Large and McGoldrick, 1998). Thus, while the $(Fe,Mn)CO_3$ of early dolomites is consistent with dolomitization during burial diagenesis, zoning of the carbonates more closely approximates patterns of hydrothermal mineralization in the region.

Stage I Calcite

It is clear that calcite occurs as a replacement of dolomite in the Mount Isa area irrespective of the textural setting of calcite. Calcitization of dolomite (dedolomites) has been widely documented and is generally regarded as the product of either;

1. The influx of meteoric waters at regional erosional surfaces or as a result of tectonic uplift (e.g. Theriault and Hutcheon, 1987; Lee and Harwood, 1989; Morse and Mackensie, 1990).
2. Ca-rich basinal brine influx derived from hydrocarbon generation (e.g Budai et al., 1984).

The singlemost important criterion for calcite rather than dolomite precipitation is low aMg^{2+}/aCa^{2+} in solution (e.g. Hardie, 1987). This is accounted for in the above models by increasing the availability of $Ca^{2+}(aq)$ by the introduction of meteoric-derived

groundwaters and/or by the reduction of sulphate evaporites during hydrocarbon generation.

Addition of Ca^{2+}(aq) from meteoric-derived groundwaters seems unlikely due to;

1. the lack of evidence of uplift during calcite formation or development of any extensive erosional surface in the Upper Mount Isa Group prior to chemical compaction,
2. the absence of iron oxide precipitation as a result of oxygenated groundwater influx (cf. Lee and Harwood, 1989).

Thus, it is more probable that calcites were derived from basinal brines or alternatively the source of Ca^{2+}(aq) was derived from *in situ* sulphate evaporites. Nodular carbonates developed in rhythmically laminated pyritic siltstones have previously been interpreted to be pseudomorphous after primary sulphate evaporites (Neudert, 1983, Clark, 1993). The formation of void-filling calcite in nodular layers and evidence for an additional precursor host rock component illustrated by a comparison of whole rock mineral abundance comparisons (Part B, Fig. 6) are fundamental differences exhibit by these layers. A model proposing dissolution and replacement of a preexisting sulphate evaporite precursor could account for these variations and the onset of Stage I calcite alteration. However, no sulphate relicts have been recorded in nodular bands, and calcites from all textural settings are chemically equivalent and isotopically indistinguishable. Similarities in isotopic composition in particular are difficult to explain if*in situ* sulphate evaporites were precursors to nodular calcite specifically.

A basin-derived fluid source is preferred for Stage I calcite alteration. Thus, whilst the displacive habit of nodular calcite is similar to sulphate evaporites, it is more probable that variation in textural setting of Stage I calcites reflects primary variations in permeability and porosity characteristics of host layers. Nodular layers were probably more porous (rather than containing an additional, undetected precursor mineral) which could account for volume differences revealed by comparison of whole rock mineral abundances in

different calcitic layers. Similar displacive nodular carbonate growth has been described from the McArthur River Zn-Pb-Ag deposit (Hinman, 1996).

Significance of chemical zonation

Zoning is exhibited by Stage I calcites and mimics patterns exhibited by Stage OI early dolomites. However, calcites are enriched in $(Fe,Mn)CO_3$ relative to ferroan or manganiferous calcites typically reported to have formed from meteoric-derived or basinal fluids (e.g. Lee and Harwood, 1989). This suggests that Stage I calcites could have been derived from fluids anomalously rich in Fe^{2+} and Mn^{2+} that may have been similar to Stage OI dolomitizing fluids. Furthermore, the similarity in chemical characteristics of Stage III vein-filling dolomites and Stage OI early dolomites and near identical $(Fe,Mn)CO_3$ contents of Stage I calcites and Stage III vein-filling calcites suggests that all pre- Zn-Pb-Ag mineralization carbonates were derived from a similar source region. Thus, precipitation of calcite versus dolomite probably reflects evolving mineral diagenesis within the source region or along the migrating fluid pathway, while similar chemical characteristics illustrate that fluid channelling from this source occurred over a potentially protracted period.

Syntectonic, Cu-related carbonate types

This carbonate population includes Stage VIII ferroan carbonate veins and alteration at George Fisher and chemically equivalent replacement and vein-filling carbonates at Hilton Mine. Stage VIII ferroan carbonates represent the dominant carbonate rock-forming constituent of Cu mineralized zones at Hilton and George Fisher and probably represent a significant proportion of carbonates that host Zn-Pb-Ag mineralization at Mount Isa (cf. Stanton, 1963).Their formation is interpreted to be intimately linked with the Cu mineralization event (cf. Valenta, 1988).

Stage V sugary ferroan dolomite veins at George Fisher post-date Zn-Pb-Ag mineralization and can be differentiated from earlier carbonates on the basis of $FeCO_3$ /$MnCO_3$ ratios. Silica-dolomite veins and alteration that host economic Cu mineralization

at Mount Isa are the only other group, out of all other carbonates, that exhibit similar positive covariation of Mn and Fe and consistent Fe/Mn ratios. This association suggests fundamental links between sugary dolomite vein formation at George Fisher and silica-dolomite formation at Mount Isa.

These two carbonate populations identified in association with Cu formation within the Mount Isa system can be further differentiated on the basis of mineralogical associations and carbonate textures. The majority of Stage VIII ferroan carbonates at Hilton and George Fisher are replacive and fine-grained. They can not be distinguished from Stage OI early dolomites at a hand specimen scale on the basis of grain size alone and associated ferroan carbonate veining is not always evident. However, they typically occur in association with Stage VIII phyllosilicate alteration. In contrast, carbonates associated with the silica-dolomite hydrothermal system are coarse-grained, and occur as breccia matrix, vein infill or porphyroblastic-style replacement. Phyllosilicate-carbonate veining is reported to occur within the silica-dolomite alteration envelope at Mount Isa (e.g. Waring, 1990a). However, stratabound phyllosilicate alteration zones are more commonly superimposed on Zn-Pb-Ag -bearing host rocks at the margins of the silica-dolomite envelope commonly in association with sideritic mudstones and siltstones (e.g. Swager et al., 1987; Wilkinson, 1995). It seems quite plausible that ferroan carbonates in these horizons are equivalent to Stage VIII ferroan carbonates at Hilton and George Fisher.

At least two fluid types have been reported to accompany initial dolomite formation during Cu formation, and are represented by brine-derived $CaCl_2$-rich and metamorphic-derived CO_2-rich fluid inclusion populations whilst NaCl-rich fluid inclusions represent fluids accompanying the main stage of Cu formation and silicification (Heinrich et al., 1989). No fluid inclusion studies have been conducted on Stage VIII ferroan carbonates at Hilton and George Fisher or on siderites from Mount Isa Mine. However, it is plausible that the separation of Cu-related carbonates into two chemically distinct populations could be a result of their precipitation from fluids of different composition and origin (cf. Heinrich et al., 1989).

Interpretation of stable isotope geochemistry

The majority of Mount Isa region carbonates define an inverted L-shaped trend on a plot of $\delta^{18}O$ and $\delta^{13}C$ (Fig. 21). Samples from the Lake Moondarra area are interpreted to represent the most isotopically pristine examples of Urquhart Shale (Waring, 1990a) and have heaviest $\delta^{18}O$ signatures compared with all other carbonates. Silica-dolomite carbonates and carbonate constituents of the Urquhart Shale at Mount Isa Mine represent a relatively $\delta^{18}O$- and $\delta^{13}C$ -depleted population whilst the majority of Hilton and George Fisher carbonates can be grouped as moderately depleted with respect to $\delta^{18}O$ and $\delta^{13}C$. However, samples from the I stratigraphic interval and a single vein sample from Hilton Mine plot within a near vertical field and are enriched in $\delta^{18}O$ compared with the latter groups.

Relative depletion of $\delta^{18}O$ and $\delta^{13}C$ of carbonates from Hilton and Mount Isa has been interpreted to be the product of mixing of isotopically light Cu-bearing fluids with isotopically heavier carbonate rocks under variable fluid/rock ratios (Valenta, 1988; Waring, 1990a; Fig. 21). Thus, variation in distribution of carbonates with respect to the inverted L-shaped on a plot of $\delta^{18}O$ versus $\delta^{13}C$ reflects variable fluid/rock ratios. The relatively less-depleted values at Hilton and George Fisher correlate with lower abundances of Cu mineralization and thus, significantly less volumes of fluid (cf. Valenta, 1988). It should be noted that this interpretation was made without clear constraints on temperature conditions in the Hilton area (Valenta, 1988). It is now evident that temperatures to the north of the system were in the order of 250-300°C (Part B) compared with estimates in the order of 300-350°C at Mount Isa (e.g. Waring, 1990b). However, the range of $\delta^{18}O$ from approximately 10‰ at Mount Isa to 17‰ at George Fisher cannot be explained by the mixing of a fluid of fixed isotopic composition at

different temperatures (cf. Heinrich, et al., 1989), which reaffirms the role of variable fluid/rock ratios.

Isotopic trends exhibited by late-stage ferroan carbonates and carbonates from the C stratigraphic interval from George Fisher lie along the Cu system mixing trend. This accords with the temporal association of late ferroan carbonates and Cu mineralization but not with the chemical signature of C stratigraphic interval carbonates.

The most striking aspect of the George Fisher isotope study is the separation of Stage OI and I carbonates into two discrete and separately trending fields. The only physical differences evident between the two sample sets, other than their stratigraphic setting and location within the deposit, is the development of a bedding perpendicular foliation in calcitic layers from the C stratigraphic interval. It is possible that carbonates from the C stratigraphic interval recrystallized during deformation and that isotopic reequilibration with syntectonic Cu-bearing fluids ensued. The difference in isotopic composition of dolomites and calcites from adjacent layers in the C stratigraphic interval cannot be explained by equilibrium isotopic fractionation between dolomite-calcite pairs at relatively high temperatures (cf. Friedman and O'Neil, 1977) and is also inconsistent with disequilibrium recrystallization at constant temperature. Thus, variation in isotopic characteristics of calcite and dolomite in adjacent layers from the C interval is interpreted to be the product of variable fluid/rock ratios at a centimetre-scale. The fact that the chemistry of these carbonates mimics that of the I stratigraphic interval implicates the decoupling of chemical and isotopic alteration envelopes at George Fisher associated with bedding-scale fluid flow (cf. Bickle and Chapman, 1990; Cartwright, 1997).

An inverted L-shaped trend can also be defined between Lake Moondarra samples and George Fisher I stratigraphic interval carbonates (Fig. 21). However, the near-vertical isotopic trend and higher $\delta^{18}O$ of Stage OI and I carbonates from the I stratigraphic interval can not be explained by variable mixing with the same Cu-bearing fluid. This

pattern is interpreted to reflect diagenetic signatures not previously recognized in the Mount Isa system.

Isotopic shifts to lower $\delta^{18}O$ in burial diagenetic systems are generally interpreted to reflect the infiltration of relatively hot basinal brines (e.g. Montañez, 1994). In such systems, shifts in $\delta^{18}O$ of the order of 4‰, as exhibited by samples from Lake Moondarra to George Fisher, are typical. However, the narrow range of $\delta^{18}O$ (i.e. 1.5‰) is restricted compared with normal burial trends (cf. Heydari, 1997). This could reflect the relatively close proximity of samples at George Fisher. Similarly, shifts to lower $\delta^{13}C$ could be produced by incorporation of a small component of fluid-derived, light organic $\delta^{13}C$ during dolomite formation or simply be a manifestation of the proximity of data points. Thus, isotope geochemistry can be interpreted to be consistent with normal burial diagenetic trends. However, this interpretation assumes that whole rock carbonate samples in the Lake Moondarra area formed prior to Stage OI and I carbonates at George Fisher and that the latter carbonates formed at burial depths in the order of kilometres (cf. Dix, 1993; Montañez, 1994).

No detailed textural or chemical data are available for samples from the Lake Moondarra area. However, dolomite constituents of the Urquhart Shale there are reported to be ferroan and texturally similar to those described from the Mount Isa area (Neudert, 1983). Thus it is quite possible that these carbonates are paragenetically equivalent to early dolomites at George Fisher. If this is the case, then differences in $\delta^{18}O$ are more likely to be the product of fluid cooling. The locus of fluid infiltration would likely have been in the vicinity of the George Fisher deposit.

It seems unlikely that Stage OI and I carbonates formed at depths greater than several hundreds of metres based on depth constraints for the onset of chemical compaction (Part

B). This would suggest that burial trends exhibited by Stage OI and I carbonates actually reflect the infiltration of thermally anomalous fluids into a shallowly buried sedimentary pile. Evidence for fluid cooling at a district scale would be predicted from such a scenario and greatest $\delta^{18}O$ depletion would correlate with zones proximal to the infiltrating fluid source. Thus, whilst more detailed comparisons are required, the current data set supports the hypothesis that the earliest recognized carbonate constituents of the Urquhart Shale were derived from warm fluids with light organic-derived carbon, and that the locus of these fluids was proximal to economic Zn-Pb-Ag mineralization (cf. Mountjoy et al., 1997).

ORIGIN OF SYNDIAGENETIC CARBONATES

Geochemical signatures of syndiagenetic major host rock carbonate constituents of the Urquhart Shale independently implicate locally introduced hydrothermal fluids. Furthermore, geochemical halos defined by decreasing $(Fe,Mn)CO_3$ contents in paragenetically-equivalent carbonates and $\delta^{18}O$ depletion halos can be interpreted to mantle fluid influx zones in the vicinity of economic Zn-Pb-Ag mineralization. This suggests that syndiagenetic carbonates and Zn-Pb-Ag mineralization formed as part of a single, evolving hydrothermal system.

SIGNIFICANCE OF HETEROGENEOUS CARBONATE DISTRIBUTION PATTERNS

This study is the first to document detailed textural, chemical, paragenetic and isotopic characteristics of syndiagenetic carbonates from the Mount Isa system and demonstrate that these carbonates represented dominant constituents of Zn-Pb-Ag -bearing Urquhart Shale. Furthermore, the study demonstrates that late-stage ferroan carbonates associated with Cu mineralization at George Fisher can be chemically and texturally distinguished from earlier carbonates, and that the absence of Stage II calcite in portions of stratigraphy at George Fisher is a result of calcite replacement by Stage VIII ferroan carbonates.

It is proposed that syndiagenetic carbonates were developed throughout the Mount Isa area in zones affected by warm infiltrating fluids. However, distribution patterns defined by these carbonates were obscured by the heterogeneous development of syn- to late-tectonic Cu mineralization. Where this second hydrothermal event was intense it appears to have resulted in pervasive syntectonic ferroan carbonate alteration at Mount Isa Mine and widespread alteration at Hilton. In contrast, the paucity of Cu mineralization, combined with additional preservation of footwall stratigraphic intervals produced a window of abundant syndiagenetic carbonate preservation with economic Zn-Pb-Ag mineralization at George Fisher not previously recognised. Thus, the Cu mineralization can account for;

1. The heterogeneous development of calcite throughout the Mount Isa system and in particular its preservation in zones distal to economic Cu mineralization.
2. The dominance of nodular dolomite at Hilton and Mount Isa reflecting alteration of syndiagenetic calcite during Cu mineralization.
3. The abundance of siderite and ankerites in association with stratabound phyllosilicate alteration in Zn-Pb-Ag horizons at Mount Isa, Hilton and George Fisher as a direct result of Cu mineralization.
4. The inability of previously invoked carbonate origins to account for carbonate-metal associations throughout the Mount Isa system (Table 4).

Distribution of mineralogical products associated with the Zn-Pb-Ag versus Cu hydrothermal systems in the Mount Isa area are summarized (Table 4 and Fig. 22). These data account for the variation in distribution of carbonate constituents of the Urquhart Shale at the Mount Isa, Hilton and George Fisher deposits, predict paragenetic associations based on mineral distribution patterns at Mount Isa and Hilton and further provide criteria that can be used to predict the extent of hydrothermal superposition and proximity to economic zones of Cu mineralization (Fig. 22). Thus, it is probable that the lack of consensus surrounding the origin of Zn-Pb-Ag and Cu mineralization at Mount Isa, and in particular the current trend to account for metal accumulation as part of a single, syntectonic hydrothermal event, is a product of the even greater scale of

development of the Cu mineralization system at Mount Isa than previously recognized. In summary;

1. The large-scale infiltration of relatively hot, Cu-bearing fluids at Mount Isa produced deposit-wide replacement of syndiagenetic carbonates by syntectonic ferroan carbonates throughout Zn-Pb-Ag-bearing strata and selective development of high-temperature phyllosilicate alteration assemblages. Later alteration assemblages probably developed in, and masked evidence of, preexisting syndiagenetic Ba-K-feldspar alteration zones similar to those developed at George Fisher.

2. Thus, the inability to differentiate between those products formed during Zn-Pb-Ag versus Cu mineralization events within the Zn-Pb-Ag-bearing strata at Mount Isa has retarded resolution of the controversy surrounding Mount Isa - style Zn-Pb-Ag and Cu ore genesis (cf. Perkins, 1997).

CONCLUSIONS

The key conclusions of this study can be summarized in brief as follows;

Nature of the Urquhart Shale

1. The Urquhart Shale at George Fisher is distinguished by abundant planar and nodular carbonate bands and paucity of black shale in the immediate host rocks to mineralization compared with the Hilton and Mount Isa deposits.

2. The large-scale intercalation of rhythmically laminated pyritic siltstones and medium-bedded, stylolitic mudstones is the major sedimentological characteristic common to sites of economic Mount Isa-style Zn-Pb-Ag accumulations.

3. The earliest preserved carbonates in the Urquhart Shale and locally abundant carbonate bands are products of syndiagenetic hydrothermal alteration.

4. The original sedimentary sequence probably consisted of alternating, mixed carbonate and siliciclastic, laminated carbonaceous siltstones, and variably-bedded mudstones with either locally abundant black shale, reflecting variations in organic accumulations, or abundant black shale intervals that were heterogeneously preserved as a result of variations in organic preservation potential.

Syndiagenetic Hydrothermal Zn-Pb-Ag System

5. The George Fisher deposit was the locus of intense hydrothermal activity that was initiated early during the burial history of the Urquhart Shale and culminated in the precipitation of Mount Isa-style Zn-Pb-Ag mineralization prior to the onset of tectonic uplift during the Diamantinan Orogeny.

6. A model age of ~1653Ma, which approximates the age of the host sedimentary sequence, has been derived for the timing of Zn-Pb-Ag mineralization from Pb-isotope compositions.

7. Hydrothermal fluid infiltration initially produced district-wide ferroan dolomitization followed by texturally distinctive forms of calcite alteration. Geochemical signatures of earliest carbonates record the infiltration and dispersion of warm, basin-derived fluids into a cool sedimentary pile.

8. Chemical zonation of the earliest carbonate alterations is defined by decreasing $(Fe,Mn)CO_3$ contents with increasing distance from Zn-Pb-Ag ores resembling relationships at other sediment-hosted deposits in the Mount Isa-McArthur region.

9. Earliest carbonates exhibit C/O isotopic zonation defined by increasing $\delta^{18}O$ and $\delta^{13}C$, with increasing distance from economic Zn-Pb-Ag mineralization at a scale of 10 to 20km.

10. Pyritization of the sequence post-dated early carbonate alteration, was the first episode of sulphide precipitation, and occurred as a result of thermochemical sulphate reduction by *in situ* organic material. Fluids were deficient in ore metals at this time.

11. Celsian-hyalophane-K-feldspar and carbonate vein development was probably localized in the vicinity of the fluid influx region and preceded and structurally prepared the sedimentary sequence for precipitation of high grade Zn-Pb-Ag ore.

12. Sphalerite and galena deposition was accompanied by a second generation of pyrite alteration, bitumen emplacement and hydrophlogopite alteration. The bulk of economic mineralization is breccia-vein -hosted.

13. Metals were transported in slightly oxidized, near neutral fluids either as chloride or organometallic complexes. Sulphur was either transported as sulphate with metals, or as sulphide in a separate fluid. Metal precipitation occurred as a result of thermochemical sulphate reduction by methane or as a result of fluid mixing.

14. The diversity, and deposit zonation of galena and sphalerite mineralization styles results from primary variations in the porosity and permeability characteristics of host layers combined with heterogeneous development of folding at a deposit-scale and preferential strain accommodation by galena during the Isan Orogeny.

15. The deposit was vertically zoned prior to regional deformation, from a Zn-rich base, through a relatively Pb-rich core to a mixed Zn-Pb -rich top and each mineralized stratigraphic interval was laterally zoned from Pb to Zn, and from higher to lower metal grades. The zonation preserves a record of syndiagenetic hydrothermal fluid infiltration sourced from the southwest despite the effects of regional deformation.

16. Peak temperatures during mineralization have been estimated to be ~200°C from bitumen reflectance data. The development of mesophase textures in these bitumens further indicates that this was the maximum temperature that would have been attained during burial metamorphism of the sedimentary sequence.

17. The general assumption that the host Urquhart Shale was metamorphosed to greenschist facies is no longer sustained and thus, it is further possible that the sedimentary sequence was buried to depths of no more than 2 or 3km prior to tectonic uplift.

Late-tectonic Cu system

18. Temporal-spatial-temperature zonation and metal zonation from Zn to Pb to Cu (with increasing stratigraphic age) at the George Fisher deposit is the result of partial superposition of syn- to late-tectonic Cu mineralization ~75-125Ma after syndiagenetic Zn-Pb-Ag mineralization.

19. The major manifestations of Cu mineralization include locally abundant pyrrhotite alteration and biotite-chlorite -dominant phyllosilicate alteration. These occur in

stratabound zones in the hanging wall portions of the sequence superimposed on preexisting Ba-feldspar alteration zones, and ferroan dolomite-ankerite -dominant carbonate alteration. The latter carbonates are pervasive throughout the hanging wall portions of the sequence and are locally abundant in the footwall sequences.

20. Late stage ferroan dolomite-ankerite -dominant carbonate alteration can be texturally, chemically and isotopically distinguished from the earliest carbonate alterations that preceded Zn-Pb-Ag mineralization.

21. Copper-bearing fluids at George Fisher had temperatures of ~250-300°C based on phyllosilicate mineral stability relationships.

Comparison with Mount Isa Zn-Pb-Ag and Cu .

22. Copper-bearing fluids at George Fisher were some ~30-80°C cooler than estimated temperatures for infiltrating Cu-bearing fluids at Mount Isa Mine. Temperature variations are manifested by variation in phyllosilicate mineral associations within the Mount Isa district.

23. Variation in textural and geochemical characteristics of carbonate constituents of the Urquhart Shale at Mount Isa reflect greater abundance of ferroan carbonate formation accompanying intense, syn- to late-tectonic Cu mineralization.

24. Variations in carbonate types throughout the Mount Isa district illustrate that extensive Copper mineralization at Mount Isa probably resulted in the complete reconstitution of syndiagenetic Zn-Pb-Ag mineralization signatures at a mine-scale. Infiltration of Cu-bearing fluids at Mount Isa Mine produced large-scale replacement of syndiagenetic hydrothermal carbonates and concomitant resetting of chemical and C/O isotope compositions of these early carbonates.

25. Variation in sulphur isotope geochemistry of sphalerite and galena in the Mount Isa district could be a product of sulphur isotope homogenization as a result of deposit-scale infiltration of Cu-bearing fluids at Mount Isa Mine.

26. The poor preservation of syndiagenetic Zn-Pb-Ag mineralization signatures at Mount Isa Mine and thus inability of previous workers to clearly differentiate between hydrothermal products associated with Zn-Pb-Ag versus Cu mineralization events accounts for much of the controversy surrounding the origin of Mount Isa-style Zn-Pb-Ag and Cu mineralization at Mount Isa.

Further work

This study represents the first detailed examination of the geology and genesis of the George Fisher deposit. Topics recommended for future research here follow from the key conclusions made and are proposed for the Mount Isa mineralization system as a whole.

1. It is recommended that further examination of organic matter characteristics is undertaken to determine;

(a) whether maturity levels and textural characteristics of migrabitumens can be used as Zn-Pb-Ag versus Cu exploration vectors in the Mount Isa district.

(b) the origin of texturally zoned bitumen grains which are reported in association with sediment-hosted Zn-Pb-Ag deposits, but for which the origin of such textures is not constrained in the current body of literature.

2. Examination of textural characteristics of galena to determine whether original textural relationships between galena and sphalerite can be constrained. If so, then better constraints can be placed on fluid evolution during the Zn-Pb-Ag event and metal distribution patterns could then be modelled in terms of fluid flow. Such a model may be of use in predicting the extent of ore development at a deposit-scale.

3. It is recommended that the sulphur isotope geochemistry of ores at George Fisher is evaluated in more detail to further constrain syndiagenetic hydrothermal fluid characteristics and reconcile variations in sulphur isotope geochemistry between George Fisher and Mount Isa.

4. Further constraints on fluid chemistry and ore-forming conditions could be derived from a fluid inclusion study of Stage III carbonate±quartz±Ba-K-feldspar veins and Stage IV sphalerite at George Fisher if suitable fluid inclusions can be located. Such a study could potentially add substantially to the understanding of partitioning of Ba into feldspars, particularly at low temperatures.

5. There is an abundance of data that indicates extensive resetting of chemical and isotopic resetting of Zn-Pb-Ag mineralization signatures at Mount Isa Mine. This raises the question of whether ores at Mount Isa are situated in original sites of metal precipitation or whether ore was substantially mobilized during the Cu event. It is recommended that microbeam technologies are utilized to probe Zn and Pb concentrations in Cu-stage quartz-hosted fluid inclusions across the Cu to Pb-Zn transition at Mount Isa Mine to establish whether large amounts of Zn and Pb could have been mobilized by syn-late tectonic Cu-bearing fluids. This study should be undertaken in conjunction with analysis of sulphide textural styles and distribution patterns across the Cu to Pb-Zn transition, similar to that applied at George Fisher, to ascertain potential scales of metal redistribution.

REFERENCES

Aldroyd, G., 1998, George Fisher project -feasibility study summary: Unpublished MIM Ltd report, 82p.

Anderson, G.M., 1973, The hydrothermal transport and deposition of galena and sphalerite near 100°C: Economic Geology, v. 68, p. 480-492.

Anderson, G.M., 1975, Precipitation of Mississippi Valley-type ores: Economic Geology, v. 70, p. 937-942.

Anderson, G.M., 1991, Organic maturation and precipitation in Southeast Missouri: Economic Geology, v. 86, p. 909-926.

Anderson, G.M., and Garven, G., 1987, Sulphate-sulphide-carbonate associations in Mississippi Valley-type lead-zinc deposits: Economic Geology, v. 82, p. 482-488.

Anderson, G.M., and Macqueen, R.W., 1988, Mississippi Valley-Type Lead-Zinc deposits: *in* R.G. Roberts and P.A. Sheahan., eds., Ore Deposit Models, Geoscience Canada Reprint Series 3, p. 79-90.

Barker, C.E., and Pawlewicz, M.J., 1986, The correlation of vitrinite reflectance with maximum temperature in humic organic matter: *In:* Palaeogeothermics, Lecture Notes in Earth Sciences, 5, Springer, Berlin, p. 79-93.

Barker, C.E., and Goldstein, R.H., 1990, Fluid-inclusion technique for determining maximum temperature in calcite and its comparison to the vitrinite reflectance geothermometer: Geology, v. 18, p. 1003-1006.

Barnes, H.L., ed., 1997, Geochemistry of Hydrothermal Ore Deposits, Third Edition: John Wiley and Sons, Inc., New York, 972 p.

Barrett, T.J., and Anderson, G.M., 1982, The solubility of sphalerite and galena in NaCl Brines: Economic Geology, v. 77, p. 1923-1933.

Bates, R.L., and Jackson, J.A., eds., 1987, Glossary of Geology - Third Edition: Alexandria, Va., American Geological Institute, 769p.

Beales, F.W., 1975, Precipitation mechanisms for Mississippi Valley-type ore deposits: Economic Geology, v. 70, p. 943-948.

Beales, F.W., and Jackson, S.A., 1966, Precipitation of lead-zinc ores in carbonate rocks as illustrated by Pine Point ore field: Canadian Institute of Mining and Metallurgy Transactions, v. 75, p.B278-B285.

Bell, T.H., 1983, Thrusting and duplex formation at Mount Isa, Queensland, Australia: Nature, v. 304, p. 493-497.

Bell, T.H., and Hickey, K.A., 1998, Multiple deformations with successive sub-vertical and sub-horizontal axial planes: their impact on geometric development and significance for mineralization and exploration in the Mount Isa region: Economic Geology, v. 8, p. 1369-1389.

Bell, T.H., Perkins, W.G., and Swager, C.P., 1988, Structural controls on the development and localization of syntectonic copper mineralization at Mount Isa, Queensland: Economic Geology, v. 83, p. 69-85.

Benezeth, P., Castet, S, Dandurand, J., Gout, R., and Schott, J., 1994, Experimental study of aluminium-acetate complexing between 60 and 200°C: Geochimica et Cosmochimica Acta, v. 21, p. 4561-4571.

Bickle, M.J., and Chapman, H.J., 1990, Strontium and oxygen isotope decoupling in the Hercynian Trois Seigneurs Massif, Pyrenees: evidence for fluid circulation in a brittle regime: Contributions to Mineralogy and Petrology, v. 104, p. 332-347.

Blainey, G., 1960, Mines in the Spinifex - The story of Mount Isa Mines. Angus and Robertson Pty Ltd, 242 p.

Blake, D.H., 1987, Geology of the Mount Isa Inlier and environs, Queensland and Northern Territory: Australian Bureau of Mineral Resources, Bulletin 225, 83p.

Blake, D.H., Etheridge, M.A., Page, R.W., Stewart, A.J., Williams, P.R., and Wyborn, L.A.I., 1990, Mount Isa Inlier - regional geology and mineralization. *in* Hughes, F.E., ed., Geology of the Mineral Deposits of Australia and Papua New Guinea: Australasian Institute of Mining and Metallurgy, Monograph 14, p. 915-925.

Blake, D.H., and Stewart, A.J., 1992, Stratigraphic and tectonic framework, Mount Isa Inlier: Australian Geological Survey Organization Bulletin, n. 243, p. 1-11.

Blanchard, R., and Hall, G., 1942, Mount Isa ore deposition: Economic Geology, v. 32, p. 1042-1057.

Blount, C.W., 1977, Barite solubilities and thermodynamic quantities up to 300°C and 1400bars: American Mineralogist, v. 62, p. 942-957.

Brand, U., and Veizer, J., 1980, Chemical diagenesis of a multicomponent carbonate system-1:Trace Elements: Journal of Sedimentary Petrology, v. 50, p. 1219-1236.

Broadbent, G.C., Myers, R.M., and Wright, J.V., 1998, Geology and origin of shale-hosted Zn-Pb-Ag mineralization at the Century deposit, Northwest Queensland, Australia: Economic Geology, v. 93, p. 1264 - 1294.

Budai, J.M., Lohmann, K.C., and Owen, R.M., 1984, Burial dedolomite in the Mississippian Madison Limestone, Wyoming and Utah Thrust Belt: Journal of Sedimentary Petrology, v. 54, p. 276-288.

Carothers, W.W., and Kharaka, Y.K., 1978, Aliphatic acid anions in oil-field waters-Implications for origin of natural gas: American Association of Petroleum Geologists Bulleting, v. 62, p. 2441-2453.

Carter, S.R., 1953, Mount Isa Mines, *in* Edwards, A.B., ed., Geology of Australian Ore Deposits: 5th Empirical Mining and Metallurgical Congress, Melbourne, 1:361-377.

Carter, E.K., Brooks, J.H., and Walker, K.R., 1961, The Precambrian mineral belt of north-western Queensland: Bureau of Mineral Resources Bulletin, v.51.

Cartwright, I., 1997, Permeability generation and resetting of tracers during metamorphic fluid flow: implications for advection-dispersion models: Contributions to Mineralogy and Petrology, v. 129, p. 198-208.

Clark, D., 1993, Correlation of the Hilton Mine Block to the Hilton North Mine Block: Unpublished Honours Thesis, James Cook University, Townsville, Australia, 94p.

Connors, K.A., and Page, R.W., 1995, Relationships between magmatism, metamorphism and deformation in the western Mount Isa Inlier: Precambrian Research, v. 71, p. 131 - 153.

Cooke, D.R., and Large, R.R., 1998, Practical uses of chemical modelling - defining new exploration targets in sedimentary basins: Journal of Australian Geology and Geophysics, v. 17, p. 259-275.

Cox, S.F., 1987, Flow mechanisms in sulphide minerals: Ore Geology Reviews, v. 2, p.133-172.

Cox, S.F., Etheridge, M.A., and Wall, V.J., 1987, The role of fluids in syntectonic mass transport, and the localization of metamorphic vein-type ore deposits: Ore Geology Reviews, v. 2, p. 65-86.

Croxford, N.J.W., 1964, Origin and significance of volcanic potash-rich rocks from Mount Isa: Institute of Mining and Metallurgy Transactions, v. 74, p. 34-43.

Cumming G.L., and Richards, J.R., 1975, Ore lead isotope ratios in a continuously changing Earth: Earth and Planetary Science Letters, v. 28, p. 155-171.

Curtis, C.D., Coleman, M.L., and Love, L.G., 1986, Pore water evolution during sediment burial from isotopic and mineral chemistry of calcite, dolomite and siderite concretions. Geochimica et Cosmochimica Acta, v. 50, p. 2321-2334.

Dix, G.R., 1993, Patterns of burial- and tectonically controlled dolomitization in an Upper Devonian fringing-reef complex: Leduc Formation, Peace River Arch area, Alberta, Canada: Journal of Sedimentary Petrology, v. 63, p.628-640.

Domagala, J., McConachie, B., Neudert, M., and Page, R., 1998. Sequence stratigraphy of the Mount Isa Group. Geological Society of Australia Abstracts, No. 49, p. 117.

Dromgoole, E.L., and Walter, L.M., 1990, Iron and manganese incorporation into calcite: Effects of growth kinetics, temperature and solution chemistry: Chemical Geology, v. 81, p. 311-336.

Etheridge, M., and Wall, V., 1994, Tectonic and structural evolution of the Australian Proterozoic. Geological Society of Australia Abstracts, No. 37, p. 102-103.

Finlow-Bates, T., and Large, D.E., 1978, Water depth as major control on the formation of submarine exhalative ore deposits: Geologisches Jahrbuch, D.30: 27-39.

Finlow-Bates, T., and Stumpfl, E.F., 1979, The copper and lead-zinc-silver orebodies at Mt Isa Mine, Queensland: Products of one hydrothermal system: Annales de la Société Géologique de Belgique, v.102, p. 497-517.

Friedmann, I., and O'Neil, J.R., 1977, Compilation of stable isotope fractionation factors of geochemical interest: United States Geological Survey Professional Paper 440 - KK.

Forrestal, P.J., 1990, Mount Isa and Hilton silver-lead-zinc deposits: *in* Hughes, F.E., ed., Geology of the Mineral Deposits of Australia and Papua New Guinea: Australasian Institute of Mining and Metallurgy, Monograph 14, p. 927-934.

Frey, M., 1987, Low temperature metamorphism: Blackie and Son Ltd, London, 351p.

Giggenbach, W.F., 1981, Geothermal mineral equilibria: Geochimica et Cosmochimica Acta, v. 45, p. 393-410.

Gilligan, L.G., and Marshall, B., 1987, Textural evidence for remobilization in metamorphic environments: Ore Geology Reviews, v. 2, p. 205-229.

Giordano, T.H., 1992, Organic ligands and metal-organic complexing in ore fluids of sedimentary origin: *in* Lewan, M.D., and Pittmann, E.D., eds., The Role of Organic Acids in Geological Processes, p. 31-41.

Giordano, T.H., and Barnes, H.L., 1981, Lead transport in Mississippi Valley-type ore solutions: Economic Geology, v. 76, p. 2200-2211.

Giordano, T.H., and Drummond, S.E., 1991, The potentiometric determination of stability constants for zinc acetate complexes in aqueous solutions to 295°C: Geochimica et Cosmochimica Acta, v. 55, p. 2401-2415.

Goodarzi, F., Eckstrand, O. R., Snowdon, L., Williamson, B., and Stasuik, L.D., 1992, Thermal metamorphism of bitumen in Archaean rocks by ultramafic flows: International Journal of Coal Geology, v. 20, p. 165-178.

Grondijis, M.F., and Schouten, C., 1937, A study of the Mount Isa ores: Economic Geology, v. 32, p. 407-450.

Gustafson, L.B., and Williams, N., 1981, Sediment-hosted stratiform deposits of copper, lead, and zinc: Economic Geology 75th Anniversary Volume, p. 139-178.

Hall, G.E.M., Pelchat, J., and Loop, J., 1988, Separation and recovery of various sulphur species in sedimentary rocks for stable sulphir isotopic determination: Chemical Geology, v. 67, p. 35-45.

Hardie, L.A., 1987, Perspectives: Dolomitization-A critical view of some current views: Journal of Sedimentary Petrology, v. 57, p. 166-183.

Heinrich, C.A., Andrew, A.S., Wilkins, R.W.T., and Patterson, D.J., 1989, A fluid inclusion and stable isotope study of synmetamorphic copper ore formation at Mt Isa, Australia: Economic Geology, v. 84, p. 529-550.

Heydari, E., 1997, Hydrotectonic models of burial diagenesis in platform carbonates based on formation water geochemistry in North American sedimentary basins: *in* Montanez, I.P., Gregg, J.M., and Shelton, K.L., eds., Basin-wide Diagenetic Patterns, SEPM Special Publication No. 57, p. 53-80.

Hill, C.A., 1993, A hydrogen sulphide, basinal-degassing model for the origin of Mississippi Valley-Type ore deposits: in Shelton, K.L., and Hagni, R.D., eds., Proceedings Volume, Geology and Geochemistry of Mississippi Valley-Type Ore Deposits, p. 121-132.

Hinman, M., 1995, Structure and kinematics of the HYC-Cooley zone at McArthur River: Australian Geological Survey Organization Record 1995/5, 29p.

Hinman, M., 1996, Constraints, timing and processes of stratiform base metal mineralization at the HYC Ag-Pb-Zn deposit, McArthur River: MIC '96 Extended Conference Abstracts, Economic Geology Research Unit Contribution 55, James Cook University, p. 56-59.

Hinman, M., 1998, Speculation on syn-diagenetic processes of sulphate reduction at the HYC Pb-Zn deposit, NT: Geological Society of Australia Abstracts, v. 49, p. 212.

Hobbs, B.E., 1987, Principles involved in mobilization and remobilization: Ore Geology Reviews, v. 2, p. 37-45.

Jackson, M.J., Scott, D. L., and Rawlings, D., 1998. Correlations of Proterozoic units across the Murphy Inlier. Geological Society of Australia Abstracts, No. 49, p. 218.

Jacob, H., 1989, Classification, structure, genesis and practical importance of natural solid oil bitumen ("migrabitumen"): International Journal of Coal Geology, v. 11, p. 65-79.

Johnstone, A.R., 1994, Mineralogical, geochemical and stable isotope study of the metadolerite dykes and enclosing metasedimentary rocks in the South West Lakes Area, Lake Moondarra, Mount Isa: Unpublished Hons Thesis, James Cook University, Townsville, Queensland, Australia.

Jones, P., 1996, Notes on faults located in the IJ69 North Drive, George Fisher. Unpublished MIM Ltd Report, 11 p.

Justo, A., Maqueda, C., Perez-Rodriguez, J.L., and Lagaly, G., 1987, An unusually expandable low-charge vermiculite: Clay Minerals, v. 22, p. 319-327.

Kesler, S.E., Jones, H.D., Furman, F.C., Sassen, R., Anderson, W.H., and Kyle, J.R., 1994, Role of crude oil in the genesis of Mississippi Valley-type deposits: Evidence from the Cincinnati arch: Geology, v. 22, p. 609-612.

Komarneni, S., and Roy, R., 1981, Hydrothermal transformations in candidate overpack materials and their effects on cesium and strontium sorption: Nuclear Technology, v. 54, p. 118-122.

Lagache, M., 1993, Na-Ba and K-Ba partitioning between feldspar and aqueous chloride solutions. Some consequences of unmixing in solids and fluids: European Journal of Mineralogy, v. 5, p. 447-454.

Lambert, I.B., 1983, The major stratiform lead-zinc deposits of the Proterozoic: Geological Society of America, Memoir 161, p. 209-226.

Large, R.R., Bull, S.W., Cooke, D.R., and McGoldrick, P. J., 1998, A genetic model for the HYC deposit, Australia: Based on regional sedimentology, geochemistry and sulphide-sediment relationships: Economic Geology, v.93, p. 1345-1368.

Large, R., and McGoldrick, P.M., 1998, Lithogeochemical halos and geochemical vectors to stratiform sediment hosted Zn-Pb-Ag deposits, 1. Lady Loretta Deposit, Queensland: Journal of Geochemical Exploration, v. 63 , p. 37-56.

Lee, M.R., and Harwood, G.M., 1989, Dolomite calcitization and cement zonation related to uplift of the Raisby Formation (Zechstein carbonate), northeast England: Sedimentary Geology, v. 65, p. 285-305.

Legge, P.J., and Lambert, I.B., 1994, Australian sediment-hosted zinc-lead-silver deposits: recent developments and ideas, *in* Fontboté, L., and Boni, M., eds., Sediment-hosted Zn-Pb Ores: Berlin, Springer-Verlag, p. 299-332.

Leventhal, J.S., 1990, Organic matter and thermochemical sulphate reduction in the Viburnam Trend, Southeast Missouri: Economic Geology, v. 85, p. 622-632.

Lovering, T.S., 1961, Sulphide ores formed from sulphide-deficient solutions: Economic Geology, v. 56, p. 68-99.

MacCready, T., Goleby, B.R., Goncharov, A., Drummond, B.J., and Lister, G.S., 1998, A framework of overprinting orogens based on interpretation of the Mount Isa Deep Seismic Transect: Economic Geology, v. 8, p. 1422-1434.

McClay, K.R., and Carlile, D.G., 1978, Mid-Proterozoic sulphate evaporites at Mount Isa Mine, Queensland, Australia: Nature, v. 274, p. 240-241.

McClay, K.R., 1979, Folding in silver-lead-zinc orebodies, Mount Isa, Australia: Transactions of the Institution of Mining and Metallurgy, Section B: Applied Earth Science, v. 88, p. 5-14.

McClay, K.R., 1982, Tectonic and sedimentary structures in sulphide ore bodies of Mount Isa, Australia, and Sullivan, Canada: Transactions of the Institution of Mining and Metallurgy, Section B: Applied Earth Science, v. 91, p. 146-151.

McCrea, J.M., 1950, On the isotopic chemistry of carbonates and a palaeo-temperature scale: Journal of Chemical Physics, v. 18, p. 849-857.

McDonald, G.D., Collerson, K.D., and Kinny, P.D., 1997, Late Archean and Early Proterozoic crustal evolution of the Mount Isa block, northwest Queensland, Australia: Geology, v. 25, p. 1095-1098.

McGoldrick, P.J., and Keays, R.R., 1990, Mount Isa copper and lead-zinc-silver ores: coincidence or cogenesis?: Economic Geology, v. 85, p. 641-650.

Machel, H.G., 1987, Some aspects of sulphate-hydrocarbon redox reactions: *in* Marshall, J.D., ed., Diagenesis of Sedimentary Sequences, Geological Society Special Publication No. 36, p. 15-28.

Machel, H.G., Cavell, P.A., and Patey, K.S., 1996, Isotopic evidence for carbonate cementation and recrystallization, and for tectonic expulsion of fluids into the Western Canada Sedimentary Basin: Geological Society of America Bulletin, v. 108: 1108-1119.

Malone, M.J., Baker, P.A., and Burns, S.J., 1996, Hydrothermal dolomitization and recrystallization of dolomite breccias from the Miocene Monterey Formation, Tepusquet area, California: Journal of Sedimentary Research, v. 66, p. 976-990.

Marshall, B., and Gilligan L. B., 1987, An introduction to remobilization: Information from orebody geometry and experimental considerations: Ore Geology Reviews, v. 2, p. 87-131.

Marshall, B., and Gilligan L. B., 1989, Durchbewegung structure, piercement cusps, and piercement veins in massive sulphide deposits: formation and interpretation: Economic Geology, v. 84, p. 2311-2319.

Mathias, B.V., and Clark, G.J., 1975, Mt Isa copper and silver-lead-zinc orebodies- Isa and Hilton Mines: *in* C.L. Knight ed., Economic Geology of Australia and Papua New Guinea. Vol. I: Metals, Australian Institute Mining Metallurgy, p. 351-372.

Montañez, I.P., 1994, Late diagenetic dolomitization of Lower Ordivician, Upper Knox Carbonates: A record of the hydrodynamic evolution of the Southern Appalachian Basin: The American Association of Petroleum Geologists Bulletin, v. 78, p. 1210-1239.

Moore, C.H., 1989. Carbonate diagenesis and porosity. Developments in Sedimentology no. 46: Elsevier, Amsterdam, Netherlands, 338p.

Morse, J.W., and Mackensie, J.W., 1990, Geochemistry of Sedimentary Carbonates: Developments in Sedimentology no. 48: Elsevier, Amsterdam, Netherlands, 338p.

Mountjoy, E., Whittaker, S., Williams-Jones, A., Qing, H., Drivet, E., and Marquez, X., 1997, Variable fluid flow and heat flow regimes in three Devonian dolomite conduit systems, Western Canada Sedimentary Basin: Isotopic and fluid inclusion evidence/constraints: *in* Montanez, I.P., Gregg, J.M., and Shelton, K.L., eds., Basin-wide Diagenetic Patterns, SEPM Special Publication No. 57, p. 119-138.

Mullens, P.J., 1990, Geology and resource potential of Hilton North, January, 1990. Unpublished MIM Ltd Technical Report, No. Geo 137, 57 p.

Mullens, P.J., 1993, The exploration history and surface geochemistry of Hilton and Hilton North. Unpublished report submitted as partial fulfillment of MSc., Townsville, James Cook University, 19p.

Myers, R., Ceremuga, C., Clark, D., McSkimming, D., Price, S., Tuesley, M., and Wilkinson, D., 1996, Mount Isa lead-zinc mineralization: What controversy?: MIC '96 Extended Conference Abstracts, Economic Geology Research Unit Contribution 55, James Cook University, p. 85-89.

Neudert, M.K., 1983, A depositional model for the Upper Mt Isa Group and implications for ore formation: Unpublished PhD Thesis, The Australian National University, Canberra, 324p.

Neudert, M.K., 1986, Sedimentological constraints on the timing of Mount Isa Pb-Zn ore genesis: Sediments Down-Under, 12th International Sedimentological Congress Abstracts, p. 229.

Neudert, M.K., and Russell, R.E., 1981, Shallow water and hypersaline features from the Middle Proterozoic Mount Isa Sequence: Nature, v. 293, p. 284-286.

O'Dea, M.G., Lister, G.S., MacCready, T., Betts, P.G., Oliver, N.H.S., Pound, K.S., Huang, W., and Valenta, R.K., 1997, Geodynamic evolution of the Proterozoic Mount Isa terrain: *in* Burg, J.P., and Ford, M., eds., Orogeny Through Time, Geological Society Special Publication No. 121, p. 99-122.

Ohmoto, H., 1986, Stable isotope geochemistry of ore deposits: *in* Valley, J.W., Taylor, H.P., and O'Neil, J.R., eds., Stable Isotopes in High Temperature Geological

Processes, Reviews in Mineralogy, Mineralogical Society of America, no. 16, p. 491-560.

Oliver, N.H.S., Hoering, T.C., Johnson, T.W., Rumble III, D., and Shanks III, W.C., 1992, Sulphur isotopic disequilibrium and fluid-rock interaction during metamorphism of sulphidic black shales from the Waterville-Augusta area, Maine, USA: Geochimica et Cosmochimica Acta, v. 56, p. 4257-4265.

Page, R.W., and Bell, T.H., 1986, Isotopic and structural responses of granite to successive deformation and metamorphism. Journal of Geology, v. 94, p. 365-379.

Page, R.W., Sun, Shen-su, and Carr, G., 1994, Proterozoic sediment-hosted lead-zinc-silver deposits in Northern Australia - U-Pb zircon and Pb isotope studies. Geological Society of Australia Abstracts, No. 37, p. 334-335.

Page, R.W., and Sun, Shen-Su, 1998, Aspects of geochronology and crustal evolution in the Eastern Fold Belt, Mt Isa Inlier: Australian Journal of Earth Sciences, v. 45, p. 343-362.

Page, R.W., and Sweet, I.P., 1998, Geochronology of basin phases in the western Mount Isa Inlier, and correlation with the McArthur Basin: Australian Journal of Earth Sciences, v. 45, p. 219-232.

Painter, M.G.M., and Neudert, M.K., 1994, Sedimentary facies and stratigraphic correlations in the host to the Mount Isa Pb-Zn and Cu orebodies, the Urquhart Shale: *in* Australian Research on Ore Genesis Symposium Proceedings, Australian Mineral Foundation, December 12-14, 1994. Adelaide, S.A.

Painter, M.G.M., Hannan, K.W., and Golding, S.D., 1996, Sulphur isotopic constraints on the formation of "fine-grained pyrite" at Mount Isa and its relationship to base metal mineralization: MIC '96 Extended Conference Abstracts, Economic Geology Research Unit Contribution 55, James Cook University, p. 99-103.

Painter, M.G.M., Golding, S.D., Hannan, K.W., and Neudert, M.K., 1999, Sedimentological, petrographic and sulfur isotopic constraints on fine-grained pyrite formation at Mount Isa mine and environs, northwest Queensland, Australia : Economic Geology, v.94: *in press*.

Parnell, J., Monson, B., and Geng, A., 1996, Maturity and petrography of bitumens in the Carboniferous of Ireland: International Journal of Coal Geology, v. 29, p. 23-38.

Perkins, C., Heinrich, C.A., and Wyborn, L.A.I., 1999, $^{40}Ar/^{39}Ar$ Geochronology of copper mineralization and regional alteration, Mount Isa, Australia: Economic Geology, v. 94, p. 23-36.

Perkins, W.G., 1984, Mt Isa silica dolomite and copper ore bodies: The result a of syntectonic hydrothermal alteration system: ECONOMIC GEOLOGY, v. 79, p. 601-637.

Perkins, W.G., 1990, Mount Isa Copper Orebodies: *in* Hughes, F.E., ed., Geology of the Mineral Deposits of Australia and Papua New Guinea: Australasian Institute of Mining and Metallurgy, Monograph 14, p. 935-941.

Perkins, W.G., 1997, Mount Isa lead-zinc orebodies: Replacement lodes in a zoned syndeformational copper-lead-zinc system?: Ore Geology Reviews, v. 12, p. 61-110.

Perkins, W.G., 1998, Timing of formation of Proterozoic stratiform fine-grained pyrite: Post-diagenetic cleavage replacement at Mount Isa? Economic Geology, v. 93, p. 1153-1164.

Perkins, W.G., and Bell, T.H., 1998, Stratiform replacement lead-zinc deposits: A comparison between Mount Isa, Hilton and McArthur River: Economic Geology, v. 93, p. 1190-1212.

Plumb K.A., Ahmad, M., and Wygralak, A.S., 1990, Mid-Proterozoic basins of the North Australian Craton: Regional geology and mineralization: Australian Institute of Mining and Metallurgy Monograph 14, p. 881-902.

Pottorf, R.J., and Barnes, H.L., 1983, Mineralogy, geochemistry and ore genesis of hydrothermal sediments from the Atlantis II Deep, Red Sea: Economic Geology Monograph 5, p. 198-223.

Purser, B.H., Brown, A., and Aissaous, D.M., 1994, Nature, origins and evolution of porosity in dolomites: *in* Purser, B., Tucker, M., and Zenger, D., eds., Dolomites - A Volume in Honour of Dolomieu, International Association of Sedimentologists Special Publication No. 21, p. 283-308.

Ranititsch, G., 1995, Coalification and graphitization of graptolites in the anchizone and lower epizone: International Journal of Coal Geology, v. 27, p. 1-22.

Robert, P., 1988, Organic Metamorphism and Geothermal History: Microscopic Study of Organic Matter and Thermal Evolution of Sedimentary Basins. Reidel Publishing Co., Dordrecht, Holland, 311p.

Rosenbaum, J., and Sheppard, S.M.F., 1986, An isotopic study of siderites, dolomites and ankerites at high temperatures: Geochimica et Cosmochimica Acta, v. 50, p. 1147-1150.

Roy, R., and Romo, L.A., 1957, Weathering studies. 1. New data on vermiculite: Journal of Geology, v. 65, p. 603-610.

Rubenach, M.J., 1992, Proterozoic low-pressure/high-temperature metamorphism and an anticlockwise P-T-t path for the Hazeldene area, Mount Isa Inlier, Queensland, Australia: Journal of Metamorphic Geology, v. 10, p. 333-346.

Russell, M.J., Solomon, M., and Walshe, J.L., 1981, The genesis of sediment-hosted, exhalative zinc + lead deposits: Mineralium Deposita, v. 16, p. 113-127.

Saxby, J.D., 1981, Organic matter in ancient ores and sediments: Australian Bureau of Mineral Resources Journal of Geology and Geophysics, v. 6, p. 287-291.

Saxby, J.D., and Stephens, J.F., 1973, Carbonaceous matter in sulphide ores from Mount Isa and McArthur River: An investigation using the electronprobe and the electron microscope: Mineralium Deposita, v. 8, p. 127-137.

Selley, R.C., 1985, Elements of Petroleum Geology: W.H. Freeman and Co., New York, 449p.

Sharma, T., and Clayton, R.N., 1965, Measurement of $^{18}O/^{16}O$ ratios of total oxygen of carbonates: Geochimica et Cosmochimica Acta, v. 29, p. 1347-1353.

Sibley, D.F., and Gregg, J.M., 1987, Classification of dolomite rock textures. Journal of Sedimentary Petrology: v. 57, p. 967-975.

Simo, J.A., Johnson, M.R., Vandrey, M.R., Brown, P.E., Castrogiovanni, E., Drzewiecki, P.E., Valley, J.W., and Boyer, J., 1994, Burial dolomitization of the Middle

Ordovician Glenwood Formation by evaporitic brines, Michigan Basin: *in* Purser, B., Tucker, M., and Zenger, D., eds., Dolomites - A Volume in Honour of Dolomieu, International Association of Sedimentologists Special Publication No. 21, p. 169-186.

Singer, A., and Stoffers, P., 1981, Hydrothermal vermiculites from the Atlantis II Deep, Red Sea: Clays and Clay Minerals, v. 29, p. 454-458.

Smith, J.W., Burns, M.S., and Croxford, N.J.W., 1978, Stable isotope studies of the origins of mineralization at Mt Isa - I: Mineralium Deposita, v. 13, p. 369-381.

Solomon, P.J., 1965, Investigations into sulphide mineralization at Mount Isa, Queensland: Economic Geology , v. 60, p. 737-765.

Solomon, M., and Groves, D.I., 1994, The Geology and Origin of Australia's Mineral Deposits: Oxford Science Publications, Clarendon Press, Oxford Monographs on Geology and Geophysics, no. 24, 951p.

Spear, F.S., 1993, Metamorphic Phase Equilibria and pressure-Temperature-Time Paths: Mineralogical Society of America Monograph, Book Crafters, Inc., Michigan, 799p.

Stanton, R.L., 1963, Constitutional features of the Mount Isa sulphide ores and their interpretation: Institute of Mining and Metallurgy Transactions, v. 72, p. 131-144.

Sun, S., Page, R., and Carr, G., 1994, Lead-isotope-based stratigraphic correlations and ages of Proterozoic sediment-hosted Pb-Zn deposits in the Mount Isa Inlier: Australian Geological Survey Organization Research Newsletter, No. 20, p. 1-2.

Surdam, R.C., Crossey, L.J., Hagen, E.S., and Heasler, H.P., 1989, Organic-inorganic interactions and sandstone diagenesis: American Association of Petroleum Geologists Bulletin, v. 73, p. 1-23.

Sverjensky, D.A., 1981, The origin of a Mississippi Valley-type deposit in the Viburnum Trend, southeast Missouri: Economic Geology, v. 76, p. 1848-1872.

Sverjensky, D.A., 1984, Oil field brines as ore-forming solutions: Economic Geology, v. 79, p. 23-37.

Swager, C.P., 1985, Syndeformational carbonate-replacement model for the copper mineralization at Mt Isa, northwest Queensland: A microstructural study: Economic Geology, v. 80, p. 107-125.

Swager, C.P., Perkins, W.G., and Knights, J. G., 1987, Stratabound phyllosilicate zones associated with syntectonic copper orebodies at Mount Isa, Queensland: Australian Journal of Earth Sciences, v. 34, p. 463-476.

Theirault, F., and Hutcheon, I., 1987, Dolomitization and calcitization of the Devonian Grosmont Formation, northern Alberta: Journal of Sedimentary Petrology, v. 57, p. 955-966.

Tompkins, L.A., Rayner, M.J., and Groves, D.I., 1994, Evaporites: In situ sulphur source for rhythmically banded ores in the Cadjebut Mississippi Valley-Type Zn-Pb Deposit, Western Australia: Economic Geology, v. 89, p. 467-492.

Tracy, R.J. and Frost, B.R., 1991, Phase equilibria and thermobarometry of calcareous, ultramafic and mafic rocks, and iron formations: *in* Kerrick, D.M., ed., Contact Metamorphism, Reviews in Mineralogy, v. 26, p. 207-289.

Tuesley, M., 1993, The analysis of metal zonation patterns in the context of gangue mineral assemblages, Hilton Mine, Mount Isa: Unpublished Honours Thesis, James Cook University, Townsville, Australia, 170p.

Valenta, R.K., 1988, Deformation, fluid flow and mineralization in the Hilton area, Mt Isa, Australia: Unpublished PhD Thesis, Monash University, Melbourne, 269p.

Valenta, R., 1994, Deformation of host rocks and stratiform mineralization in the Hilton area, Mt Isa: Australian Journal of Earth Science, v. 41, p. 429-443.

Van den Heuvel, H.B., 1969, Sedimentation, stratigraphy and post-depositional changes in the sediments of the Upper Formations of the Mt Isa Group, NW Queensland: Unpublished PhD Thesis, University of Queensland, Brisbane.

Waring, C.L., 1990a, Genesis of the Mount Isa Cu ore system: Unpublished PhD Thesis, Monash University, Clayton, Victoria, 295p.

Waring, C.L., 1990b, The distinction between metamorphosed stratiform Pb-Zn-Ag mineralization and metamorphic syntectonic Cu mineralization at Mt Isa: Mt Isa Inlier

Geology Conference Abstracts, Monash University and the Victorian Institute of Earth and Planetary Sciences, p. 81-82.

Waring, C.L., Heinrich, C.A., and Wall, V.J., 1998, Proterozoic metamorphic Cu (Mt Isa Cu): Australian Geological Survey Organization Journal of Australian Geology and Geophysics, v. 17, p. 239-246.

Wilkinson, D., 1995, Structural termination of the 8 orebody and its implications for the genesis of the lead-zinc-silver mineralization, Mount Isa, Queensland: Unpublished Honours Thesis, James Cook University, Townsville, Queensland, 184p.

Williams, P.J., 1998, An introduction to the metallogeny of the McArthur-Mount Isa-Cloncurry Minerals Province: Economic Geology, v. 93, p. 1120-1131.

Winsor, C.N., 1986, Intermittent folding and faulting in the Lake Moondarra area, Mount Isa, Queensland: Australian Journal of Earth Sciences, v. 33, p. 27-42.

Winter, B.L., Clark, M.J., Simo, J.A., and Valley, J.W., 1995, Palaeozoic fluid history of the Michigan Basin: Evidence from dolomite geochemistry in the Middle Ordovician St. Peter Sandstone: Journal of Sedimentary Research, v. A65, p. 306-320.

Zierenberg, R.A., and Shanks III, W.C., 1983, Mineralogy and geochemistry of epigenetic features in metalliferous sediment, Atlantis II Deep, Red Sea: Economic Geology, v. 78, p. 57-72.

APPENDIX I - SAMPLE CATALOGUE

JCU Cat. #	LHC HS#	DDH #	Depth	Sample Type	Strat. Zone	PTS#	XRD	C/O	Pb	S
44685	OO8	J702 WI#2	9.3	fillet	I	20i, 20ii	*	*		
44686	O12	J702 WI#2	14.95	fillet	I	21i, 21ii, 21iii,	*	*		
44687	O18	J702 WI#2	24.5	fillet	I	12				
44688	O19	J702 WI#2	26.1	fillet	I	16, 17				
44689	O20	J702 WI#2	27.45	fillet	I	22i, 22ii	*	*		
44690	O22	J702 WI#2	33.7	fillet	I	23i	*	*		
44691	O23	J702 WI#2	35.1	fillet	I	24i, 24ii	*	*		
44692	O24	J702 WI#2	38	fillet	I					
44693	O25	J702 WI#2	42.27	fillet	I	9, 10, 11				
44694	O29	J702 WI#2	48.5	fillet	I	99				
44695	O31	J702 WI#2	52.6	fillet	I	84				
44696	O32	J702 WI#2	53.82	fillet	I	25ii	*			
44697	O33	J702 WI#2	55.4	fillet	I	4,5, 6				
44698	O34	J702 WI#2	57.9	fillet	I	1				
44699	O42	J702 WI#2	80.8	fillet	H fw	92, 93, 94				
44700	O44	J702 WI#5	45	fillet	I	26ii, 103, 104	*	*		
44701	O47	J702 WI#5	73.9	fillet	H fw					
44702	O48	J702 WI#5	75.3	fillet	H fw	2, 3				
44703	O50	J702 WI#5	105.9	fillet	G	13, 14, 15, 96				
44704	O51	J702 WI#5	111.65	fillet	G	18, 19				
44705	O52	J702 WI#5	113.8	fillet	G	7, 8, 53				
44706	O6O	J702 WI#5	183.4	fillet	D	107				
44707	O63	J702 WI#5	199.8	fillet	D?	122, 123				
44708	O78	J710 WI#1	71.1	1/ 2 core	I	27ii, 27iii, 54, 101, 102	*			
44709	O79	J710 WI#1	74	1/ 2 core	I	28	*			
44710	O81	J710 WI#1	106		H hw	63i, 63ii, 64, 65				
44711	O83	J710 WI#1	307.5	1/ 2 core	O2O1	36	*	*		
44712	O85	J710 WI#1	333.4	1/ 2 core	O2O1	90, 91				
44713	O86	J710 WI#1	42.6	fillet	I	57i, 57ii, 58, 59, 60, 129				
44714	O87	J710 WI#1	79.5	fillet	H fw	55, 56i, 56ii				
44715	O88	J710 WI#1	89.6	fillet	H fw					
44716	O90	J710 WI#1	197.8	fillet	F?	76, 77, 78				
44717	100	J702 WD#4	11.6	1/ 2 core	I	30i, 30ii	*	*		
44718	101	J702 WD#4	14.2	1/ 2 core	I	42	*	*		
44719	102	J702 WD#4	20.3	1/ 2 core	I	38	*			
44720	107	J702 WD#4	90.4	1/ 2 core	I	31	*			
44721	110	J702 WD#4	104.2	1/ 2 core	I	127, 128				
44722	117	J702 WD#4	141.1	1/ 2 core	H fw	161				
44723	118	J702 WD#4	168.4	1/ 2 core	H fw	49	*	*		
44724	122	J702 WD#4	179.1	1/ 2 core	H fw	50	*	*		
44725	123	J702 WD#4	183.5	1/ 2 core	H fw	79				*
44726	125	J702 WI#6	54.9	1/ 2 core	I	39i, 39ii	*	*		
44727	126	J702 WI#6	57.2	1/ 2 core	I	35i, 35ii, 35iii	*			
44728	127	J702 WI#6	57.8	1/ 2 core	I	40i, 40ii, 40iii	*	*		
44729	129	J702 WI#6	75.7	1/ 2 core	H fw	132				
44730	130	J702 WI#6	77.6	1/ 2 core	H fw		*			
44731	131	J702 WI#6	79.6	1/ 2 core	H fw	97, 98				
44732	132	J702 WI#6	80.7	1/ 2 core	H fw	41i, 41ii, 41iii	*	*		
44733	134	J702 WI#6	87.7	1/ 2 core	H fw	134				
44734	136	J702 WI#6	90.2	1/2 core	H fw	62				
44735	137	J702 WI#6	199.6	1/ 2 core	F	46, 80, 81	*	*		
44736	138	J702 WI#6	215.5	1/ 2 core	E	33	*	*		
44737	143	J702 WI#6	234.7	1/ 2 core	D	109, 110				*
44738	144	J702 WI#6	235	1/ 2 core	D	108				*
44739	150	J702 WI#6	244.5	1/ 2 core	D	119				

JCU Cat. #	LHC HS#	DDH #	Depth	Sample Type	Strat. Zone	PTS#	XRD	C/O	Pb	S
44740	152	J702 WI#6	250.7	1/ 2 core	D					
44741	154	J702 WI#6	252.8	1/ 2 core	D	45	*			
44742	157	J718 WD#5	291.1	1/ 2 core	F-1	34i, 34ii	*			
44743	158	J718 WD#5	292.5	1/ 2 core	F-1	48	*	*		
44744	159	J718 WD#5	294.1	1/ 2 core	F-1	47	*	*		
44745	166	J718 WD#5	336.2	1/ 2 core	F-3					
44746	169	J718 WD#5	345.7	1/ 2 core	D	117, 118				
44747	173	J718 WD#5	351.9	1/ 2 core	D	71, 124, 125, 126			*	
44748	181	J718 WI#3	175.4	fillet	D					
44749	186	J718 WI#3	192.2	fillet	C C/D	44i, 44ii, 44iii	*			
44750	190	J718 WI#3	205.4	1/4 core	C	82				
44751	191	J718 WI#3	207.3	1/4 core	C	69				
44752	201	J718 WI#3	237.8	1/4 core	B	83				
44753	202	J718 WI#3	248.1	1/2 core	B	43i, 43ii, 43iii	*	*		
44754	207	J718 WI#3	259.1	1/4 core	B	68				
44755	208	J718 WI#3	262.3	1/2 core	B	106				
44756	213	J718 WD#5	384.8	1/4 core	C	70				
44757	226	J718 WD#5	425.8	1/2 core	A	32	*	*		
44758	245	J718 WI#5	149.6	fillet	E	73, 74, 75				
44759	246	J718 WI#5	155.9	1/2 core	D	66				
44760	248	J718 WI#5	158.4	fillet	D					
44761	251	J718 WI#5	164.9	fillet	D	67i, 67ii, 67iii				
44762	253	J718 WI#5	166.9	fillet	D	105				
44763	254	J718 WI#5	167.3	fillet	D	111, 112, 113				
44764	255	J718 WI#5	171.7	fillet	D	87, 88, 89				
44765	256	J718 WI#5	174	fillet	D	121				
44766	260	J718 WI#5	202.9	fillet	C	85, 86				
44767	262	J718 WI#5	233.3	fillet	B	72				
44768	266	J718 WI#5	244.9	fillet	B	114				
44769	267	J718 WI#5	248.2	fillet	B	115, 116				
44770	268	J718 WI#5	248.9	fillet	B					
44771	270	J718 WI#5	64	1/2 core	I	61				
44772	272	I698 WI#3A	78.9	fillet	H hw	37i, 37ii			*	*
44773	276	K766 WI#2	241.2	fillet	B					
44774	278	K782 WI#1	93.7	fillet	H	169, 170, 171				
44775	279	K782 WI#1	117.2	fillet	H?	159, 166				
44776	281	K782 WI#1	125.3	fillet	H?	178				
44777	282	K782 WI#1	127.3	fillet	H?					
44778	288	K782 WI#1	178.5	fillet	F -3	167, 168				
44779	289	K782 WI#1	235	fillet	C				*	
44780	290	K774 WI#1	184.8	fillet	F-1	165				
44781	292	K774 WI#1	222.9	fillet	D	174, 175, 176, 177			*	
44782	294	J718 WI#4	118.3	fillet	F-2	163, 164				
44783	295	J718 WI#4	119.3	fillet	F-2	151, 152				
44784	296	J718 WI#4	MCBS	fillet	D				*	
44785	297	J718 WI#4	188	1/2 core	C	153				
44786	298	J718 WI#4	200.8	fillet	C	154				
44787	299	J718 WI#4	209.8	fillet	C	155				
44788	300	J718 WI#4	211	fillet	C	156				
44789	301	J718 WI#4	236.2	fillet	B	157, 158				
44790	303	J730 WI#1	37	fillet	H fw	162				
44791	305	J730 WI#1	189.8	fillet	D	179				*
44792	310	J722 WI#2	199.8	fillet	C	160				
44793	311	J722 WI#2	227.9	fillet	B	172				
44794	UG1	7200x-cut	-	-	C	136, 137, 138, 139			*	
44795	UG2	7200x-cut	-	-	C	140				

JCU Cat. #	LHC HS#	DDH #	Depth	Sample Type	Strat. Zone	PTS#	XRD	C/O	Pb	S
44796	UG3	7200x-cut	-	-	C					
44797	UG4	7200x-cut	-	-	C					
44798	UG5	7200x-cut	-	-	C					
44799	UG6	7200x-cut	-	-	C					
44800	UG7	7200x-cut	-	-	C					
44801	UG8	7200x-cut	-	-	C	141, 142			*	
44802	UG9	7200x-cut	-	-	C	143, 144				*
44803	UG10	7200x-cut	-	-	C					
44804	UG11	7200x-cut	-	-	C					
44805	UG12	7200x-cut	-	-	C					
44806	UG13	7200x-cut	-	-	C					
44807	UG14	7200x-cut	-	-	C	145				
44808	UG15	7200x-cut	-	-	C	146, 147, 148, 149			*	
44809	UG16	7200x-cut	-	-	F2	150				
44810	UG23	7200x-cut	-	-	C	180				*
44811	UG25	7200x-cut	-	-	D	134, 135			*	
44812	UG26	7200x-cut	-	-	D				*	
44813	UG29	7200x-cut	-	-	D				*	
44814	DC838	H766 ED#1	561	1/2 core	C	131				
44815	DC839	H766 ED#1	564	1/2 core	C	133	*	*		
44816	DC840a	H766 ED#1	558	1/2 core	C	130				
44817	DC840b	H766 ED#1	558.6	1/2 core	C	51	*	*		
44818	DC845	H766 ED#1	554	1/2 core	C	52	*	*		
44819	MP A	Qz 010	1044.4	1/2 core	-	A				
44820	MP B	Qz 010	1056.5	1/2 core	-	B				
44821	MP C	Zw 295	822.2	1/2 core	-	C				
44822	MP D	Zw 295	824.1	1/2 core	-	D				
44823	MP E	M 815	1122.7	1/2 core	-	E				

APPENDIX II
LIST OF GRAPHICALLY LOGGED DIAMOND DRILLHOLES

- J702 WI#2 1:200 Field Graphic Log
- J702 WI#2 1:100 Summary Log, I-H stratigraphic intervals (true thickness represented)
- J702 WI#2 1:100 Summary Log, F-B stratigraphic intervals (true thickness represented)

- J710 WI#1 1:200 Field Graphic Log
- J710 WI#1 1:100 Summary Log, I-H stratigraphic intervals (true thickness represented)
- J710 WI#1 1:100 Summary Log, F-B stratigraphic intervals (true thickness represented)

- J702 WI#2 1:100 Field Graphic Log
- J702 WI#2 1:100 Summary Log, I-H stratigraphic intervals (true thickness represented)
- J702 WI#2 1:100 Summary Log, F-B stratigraphic intervals (true thickness represented)

- J718 WI#4 1:200 Field Graphic Log
- J718 WI#4 1:100 Summary Log, I-H stratigraphic intervals (true thickness represented)
- J718 WI#4 1:100 Summary Log, F-B stratigraphic intervals (true thickness represented)
- J718 WI#4 1:100 Summary Log, Mineralization styles for the F-B stratigraphic intervals (apparent thickness represented)

- J722 WI#2 1:200 Field Graphic Log
- J722 WI#2 1:500 Summary Log, F-B stratigraphic intervals (apparent thickness represented)

- J730 WI#1 1:200 Field Graphic Log
- J730 WI#1 1:500 Summary Log, I-H stratigraphic intervals (apparent thickness represented)
- J730 WI#1 1:500 Summary Log, F-B stratigraphic intervals (apparent thickness represented)

- K766 WI#2 1:200 Field Graphic Log
- K766 WI#2 1:500 Summary Log, I-H stratigraphic intervals (apparent thickness represented)
- K766 WI#2 1:500 Summary Log, F-B stratigraphic intervals (apparent thickness represented)

- K774 WI#1 1:200 Field Graphic Log
- K774 WI#1 1:500 Summary Log, I-H stratigraphic intervals (apparent thickness represented)
- K774 WI#1 1:500 Summary Log, F-B stratigraphic intervals (apparent thickness represented)

- K782 WI#1 1:200 Field Graphic Log
- K782 WI#1 1:500 Summary Log, I-H stratigraphic intervals (apparent thickness represented)
- K782 WI#1 1:500 Summary Log, F-B stratigraphic intervals (apparent thickness represented)

APPENDIX IIIa - X-RAY DIFFRACTION -BASED WHOLE ROCK MINERAL ABUNDANCES

JCU#	LHC #	Rock Type or Vein Type	Dol %	Cal %	Qtz %	Mica %	Chl %	Kfs %	Alb %	Py %	Po %	Gal %	Gpt %
44685	0008	SBS	57	1	29	6	1	3	2	1			
44685	0008	BM	56		30	8		3	3				
44686	0012a	BM	26		61	10		2	1				
44686	0012a	WB		90	10								
44689	0020g	WB	2	87	11								
44690	0022b	MM	57		41	2							
44691	0023b	Nod		94	4					2			
44691	0023b	WB		95	5								
44696	0032	Syntectonic fibre vein		67	32					1			
44700	0044b	MM	7	48	45								
44700	0044b	BM	26		57	7		9	1				
44708	0078b	Syntectonic fibre vein		90	10								
44709	0079c	MM	2	87	11								
44730	130	Nod	11	71	13					5			
44717	100	Nod	3	88	4					5			
44717	100	MM	60		35	3		2	mnr				
44720	107	WB	5	82	12								1
44720	107	BM	58	6	32	2		1					1
44757	226a	Stage IXa carbonate vein infill	100										
44757	226b	BM	32		60	6		1	1				
44736	138b	Stage V sugary ferroan dolomite vein infill	88		12								
44742	157	Stage IXa carbonate vein infill	19	79						2			
44727	126b	Syntectonic fibre vein		55	41					3		1	
44711	0083i	BM	37		56	4		2	1				
44772	272b	Stage IXa carbonate vein infill	100										
44719	102	SM	78	3	12	4	1	1					1
44726	125	WB	3	62	33	1		1					
44728	127	WB		93	7								
44728	127	SBS	36		51	8		4	1				
44732	132	MM		80	20								
44718	101	MM	48	10	38	2	1	1					
44753	202b	BM	22		78								
44749	186	Stage IXa carbonate vein infill		99						1		1	
44741	154	Stage IXa carbonate vein infill	98							1			
44735	137a	Stage V sugary ferroan dolomite vein infill	94		3					3			
44744	159	Stage V sugary ferroan dolomite vein infill	94		4					1		1	
44743	158	Stage V sugary ferroan dolomite vein infill	90		8					2			
44723	118	Nod	63	5	20		1	1		9	1		
44724	122	Nod	85	3	3					7	2		
44818	36845	BM	43		7	6		2	1				1
44817	36840	Nod	7	78	11			1		3			
44815	36839	Nod	2	85	5					8			
44815	36839	PS	23	8	21			4		43			1
44815	36839	Nod		95	2					3			
44817	36840	WB	1	90	7	1		1					
44817	36840	BM	48		41	7		2	1	1			
44818	36845	WB	4	74	19			1		2			
44818	36845	Nod	29	34	24	1	1	2		8	1		
44817	36840	Nod	15	61	16	1		1		6			
44817	36840	WB		85	13					2			
44817	36840	BM	53		38	5		2	1	1			
44817	36840	PS	33	2	26	2		6		30			1
44817	36840	PS	44		28	3		4		18			2

APPENDIX IIIb

MIXED LAYER TRIOCTAHEDRAL MICA-VERMICULITE

A mineral phase, with the general formula K_2 $(MgFe)_{5.5}$ Si_{6-7} Al_{1-2} and analysis totals between 84 and 91 wt%, was identified on the microprobe (Appendix IV). Cation content and low totals can most reasonably be explained if the the phase is a mixed layer vermiculite-mica.

Examination of X-ray powder patterns confirms the presence of trioctahedral vermiculite which shows varying degrees of hydration ($4H_2O$ - $2H_2O$) illustrated by its variable (001) spacing from 12.7 - 13.6Å. Trioctahedral mica also exhibits a variable basal spacing of 10.5 to 10.7 Å. From evidence of repeats, the true basal repeat of the interstratified phase is probably 46.5 - 48.5 Å and in each repeat there are approximately 50% mica and 50% vermiculite layers relatively regularly interstratified. However, it is not clear whether it is a MVMV or MMVV stacking pattern.

From positions of reflectance in region 19-21 2σ it is strongly suggested that there is little or no dioctahedral component since no (020) reflections are present in the typical range of 19.7 - 20.00 2σ. The majority of reflections identified as (020) are in the range 19.05 - 19.40 2σ (Avg. = 19.22 2σ or 4.618 Å).

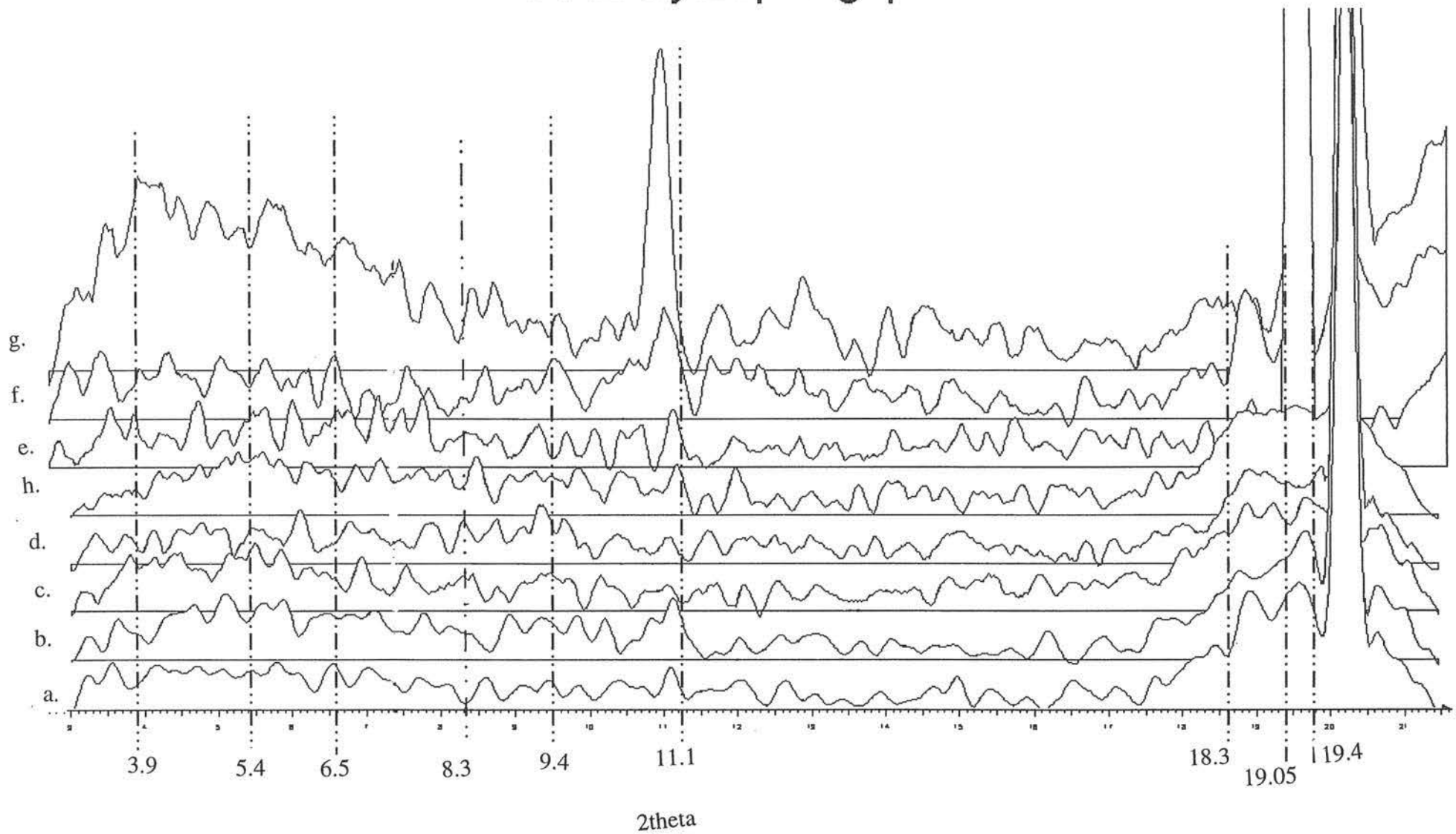
XRD hydrophlogopite
g.
f.
e.
h.
d.
c.
b.
a.
3.9
5.4
6.5
8.3
9.4
11.1
18.3
19.05
19.4
2theta

APPENDIX IV
MICROPROBE RESULTS

CONTENTS

Stage OI core and inner rim carbonates

	14core1d	14rim1e	14core1f	8rim1h	8rim1i	8rim1r
FeO	0.770	5.780	2.620	10.300	8.650	9.200
MnO	0.080	1.410	0.250	1.520	1.410	1.690
MgO	21.500	17.100	19.200	14.100	15.400	15.200
CaO	29.800	28.800	29.700	28.600	29.300	28.600
TOTAL	52.240	53.100	51.860	54.700	54.910	54.790
wt% C02 equ.	47.393	45.833	46.059	45.249	46.127	45.899
NUMBER OF IONS ON THE BASIS OF 2 OXYGENS						
Fe +2	0.020	0.155	0.070	0.281	0.230	0.246
Mn	0.002	0.038	0.007	0.041	0.038	0.046
Mg	0.991	0.817	0.911	0.683	0.732	0.726
Ca	0.987	0.990	1.012	0.995	1.000	0.982

	8rim2c	8core2i	8rim2j	8rim2k	8rim2s	39core1f
FeO	8.600	1.210	3.510	10.100	8.980	6.890
MnO	1.530	0.280	0.700	1.910	2.070	0.460
MgO	15.400	18.000	15.530	12.800	12.400	15.700
CaO	29.400	33.700	43.400	28.500	29.000	29.700
TOTAL	55.020	53.290	53.170	53.480	52.480	52.800
wt% C02 equ.	46.262	47.046	42.754	43.910	43.295	45.005
NUMBER OF IONS ON THE BASIS OF 2 OXYGENS						
Fe +2	0.228	0.031	0.020	0.284	0.255	0.188
Mn	0.041	0.008	0.018	0.054	0.059	0.012
Mg	0.729	0.835	0.631	0.641	0.628	0.761
Ca	1.002	1.124	1.268	1.021	1.058	1.038

	39core1h	39rim1i	39rim1j	39core1k	39rim2f	39rim2l
FeO	7.560	1.280	6.730	1.870	6.710	5.910
MnO	0.780	0.270	0.640	0.280	0.170	0.260
MgO	15.700	20.000	16.800	20.000	17.100	17.700
CaO	29.900	32.200	29.800	31.600	29.100	29.300
TOTAL	53.950	53.840	53.960	53.780	53.130	53.260
wt% C02 equ.	45.803	48.088	46.316	47.986	45.743	46.130
NUMBER OF IONS ON THE BASIS OF 2 OXYGENS						
Fe +2	0.202	0.032	0.178	0.048	0.179	0.157
Mn	0.021	0.007	0.017	0.007	0.004	0.007
Mg	0.750	0.909	0.794	0.910	0.818	0.839
Ca	1.027	1.052	1.011	1.035	0.998	0.998

	131core1a	131core1g	131core2b	131rim2l	131core3a
FeO	0.280	0.250	0.240	7.090	0.440
MnO	0.220	0.260	0.150	0.720	0.010
MgO	20.900	20.100	20.300	16.700	21.100
CaO	30.900	31.400	31.000	29.000	31.500
TOTAL	52.360	52.070	51.760	53.670	53.090
wt% C02 equ.	47.402	46.931	46.750	45.858	48.038
NUMBER OF IONS ON THE BASIS OF 2 OXYGENS					
Fe +2	0.007	0.006	0.006	0.189	0.011
Mn	0.006	0.007	0.004	0.019	0.000
Mg	0.962	0.935	0.095	0.798	0.958
Ca	1.025	1.052	1.039	0.994	1.030

Stage OI core and inner rim carbonates continued.

	131core3b	131core3f
FeO	0.410	0.390
MnO	0.080	0.270
MgO	21.400	18.700
CaO	30.900	33.700
TOTAL	52.810	53.220
wt% C02 equ.	47.927	47.301
	NUMBER OF IONS ON THE BASIS OF 2 OXYGENS	
Fe +2	0.010	0.010
Mn	0.002	0.007
Mg	0.975	0.865
Ca	1.013	1.118

Stage OI light grey matrix carbonates

	14lc1i	14lc2k	835lc1b	835lc1d	835lc2a	835lc2c
FeO	7.100	7.510	12.100	11.700	11.500	12.300
MnO	1.480	1.320	2.530	2.460	2.170	2.400
MgO	15.100	15.900	12.500	12.500	12.600	12.700
CaO	28.600	28.900	27.300	27.500	27.400	27.600
TOTAL	52.360	53.680	54.490	54.370	53.750	55.110
wt% C02 equ.	44.352	45.596	44.313	44.175	43.874	44.796
	NUMBER OF IONS ON THE BASIS OF 2 OXYGENS					
Fe +2	0.196	0.202	0.337	0.327	0.324	0.338
Mn	0.041	0.036	0.071	0.069	0.061	0.067
Mg	0.747	0.764	0.619	0.622	0.630	0.621
Ca	1.015	0.998	0.972	0.982	0.985	0.974

	835lc3b	8lc1e	8lc1f	8lc2h	8lc3c	8lc3d
FeO	13.100	9.880	9.160	9.230	9.190	7.080
MnO	2.040	1.660	1.520	1.560	1.620	1.470
MgO	12.300	14.800	15.000	14.300	14.000	15.200
CaO	27.200	28.500	27.600	28.900	29.400	30.000
TOTAL	54.810	54.960	53.380	54.030	54.270	53.840
wt% C02 equ.	44.275	45.778	44.748	45.076	45.160	45.540
	NUMBER OF IONS ON THE BASIS OF 2 OXYGENS					
Fe +2	0.365	0.265	0.251	0.251	0.250	0.191
Mn	0.057	0.045	0.042	0.043	0.044	0.040
Mg	0.611	0.710	0.736	0.695	0.682	0.730
Ca	0.967	0.981	0.971	1.011	1.024	1.039

	8lc3f	8lc3g	8lc3j	8lc3m	39lc1m	39lc2p
FeO	9.360	9.580	7.490	8.420	6.200	5.200
MnO	1.760	1.580	1.340	1.300	0.630	0.310
MgO	14.100	13.000	14.400	13.900	17.100	18.400
CaO	28.700	28.800	29.000	29.300	29.300	30.100
TOTAL	53.940	53.080	52.290	53.030	53.310	54.030
wt% C02 equ.	44.925	43.807	44.039	44.269	45.920	47.123
	NUMBER OF IONS ON THE BASIS OF 2 OXYGENS					
Fe +2	0.256	0.268	0.209	0.233	0.165	0.135
Mn	0.049	0.045	0.038	0.036	0.017	0.008
Mg	0.689	0.652	0.717	0.688	0.814	0.852
Ca	1.006	1.035	1.037	1.043	1.004	1.005

	39lc2q	39lc3r	131lc1f	131lc1h	131lc1i	131lc2i
FeO	7.060	6.680	7.270	6.080	7.740	7.620
MnO	0.390	0.520	0.670	0.880	1.020	0.960
MgO	16.200	16.200	15.100	17.000	15.500	15.900
CaO	29.600	28.700	29.700	29.300	28.800	29.600
TOTAL	53.330	52.240	52.770	53.350	53.100	54.160
wt% C02 equ.	45.526	44.681	44.734	45.917	45.005	45.953
	NUMBER OF IONS ON THE BASIS OF 2 OXYGENS					
Fe +2	0.190	0.183	0.199	0.162	0.211	0.203
Mn	0.010	0.014	0.019	0.024	0.028	0.026
Mg	0.777	0.794	0.740	0.812	0.753	0.757
Ca	1.023	1.009	1.043	1.002	1.008	1.014

Stage OI light grey matrix continued.

	131lc3c	131lc3d	131lc3g	103lc1c	103lc1f	103lc1g
FeO	6.920	6.980	7.650	7.400	6.640	5.950
MnO	0.640	0.720	1.130	0.340	0.250	0.350
MgO	16.100	17.100	15.300	15.700	16.300	17.200
CaO	29.900	29.700	29.100	28.500	29.000	29.100
TOTAL	53.680	54.560	53.340	52.000	52.280	52.690
wt% C02 equ.	45.747	46.776	45.046	44.289	44.806	45.516
NUMBER OF IONS ON THE BASIS OF 2 OXYGENS						
Fe +2	0.185	0.183	0.208	0.205	0.181	0.160
Mn	0.017	0.019	0.031	0.010	0.007	0.009
Mg	0.770	0.799	0.745	0.773	0.796	0.828
Ca	1.028	0.999	1.016	1.013	1.016	1.003

Stage OI grey matrix

	14lc1`j	14lc1k	14lc2h	14lc2i	835lc1	835lc1c
FeO	4.780	3.600	3.850	3.470	8.350	7.710
MnO	1.390	1.330	1.690	1.480	1.740	1.430
MgO	17.800	18.300	18.400	18.600	16.000	16.000
CaO	29.100	29.200	29.700	30.300	28.400	27.800
TOTAL	53.190	52.560	53.750	53.890	54.610	52.960
wt% C02 equ.	46.206	46.064	46.979	47.284	46.131	45.044
NUMBER OF IONS ON THE BASIS OF 2 OXYGENS						
Fe +2	0.127	0.096	0.101	0.090	0.222	0.210
Mn	0.037	0.036	0.045	0.039	0.047	0.039
Mg	0.845	0.871	0.858	0.861	0.760	0.779
Ca	0.991	0.998	0.997	1.010	0.971	0.972

	835lc2b	835lc2d	835lc3a	8lc1b	8lc1c	8lc1d
FeO	7.740	8.530	8.700	4.550	6.860	4.760
MnO	1.690	1.490	1.580	1.300	0.810	1.290
MgO	15.800	15.200	15.300	18.600	16.700	18.900
CaO	28.200	28.200	27.900	29.200	28.100	29.300
TOTAL	53.490	53.430	53.590	53.680	52.540	54.330
wt% C02 equ.	45.346	45.030	45.073	46.952	45.075	47.480
NUMBER OF IONS ON THE BASIS OF 2 OXYGENS						
Fe +2	0.210	0.233	0.237	0.119	0.187	0.123
Mn	0.046	0.041	0.044	0.034	0.022	0.034
Mg	0.766	0.740	0.746	0.868	0.810	0.872
Ca	0.978	0.987	0.974	0.979	0.981	0.971

	8lc2n	8lc2s	8lc2o	8lc3h	8lc3i
FeO	4.790	4.350	6.970	4.630	4.510
MnO	1.250	1.360	1.140	1.440	1.080
MgO	16.500	18.800	15.000	17.400	17.400
CaO	30.600	29.500	29.300	30.500	29.600
TOTAL	53.220	54.060	52.540	54.010	52.650
wt% C02 equ.	45.869	47.327	44.466	46.812	45.772
NUMBER OF IONS ON THE BASIS OF 2 OXYGENS					
Fe +2	0.128	0.113	0.192	0.121	0.121
Mn	0.034	0.036	0.032	0.038	0.029
Mg	0.790	0.872	0.739	0.815	0.832
Ca	1.048	0.980	1.037	1.025	1.018

Stage OI grey matrix continued.

	8Ic3j	8Ic3k	8Ic2m	39Ic1r	39Ic2o	39Ic3s
FeO	4.500	4.660	3.070	3.380	3.600	3.960
MnO	1.210	1.260	1.250	0.410	0.440	0.250
MgO	17.000	16.900	17.100	19.400	18.900	18.600
CaO	29.700	30.000	30.600	29.700	30.100	29.300
TOTAL	52.560	52.970	52.130	52.990	53.080	52.260
wt% C02 equ.	45.502	45.762	45.470	46.859	46.783	45.911
	NUMBER OF IONS ON THE BASIS OF 2 OXYGENS					
Fe +2	0.121	0.125	0.083	0.088	0.094	0.105
Mn	0.033	0.034	0.034	0.011	0.012	0.007
Mg	0.819	0.810	0.825	0.906	0.882	0.886
Ca	1.027	1.032	1.059	0.995	1.012	1.002

	39Ic2u	39Ic2v	131Ic1c	131Ic1e	131Ic2e	131Ic2f
FeO	4.140	3.300	6.280	4.820	4.830	4.610
MnO	0.580	0.190	0.350	0.570	0.490	0.250
MgO	18.100	19.300	16.900	17.800	17.800	18.000
CaO	30.000	30.100	29.600	29.300	29.700	29.600
TOTAL	52.920	52.960	53.180	52.640	52.870	52.590
wt% C02 equ.	46.263	46.855	45.783	45.795	46.058	45.889
	NUMBER OF IONS ON THE BASIS OF 2 OXYGENS					
Fe +2	0.110	0.086	0.168	0.129	0.128	0.123
Mn	0.016	0.005	0.009	0.015	0.013	0.007
Mg	0.855	0.900	0.806	0.851	0.846	0.858
Ca	1.020	1.009	1.017	1.005	1.012	1.013

	131Ic2h1	131Ic2h2	131Ic2n	131Ic3e	131Ic3h	103Ic1d
FeO	4.840	4.580	4.380	5.080	4.730	3.440
MnO	0.540	0.600	0.520	0.280	0.980	0.370
MgO	17.000	18.400	17.900	18.900	18.000	19.000
CaO	29.500	30.000	29.700	30.300	29.700	29.300
TOTAL	52.040	53.600	52.620	54.700	53.480	52.100
wt% C02 equ.	45.069	46.874	45.913	47.731	46.569	46.116
	NUMBER OF IONS ON THE BASIS OF 2 OXYGENS					
Fe +2	0.131	0.120	0.117	0.130	0.125	0.091
Mn	0.015	0.016	0.014	0.007	0.026	0.010
Mg	0.826	0.859	0.854	0.866	0.845	0.900
Ca	1.028	1.006	1.016	0.997	1.004	0.998

	1031h	130Ic1b	130Ic1c
FeO	3.830	3.400	4.290
MnO	0.160	0.890	0.910
MgO	19.400	18.600	18.700
CaO	29.700	30.100	29.400
TOTAL	53.200	53.040	53.390
wt% C02 equ.	46.954	46.658	46.777
	NUMBER OF IONS ON THE BASIS OF 2 OXYGENS		
Fe +2	0.100	0.089	0.112
Mn	0.004	0.024	0.024
Mg	0.904	0.872	0.876
Ca	0.992	1.015	0.988

Stage OI ferroan carbonates in Stage III Ba-Kfs altered mudstones

	Cal1111a	Core1111c	Core1111f	Core1112a	Grey1111e
FeO	1.120	0.680	1.440	0.460	5.930
MnO	0.490	0.260	0.680	0.470	2.010
MgO	0.880	21.000	21.000	20.200	16.600
CaO	53.400	29.800	28.400	31.100	28.300
TOTAL	55.930	51.850	51.490	52.360	52.970
wt % CO2 equ.	43.910	46.92	46.59	47.09	45.420
	NUMBER OF IONS ON THE BASIS OF (2) OXYGENS				
Fe++	0.03	0.02	0.04	0.01	0.16
Mn++	0.01	0.01	0.02	0.01	0.06
Mg++	0.04	0.98	0.99	0.94	0.80
Ca 2+	1.91	1.00	0.96	1.04	0.98

	Grey1111i	Grey 1111j	Ic105b	Ic1055c	Ic67ii3f
FeO	3.840	4.890	0.26	0.79	14.10
MnO	1.940	1.080	0.61	0.14	0.76
MgO	18.100	18.000	20.30	18.20	17.50
CaO	28.400	29.400	31.30	33.10	22.60
TOTAL	52.270	53.480	52.60	52.28	55.11
wt % CO2 equ.	45.810	46.500	47.33	46.44	46.03
	NUMBER OF IONS ON THE BASIS OF (2) OXYGENS				
Fe++	0.10	0.13	0.01	0.02	0.38
Mn++	0.05	0.03	0.02	0.00	0.02
Mg++	0.87	0.85	0.94	0.86	0.83
Ca 2+	0.98	1.00	1.04	1.12	0.77

	Ic67ii3b	Ic105d	Ic1055e	Ic105g	Ic1052c
FeO	10.80	0.04	10.70	5.21	7.37
MnO	0.00	0.03	1.89	1.60	1.74
MgO	17.20	19.70	14.30	17.00	14.40
CaO	26.90	32.10	28.30	29.60	29.80
TOTAL	55.02	51.94	55.33	53.57	53.42
wt% CO2 equ.	46.51	46.74	45.74	46.14	44.88
	NUMBER OF I(	NUMBER OF IONS ON THE BASIS OF 2 OXYGENS			
Fe2+	0.29	0.00	0.29	0.14	0.20
Mn	0.00	0.00	0.05	0.04	0.05
Mg	0.81	0.92	0.69	0.81	0.70
Ca	0.91	1.08	0.97	1.01	1.05

Stage I mudstone-hosted calcite alteration and Stage OI relict early dolomite

	8Cal (a)	8Cal(b)	101RD(a)	101RD(b)	101RD(c)	101RD1j
FeO	1.560	0.840	2.900	3.350	3.160	6.380
MnO	0.800	0.540	0.470	0.440	0.570	0.580
MgO	0.930	0.620	18.900	19.600	19.600	17.800
CaO	53.700	54.800	30.800	30.500	30.300	29.800
TOTAL	56.970	56.810	53.120	54.010	53.690	54.730
wt% C02 equ.	44.692	44.588	46.925	47.708	47.529	47.150
	NUMBER OF IONS ON THE BASIS OF 2 OXYGENS					
Fe +2	0.043	0.023	0.076	0.086	0.081	0.165
Mn	0.022	0.015	0.012	0.011	0.015	0.015
Mg	0.045	0.030	0.881	0.899	0.901	0.826
Ca	1.890	1.932	1.031	1.003	1.003	0.993

	101RD(d)	101lc1h	101RD2a	101RD2b	101RD1i	103Cal1k
FeO	5.180	3.320	0.000	3.510	3.150	0.650
MnO	0.810	0.600	0.000	0.650	0.610	0.490
MgO	18.200	18.900	21.600	19.700	19.100	0.600
CaO	30.100	30.800	31.300	29.800	29.600	55.100
TOTAL	54.350	53.710	53.000	53.690	52.610	56.850
wt% C02 equ.	47.254	47.276	48.150	47.518	46.456	44.649
	NUMBER OF IONS ON THE BASIS OF 2 OXYGENS					
Fe +2	0.134	0.086	0.000	0.091	0.083	0.018
Mn	0.021	0.016	0.000	0.017	0.016	0.013
Mg	0.841	0.876	0.980	0.906	0.899	0.029
Ca	1.003	1.022	1.020	0.987	1.002	1.940

	18cbl1	18cbl4	18cbl5	18cbl7	18cbl8	18cbl9
FeO	0.650	0.630	0.500	0.860	1.060	1.040
MnO	1.010	0.850	0.710	1.350	0.820	0.860
MgO	0.630	0.690	0.860	0.760	0.600	0.580
CaO	54.300	54.400	54.100	52.500	54.000	53.900
TOTAL	56.620	56.580	56.150	55.500	56.530	56.370
wt% C02 equ.	44.430	44.450	44.220	43.530	44.280	44.190
	NUMBER OF IONS ON THE BASIS OF 2 OXYGENS					
Fe +2	0.018	0.017	0.014	0.024	0.029	0.029
Mn	0.028	0.024	0.020	0.038	0.023	0.024
Mg	0.031	0.034	0.042	0.038	0.029	0.029
Ca	1.924	1.924	1.924	1.900	1.918	1.919

	18cbl10	18cbl11	18cbl12	101RD1k	18 rel dol 3
FeO	1.000	0.860	0.940	5.280	7.970
MnO	0.900	0.660	1.250	0.420	2.010
MgO	0.570	0.570	0.810	18.400	15.200
CaO	53.600	54.400	53.400	29.800	28.700
TOTAL	56.090	56.550	56.470	53.950	53.940
wt% C02 equ.	43.950	44.320	44.270	47.016	45.450
	NUMBER OF IONS ON THE BASIS OF 2 OXYGENS				
Fe +2	0.028	0.024	0.026	0.137	0.216
Mn	0.025	0.018	0.035	0.011	0.055
Mg	0.028	0.028	0.040	0.855	0.734
Ca	1.919	1.930	1.899	0.996	0.995

Stage I nodular calcite

	14lath2d	52lc2e	52lc2f	52lc2g	52lc2h	130lc3c
FeO	0.340	0.690	0.590	0.830	0.400	0.670
MnO	0.440	0.820	0.260	0.370	0.540	0.760
MgO	0.170	0.650	0.580	0.690	0.370	0.660
CaO	53.100	52.400	51.600	52.600	52.000	55.000
TOTAL	54.120	54.580	53.080	54.540	53.310	57.100
wt% C02 equ.	42.384	42.848	41.678	42.809	41.848	44.843
NUMBER OF IONS ON THE BASIS OF 2 OXYGENS						
Fe +2	0.010	0.020	0.017	0.024	0.012	0.018
Mn	0.013	0.024	0.008	0.010	0.016	0.021
Mg	0.008	0.033	0.030	0.035	0.019	0.032
Ca	1.969	1.924	1.945	1.931	1.954	1.929

	52nc3	52nc4	52nc5	52nc9
FeO	0.390	0.940	0.550	0.600
MnO	0.900	0.720	0.930	0.680
MgO	0.700	0.700	0.470	0.420
CaO	55.000	54.600	54.200	55.200
TOTAL	56.990	56.950	56.190	56.950
wt% C02 equ.	44.820	44.710	44.060	44.640
NUMBER OF IONS ON THE BASIS OF 2 OXYGENS				
Fe +2	0.011	0.026	0.015	0.016
Mn	0.025	0.020	0.026	0.019
Mg	0.034	0.034	0.023	0.020
Ca	1.931	1.921	1.936	1.945

Stage I layer-parallel white band calcite

	52wb(a)	52wb(b)	52wb(c)	52wb(d)	52wb2	17wb10
FeO	0.370	0.420	0.150	0.570	0.450	0.620
MnO	0.560	0.490	0.450	0.580	0.630	0.980
MgO	0.620	0.070	0.480	0.670	0.690	0.680
CaO	53.900	53.900	54.200	51.700	55.300	54.700
TOTAL	55.440	53.510	55.260	53.510	57.100	57.030
wt% C02 equ.	43.608	42.988	43.477	42.073	44.880	44.760
NUMBER OF IONS ON THE BASIS OF 2 OXYGENS						
Fe +2	0.010	0.012	0.004	0.016	0.012	0.017
Mn	0.016	0.014	0.013	0.017	0.017	0.027
Mg	0.031	0.003	0.024	0.034	0.033	0.033
Ca	1.943	1.971	1.960	1.932	1.936	1.923

	17wb4	17wb6	17wb9
FeO	0.830	0.380	0.380
MnO	0.590	0.380	0.670
MgO	0.730	0.700	0.780
CaO	53.300	55.200	54.200
TOTAL	55.420	56.750	56.110
wt% C02 equ.	43.560	44.590	44.100
NUMBER OF IONS ON THE BASIS OF 2 OXYGENS			
Fe +2	0.023	0.010	0.010
Mn	0.017	0.011	0.019
Mg	0.036	0.034	0.038
Ca	1.924	1.943	1.932

Carbonates distal to mineralization (samples provided by M. Painter)

	A3bckdol1	A3bckdol2	A3bckdol3	A3bckdol4	B1rim 1
FeO	2.690	2.590	2.820	3.090	3.640
MnO	0.160	0.190	0.330	0.250	0.910
MgO	20.400	30.000	20.200	19.900	19.100
CaO	29.800	20.900	29.800	30.200	29.800
TOTAL	53.060	53.830	53.160	53.460	53.490
wt% CO2 equ.	47.430	48.090	47.410	47.500	47.130
	NUMBER OF IONS ON BASIS OF 2 OXYGENS				
Fe+2	0.069	0.066	0.073	0.080	0.095
Mn	0.005	0.006	0.010	0.008	0.028
Mg	0.939	0.949	0.930	0.915	0.885
Ca	0.986	0.979	0.986	0.998	0.992

	B1core1	B1core2	B1 core3	C2bckdol1	C2bckdol2
FeO	0.860	0.780	0.670	4.090	5.750
MnO	0.240	0.360	0.430	0.380	0.420
MgO	21.200	20.900	20.700	19.300	17.800
CaO	30.500	30.200	30.200	29.200	29.500
TOTAL	52.800	52.340	52.060	53.070	53.540
wt% CO2 equ.	47.790	47.260	47.020	46.770	46.410
	NUMBER OF IONS ON BASIS OF 2 OXYGENS				
Fe+2	0.022	0.020	0.017	0.107	0.152
Mn	0.007	0.009	0.011	0.010	0.011
Mg	1.002	0.967	0.964	0.902	0.839
Ca	0.969	1.004	1.008	0.981	0.998

	C2bckdol3	C2bckdol4	C2bckdol5	C3core1	C3core2
FeO	3.370	4.190	5.000	0.650	0.590
MnO	0.470	0.390	0.450	0.590	0.310
MgO	19.400	18.700	18.600	21.200	21.000
CaO	29.300	29.900	29.900	30.300	30.400
TOTAL	52.610	53.270	54.070	52.830	52.410
wt% CO2 equ.	46.580	46.730	47.160	47.750	47.370
	NUMBER OF IONS ON BASIS OF 2 OXYGENS				
Fe+2	0.089	0.110	0.130	0.017	0.015
Mn	0.012	0.010	0.012	0.015	0.008
Mg	0.912	0.875	0.863	0.971	0.969
Ca	0.987	1.005	0.994	0.997	1.008

Carbonates distal to mineralization (samples provided by M. Painter) continued.

	C3rim1	C3rim2	A3cal	A3cal2	A1cal
FeO	4.350	4.960	0.850	0.530	0.090
MnO	0.220	0.320	0.100	0.010	0.140
MgO	19.600	19.000	0.970	0.410	0.860
CaO	29.100	29.900	55.700	57.200	56.500
TOTAL	53.340	54.250	57.650	58.170	57.640
wt% CO2 equ.	47.060	47.480	45.360	45.670	45.440
	NUMBER OF IONS ON BASIS OF 2 OXYGENS				
Fe+2	0.113	0.128	0.024	0.014	0.002
Mn	0.006	0.008	0.003	0.000	0.004
Mg	0.912	0.877	0.048	0.020	0.041
Ca	0.969	0.988	1.986	1.966	1.952

	A1cal2	A3cal3	A3cal4
FeO	0.310	0.320	0.520
MnO	0.100	0.220	0.440
MgO	1.220	0.670	0.700
CaO	55.300	56.100	55.400
TOTAL	57.010	57.310	57.120
wt% CO2 equ.	44.990	45.110	44.880
	NUMBER OF IONS ON BASIS OF 2 OXYGENS		
Fe+2	0.008	0.009	0.014
Mn	0.003	0.007	0.014
Mg	0.059	0.032	0.034
Ca	1.929	1.952	1.938

Stage III calcite-ferroan dolomite vein infill

	67iV1a	67iV1b	67iVic	67iVb2	67iVb3	67iVb4
FeO	0.190	0.590	0.130	0.420	0.000	0.250
MnO	1.060	0.830	1.060	0.860	1.110	1.280
MgO	0.800	0.690	0.940	1.050	0.700	0.680
CaO	57.520	56.560	56.260	56.670	54.360	56.090
TOTAL	59.580	58.660	58.390	59.000	56.170	58.310
wt% CO2 equ.	43.360	42.620	42.570	43.010	40.900	42.410
	NUMBER OF IONS ON BASIS OF (2) OXYGENS					
Fe 2+	0.005	0.015	0.004	0.011	0.000	0.007
Mn	0.028	0.026	0.029	0.027	0.031	0.035
Mg	0.037	0.032	0.044	0.049	0.035	0.033
Ca	1.929	1.926	1.923	1.912	1.934	1.926

	112Va3	112Va4	112Va5	112Va6	112Vb1	112Vb2
FeO	0.210	0.200	0.610	0.230	0.760	0.570
MnO	0.490	0.720	0.420	0.360	0.600	1.030
MgO	0.590	0.410	1.030	0.490	0.910	0.890
CaO	56.230	55.760	54.560	56.430	56.420	55.110
TOTAL	57.510	57.100	56.620	57.510	58.680	57.610
wt% CO2 equ.	41.770	41.410	41.230	41.710	42.680	41.930
	NUMBER OF IONS ON BASIS OF (2) OXYGENS					
Fe 2+	0.006	0.006	0.017	0.006	0.020	0.015
Mn	0.013	0.020	0.012	0.010	0.016	0.028
Mg	0.028	0.020	0.050	0.023	0.043	0.043
Ca	1.653	1.954	1.921	1.960	1.920	1.913

	112Vb5	112Vc1	112Vc2	112Vc3	123V1b	123V1c
FeO	0.970	0.200	0.570	0.350	0.160	0.170
MnO	1.040	0.920	0.900	0.640	0.560	0.250
MgO	0.670	0.550	0.860	0.680	0.800	0.950
CaO	54.960	56.630	55.990	57.250	55.190	56.910
TOTAL	57.640	58.300	58.320	58.920	56.710	58.280
wt% CO2 equ.	41.840	42.340	42.430	42.810	41.270	42.440
	NUMBER OF IONS ON BASIS OF (2) OXYGENS					
Fe 2+	0.026	0.005	0.015	0.009	0.004	0.004
Mn	0.029	0.025	0.025	0.017	0.016	0.007
Mg	0.032	0.026	0.030	0.032	0.039	0.045
Ca	1.913	1.943	1.919	1.941	1.941	1.944

Stage III calcite-ferroan dolomite vein infill continued.

	67iVb5	112Va2	112Vb3	112Vb4	123V1e	123V1f
FeO	2.560	0.600	0.900	0.650	0.360	0.210
MnO	2.060	0.480	0.580	0.970	0.000	0.770
MgO	18.880	0.580	0.800	0.360	0.560	0.740
CaO	30.710	56.330	56.430	55.440	56.720	56.250
TOTAL	54.220	57.980	58.720	57.430	57.640	57.970
wt% CO2 equ.	45.980	42.060	42.640	41.590	41.800	42.170
	NUMBER OF IONS ON BASIS OF (2) OXYGENS					
Fe 2+	0.066	0.016	0.010	0.017	0.010	0.006
Mn	0.054	0.013	0.016	1.938	0.000	0.021
Mg	0.867	0.028	0.038	0.018	0.027	0.035
Ca	1.014	1.942	1.922	0.027	1.963	1.938

	123V1g	123V2a	123V2b	123V4c	123V2d	123V2e
FeO	0.600	2.200	3.020	3.090	3.190	2.660
MnO	0.460	0.880	0.860	0.780	1.020	0.620
MgO	0.740	19.600	19.080	18.680	18.890	19.400
CaO	56.720	29.970	29.120	29.420	29.030	29.430
TOTAL	58.520	52.250	52.080	51.970	52.130	52.110
wt% CO2 equ.	42.500	45.090	44.390	44.150	44.350	44.550
	NUMBER OF IONS ON BASIS OF (2) OXYGENS					
Fe 2+	0.016	0.058	0.080	0.082	0.085	0.070
Mn	0.013	0.023	0.023	0.021	0.027	0.018
Mg	0.035	0.923	0.904	0.889	0.897	0.914
Ca	1.936	0.998	0.992	1.006	0.990	0.997

	123V4a	1234b
FeO	3.750	2.890
MnO	0.720	0.840
MgO	18.500	19.230
CaO	29.240	29.670
TOTAL	52.220	52.620
wt% CO2 equ.	44.180	44.850
	NUMBER OF IONS ON BASIS OF (2) OXYGENS	
Fe 2+	0.100	0.076
Mn	0.020	0.023
Mg	0.880	0.901
Ca	1.000	1.000

Stage V sugary ferroan dolomite vein infill

	lc100v2	lc100v3	lc100v4	lc100v5	lc100v6	lc100v7
FeO	7.550	7.810	7.090	6.000	6.060	5.640
MnO	1.250	1.220	0.900	1.170	0.780	0.910
MgO	16.500	15.800	17.200	16.400	16.900	16.900
CaO	29.100	29.000	29.400	29.100	29.200	29.200
TOTAL	54.480	53.910	54.620	52.740	52.980	52.710
wt% C02 equ.	46.380	45.680	46.850	45.270	45.650	45.480
	NUMBER OF IONS ON THE BASIS OF 2 OXYGENS					
Fe +2	0.199	0.209	0.185	0.162	0.163	0.152
Mn	0.039	0.039	0.028	0.037	0.025	0.029
Mg	0.777	0.755	0.802	0.791	0.809	0.811
Ca	0.985	0.997	0.985	1.009	1.004	1.008

	lc100v9	lc100v10	lc100v11	lc100v12	lc100v13	lc100v14
FeO	6.610	6.840	6.470	4.080	6.940	7.030
MnO	0.860	1.150	0.730	1.150	1.410	1.250
MgO	16.900	16.800	17.200	18.300	16.400	16.400
CaO	28.800	28.800	29.400	29.200	28.400	28.900
TOTAL	53.230	53.710	53.900	52.830	53.190	53.760
wt% C02 equ.	45.720	45.970	46.340	46.230	45.470	45.800
	NUMBER OF IONS ON THE BASIS OF 2 OXYGENS					
Fe +2	0.177	0.182	0.171	0.108	0.187	0.188
Mn	0.027	0.036	0.023	0.036	0.045	0.039
Mg	0.807	0.798	0.811	0.865	0.788	0.782
Ca	0.989	0.983	0.996	0.991	0.980	0.990

	lc47v1	lc47v3	lc47v4	lc47v5	lc47v6	lc47v7
FeO	6.480	6.070	6.550	6.470	6.580	5.960
MnO	0.780	0.900	0.980	0.740	0.890	0.750
MgO	17.500	17.800	17.500	16.800	16.700	17.100
CaO	28.700	29.000	28.900	29.100	29.000	29.400
TOTAL	53.580	53.850	54.000	53.210	53.260	53.260
wt% C02 equ.	46.170	46.560	46.510	45.700	45.670	45.940
	NUMBER OF IONS ON THE BASIS OF 2 OXYGENS					
Fe +2	0.172	0.160	0.173	0.174	0.177	0.159
Mn	0.244	0.028	0.030	0.023	0.028	0.024
Mg	0.828	0.835	0.822	0.803	0.799	0.813
Ca	0.976	0.978	0.975	1.000	0.997	1.005

	lc47v8	lc47v9
FeO	6.340	7.000
MnO	0.540	0.830
MgO	17.500	17.000
CaO	29.300	28.800
TOTAL	53.710	53.610
wt% C02 equ.	46.380	46.050
	NUMBER OF IONS ON THE BASIS OF 2 OXYGENS	
Fe +2	0.168	0.186
Mn	0.017	0.026
Mg	0.824	0.806
Ca	0.992	0.982

Stage V sugary ferroan dolomite veins - wall rock ferroan dolomite

	lc47wr1	lc47wr3	lc47wr4	lc47wr6
FeO	9.870	5.610	3.720	4.530
MnO	1.010	0.820	0.620	0.650
MgO	14.800	18.300	19.300	18.300
CaO	28.300	28.600	29.000	29.300
TOTAL	54.030	53.350	52.720	52.840
wt% C02 equ.	45.150	46.460	46.560	46.220

NUMBER OF IONS ON THE BASIS OF 2 OXYGENS

Fe +2	0.268	0.148	0.098	0.120
Mn	0.032	0.026	0.019	0.017
Mg	0.716	0.860	0.905	0.867
Ca	0.984	0.966	0.978	0.996

	lc47wr7	lc47wr8	lc47wr9	lc47wr10	lc47wr11
FeO	6.180	5.770	9.220	9.510	9.560
MnO	0.740	0.830	0.770	0.760	1.140
MgO	17.100	18.000	15.800	15.200	14.800
CaO	29.300	28.900	29.200	28.600	28.400
TOTAL	53.400	53.550	55.040	54.160	53.930
wt% C02 equ.	45.990	46.470	46.370	45.420	45.130

NUMBER OF IONS ON THE BASIS OF 2 OXYGENS

Fe +2	0.165	0.152	0.244	0.256	0.260
Mn	0.020	0.022	0.020	0.021	0.031
Mg	0.815	0.847	0.746	0.732	0.720
Ca	1.001	0.979	0.990	0.991	0.989

Stage VIII matrix ferroan carbonate

	lc431a	lc432a	lc432b	lc432c	lc432d	lc432i
FeO	2.780	6.840	6.930	5.820	5.140	5.370
MnO	0.510	1.850	1.500	2.430	2.120	1.630
MgO	18.700	15.700	16.000	16.300	17.500	17.400
CaO	30.200	28.800	29.000	29.800	29.900	29.200
TOTAL	52.240	53.220	53.450	54.460	54.710	53.650
wt% CO2 equ.	46.190	45.270	45.560	46.510	47.250	46.380
NUMBER OF IONS ON BASIS OF (2) OXYGENS						
Fe 2+	0.074	0.186	0.187	0.154	0.134	0.142
Mn	0.014	0.051	0.041	0.065	0.056	0.044
Mg	0.887	0.761	0.770	0.770	0.812	0.821
Ca	1.026	1.003	1.002	1.012	0.999	0.994

	lc432j	lc432k	lc432o	lc433a	lc433b	lc433f
FeO	5.010	6.130	7.520	6.520	5.620	4.650
MnO	1.960	1.930	1.620	1.920	1.610	1.970
MgO	17.600	17.100	15.200	15.900	17.700	17.300
CaO	29.400	29.200	29.200	29.000	29.200	29.000
TOTAL	54.040	54.420	53.660	53.400	54.230	52.950
wt% CO2 equ.	46.780	46.740	45.290	45.500	46.850	45.920
NUMBER OF IONS ON BASIS OF (2) OXYGENS						
Fe 2+	0.131	0.161	0.204	0.176	0.147	0.124
Mn	0.052	0.051	0.044	0.053	0.043	0.053
Mg	0.827	0.802	0.737	0.767	0.828	0.826
Ca	0.990	0.985	1.015	1.004	0.982	0.997

	lc434g	lc1212b	lc1212c	lc1212d	lc1212i
FeO	6.260	6.640	5.740	7.950	6.620
MnO	1.680	1.210	1.550	1.780	1.510
MgO	16.400	16.400	17.000	15.200	15.700
CaO	29.300	29.600	29.600	28.600	29.600
TOTAL	53.670	53.950	53.960	53.630	53.490
wt% CO2 equ.	45.950	46.080	46.430	45.200	45.520
NUMBER OF IONS ON BASIS OF (2) OXYGENS					
Fe 2+	0.167	0.176	0.152	0.216	0.179
Mn	0.045	0.032	0.041	0.049	0.041
Mg	0.783	0.779	0.803	0.738	0.756
Ca	1.004	1.012	1.004	0.998	1.024

	lc1212k	lc1212l
FeO	6.380	6.940
MnO	1.530	1.500
MgO	16.400	15.400
CaO	29.200	29.200
TOTAL	53.620	53.140
wt% CO2 equ.	45.840	45.070
NUMBER OF IONS ON BASIS OF (2) OXYGENS		
Fe 2+	0.170	0.189
Mn	0.041	0.041
Mg	0.785	0.750
Ca	1.003	1.020

Stage VIII matrix light Grey ferroan carbonate

	lc431h	lc431j	lc431l	lc431v	lc431w	lc432f
FeO	11.800	11.500	9.210	16.400	10.900	9.720
MnO	2.760	2.190	2.100	0.720	2.360	1.170
MgO	11.700	11.500	13.700	10.500	12.100	14.600
CaO	28.900	29.000	29.400	28.100	28.700	28.900
TOTAL	55.340	54.260	54.520	55.830	54.170	54.480
wt% CO2 equ.	44.680	43.940	45.190	44.080	44.120	45.420
NUMBER OF IONS ON BASIS OF (2) OXYGENS						
Fe 2+	0.327	0.322	0.250	0.458	0.306	0.262
Mn	0.077	0.062	0.058	0.020	0.066	0.032
Mg	0.577	0.574	0.665	0.522	0.602	0.704
Ca	1.019	1.042	1.026	1.000	1.025	1.001

	lc432g	**lc432p**	**lc432q**	**lc434c**	**lc434d**	**lc434e**
FeO	13.000	10.400	10.900	10.300	9.240	9.550
MnO	2.310	2.770	2.490	1.820	1.740	2.140
MgO	11.500	12.100	11.600	13.400	14.200	14.500
CaO	29.500	29.100	29.200	28.700	29.100	28.700
TOTAL	56.470	54.480	54.240	54.380	54.310	54.920
wt% CO2 equ.	45.340	44.420	44.060	44.780	45.260	45.750
NUMBER OF IONS ON BASIS OF (2) OXYGENS						
Fe 2+	0.354	0.289	0.305	0.283	0.251	0.257
Mn	0.063	0.078	0.070	0.050	0.048	0.058
Mg	0.556	0.598	0.579	0.658	0.687	0.697
Ca	1.027	1.035	1.046	1.009	1.014	0.989

	lc1212e	**lc1212f**	**lc1212g**	**lc1212h**
FeO	10.000	10.000	8.490	10.700
MnO	1.640	2.040	1.740	1.840
MgO	14.100	14.100	14.100	13.000
CaO	28.100	28.300	30.200	28.800
TOTAL	53.900	54.600	54.590	54.470
wt% CO2 equ.	44.760	45.210	45.550	44.680
NUMBER OF IONS ON BASIS OF (2) OXYGENS				
Fe 2+	0.275	0.229	0.290	0.295
Mn	0.045	0.047	0.050	0.051
Mg	0.691	0.681	0.680	0.639
Ca	0.989	1.043	1.040	1.015

Stage VIII nodular ferroan carbonate

	lc501b	lc501e	lc501f	lc501g	lc502b
FeO	3.570	4.820	4.770	5.090	4.030
MnO	2.170	2.110	1.830	1.860	1.630
MgO	18.200	17.100	16.700	16.900	17.100
CaO	30.000	29.600	29.800	29.300	29.300
TOTAL	53.990	53.740	53.210	53.260	52.090
wt% CO2 equ.	47.171	46.379	45.866	45.910	45.313
NUMBER OF IONS ON BASIS OF (2) OXYGENS					
Fe 2+	0.093	0.128	0.127	0.136	0.109
Mn	0.057	0.057	0.049	0.050	0.045
Mg	0.847	0.809	0.798	0.807	0.827
Ca	1.003	1.007	1.025	1.007	1.019

	lc501h	lc502a	lc502p	lc502q	lc502r	lc502c
FeO	5.660	3.360	14.900	14.400	14.000	4.700
MnO	2.060	2.220	1.620	1.520	1.730	2.150
MgO	16.700	17.300	9.910	10.200	9.940	17.500
CaO	29.200	29.600	30.000	30.600	30.000	30.400
TOTAL	53.670	52.570	56.450	56.800	55.670	54.790
wt% CO2 equ.	46.106	45.782	44.662	45.071	44.223	47.399
NUMBER OF IONS ON BASIS OF (2) OXYGENS						
Fe 2+	0.151	0.090	0.410	0.392	0.389	0.122
Mn	0.055	0.060	0.045	0.042	0.049	0.056
Mg	0.794	0.831	0.486	0.498	0.492	0.811
Ca	1.000	1.018	1.059	1.068	1.070	1.011

	lc502d	lc502e	lc502f	lc502g	lc502h	lc502i
FeO	12.800	12.300	13.800	13.500	12.700	14.500
MnO	1.580	1.150	1.730	1.110	1.180	0.970
MgO	10.600	10.400	9.900	10.800	11.000	10.000
CaO	30.400	30.700	30.700	29.800	29.700	29.600
TOTAL	55.580	54.730	56.240	55.350	54.700	55.210
wt% CO2 equ.	44.414	43.814	44.606	44.251	43.951	43.732
NUMBER OF IONS ON BASIS OF (2) OXYGENS						
Fe 2+	0.354	0.346	0.382	0.376	0.354	0.407
Mn	0.044	0.032	0.048	0.031	0.033	0.027
Mg	0.525	0.520	0.486	0.536	0.548	0.502
Ca	1.077	1.101	1.085	1.057	1.064	1.063

	lc502j	lc502k	lc502l	lc502m	lc502n	lc502o
FeO	12.900	13.400	12.700	12.900	15.200	14.200
MnO	1.760	1.390	1.560	1.250	1.630	1.420
MgO	10.600	10.300	10.500	10.700	9.880	10.100
CaO	30.100	30.400	30.600	30.000	29.100	30.100
TOTAL	55.540	55.590	55.500	55.040	55.930	55.840
wt% CO2 equ.	44.370	44.317	44.386	44.032	44.114	44.375
NUMBER OF IONS ON BASIS OF (2) OXYGENS						
Fe 2+	0.359	0.372	0.353	0.360	0.425	0.393
Mn	0.049	0.039	0.044	0.035	0.046	0.040
Mg	0.524	0.510	0.520	0.533	0.490	0.499
Ca	1.068	1.079	1.084	1.071	1.039	1.069

Stage VIII matrix ferroan carbonate
(Stage III Ba-K-feldspar altered host rock)

	lc712j	lc712l	lc713g	lc713h	lc713j	lc713k
FeO	12.400	12.800	12.400	13.000	12.500	12.600
MnO	2.120	1.630	1.670	2.050	2.350	2.020
MgO	12.400	12.200	13.200	12.200	12.700	12.200
CaO	27.200	27.400	26.600	27.400	26.900	27.400
TOTAL	54.190	54.250	53.950	54.750	54.440	54.320
wt% CO2 equ.	44.010	43.840	44.090	44.270	44.330	44.000
	NUMBER OF IONS ON THE BASIS OF 2 OXYGENS					
Fe2+	0.347	0.360	0.346	0.362	0.347	0.353
Mn	0.060	0.046	0.047	0.057	0.066	0.057
Mg	0.618	0.611	0.657	0.606	0.629	0.607
Ca	0.975	0.983	0.950	0.975	0.957	0.982

	lc713l	lc714c	lc714d	lc851n	lc851q	lc852c
FeO	13.600	15.100	12.600	11.100	15.800	9.010
MnO	2.430	2.190	1.830	2.520	2.240	2.190
MgO	12.100	11.100	12.200	13.100	10.100	15.000
CaO	28.100	26.600	27.400	27.300	26.800	27.600
TOTAL	56.350	55.190	54.160	54.190	55.060	53.790
wt% CO2 equ.	45.350	43.820	43.870	44.350	43.360	45.140
	NUMBER OF IONS ON THE BASIS OF 2 OXYGENS					
Fe2+	0.370	0.425	0.354	0.309	0.448	0.246
Mn	0.067	0.062	0.052	0.071	0.064	0.060
Mg	0.586	0.556	0.610	0.650	0.514	0.730
Ca	0.977	0.957	0.984	0.970	0.974	0.964

Stage VIII ferroan carbonate vein infill
(Stage III Ba-K-feldspar altered host rock)

	lc114va	lc114vb	lc114vc	lc114vd	lc114ve	lc114vf
FeO	18.10	17.70	18.10	18.50	20.90	16.90
MnO	1.76	0.91	1.41	1.79	1.71	1.67
MgO	7.43	9.08	8.04	7.60	7.15	9.28
CaO	28.50	27.90	28.30	27.90	27.40	28.40
TOTAL	55.87	55.64	55.94	55.86	57.24	56.37
wt% CO2 equ.	42.84	43.31	43.09	42.82	43.35	43.98
NUMBER OF IONS ON THE BASIS OF 2 OXYGENS						
Fe2+	0.52	0.50	0.52	0.53	0.59	0.47
Mn	0.05	0.03	0.04	0.05	0.05	0.05
Mg	0.38	0.46	0.41	0.39	0.36	0.46
Ca	1.05	1.01	1.04	1.03	1.00	1.02

	lc114vh	lc114vl	lc114vm	lc114vn	lc114vo	lc71v2	lc71v1
FeO	15.90	16.50	53.30	53.80	53.20	12.40	11.60
MnO	1.06	1.34	1.93	1.70	1.99	1.80	2.15
MgO	9.91	9.96	5.62	5.36	5.36	12.60	12.70
CaO	28.80	27.90	0.40	0.32	0.35	27.50	27.80
TOTAL	55.75	55.77	61.25	61.20	60.96	54.40	54.44
wt% CO2 equ.	43.93	43.85	40.49	40.28	40.15	44.24	44.34
NUMBER OF IONS ON THE BASIS OF 2 OXYGENS							
Fe2+	0.45	0.46	1.62	1.64	1.63	0.35	0.32
Mn	0.03	0.04	0.06	0.05	0.06	0.05	0.06
Mg	0.49	0.50	0.30	0.29	0.29	0.63	0.63
Ca	1.03	1.00	0.02	0.01	0.01	0.98	0.99

Stage VIII ferroan carbonate vein infill

	Vn1212n	Vn1212o	Vn1212p	Vn1212q	Vn1212s	Vn1212t
FeO	15.700	14.000	17.500	13.200	15.100	14.000
MnO	2.070	1.980	2.020	1.510	1.760	1.960
MgO	11.000	11.300	9.500	12.100	10.900	10.800
CaO	27.000	27.900	27.500	27.900	27.900	29.300
TOTAL	55.910	55.280	56.590	54.860	55.850	56.170
wt% CO2 equ.	44.310	44.240	44.130	44.280	44.320	44.780
NUMBER OF IONS ON BASIS OF (2) OXYGENS						
Fe 2+	0.436	0.389	0.489	0.367	0.419	0.385
Mn	0.058	0.055	0.057	0.042	0.049	0.054
Mg	0.545	0.562	0.471	0.598	0.541	0.528
Ca	0.961	0.993	0.983	0.993	0.991	1.032

HYDROPHLOGOPITE

	67iic1	67iic2	67iic3	67iic4	67iic5	67iic6	67iic7	67iic8
SiO2	43.18	41.39	41.35	38.99	40.37	41.00	41.71	41.31
TiO2	0.56	0.70	0.65	0.71	0.50	0.90	0.60	0.64
Al2O3	9.61	9.23	9.28	9.95	9.68	9.76	10.18	9.84
FeO	1.62	1.92	1.68	2.19	1.59	2.62	1.82	1.89
CaO	0.00	0.00	0.00	0.00	0.00	0.00	0.00	0.00
MgO	24.09	23.10	24.34	22.42	23.37	23.60	24.19	24.93
MnO	0.00	0.06	0.09	0.00	0.00	0.18	0.09	0.20
Na2O	0.00	0.00	0.00	0.00	0.00	0.00	0.00	0.00
K2O	10.35	10.47	10.22	9.81	9.97	9.88	10.64	10.45
Total	89.41	86.87	87.61	84.07	85.48	87.94	89.23	89.26

NUMBER OF IONS ON THE BASIS OF 22 OXYGENS

Si	6.42	6.37	6.30	6.21	6.29	6.25	6.25	6.20
Ti	0.06	0.08	0.07	0.09	0.06	0.10	0.07	0.07
Al	1.68	1.67	1.67	1.87	1.78	1.75	1.80	1.74
Fe2+	0.20	0.25	0.21	0.29	0.21	0.33	0.23	0.24
Ca	0.00	0.00	0.00	0.00	0.00	0.00	0.00	0.00
Mg	5.33	5.30	5.53	5.32	5.43	5.36	5.41	5.58
Mn	0.00	0.00	0.00	0.00	0.00	0.02	0.01	0.03
Na	0.00	0.00	0.00	0.00	0.00	0.00	0.00	0.00
K	1.96	2.06	1.99	1.99	1.98	1.92	2.03	2.00
Total	15.66	15.74	15.78	15.77	15.75	15.74	15.80	15.86

	67iic9	67iic10	67iic11	67iic12	67iic13	67iic14	hn39i
SiO2	40.56	41.69	41.65	40.76	44.24	44.05	41.20
TiO2	0.59	0.74	0.68	0.48	0.17	0.31	0.69
Al2O3	9.53	9.66	9.77	10.18	7.91	7.61	11.70
FeO	1.97	2.01	2.40	6.41	1.70	1.62	5.93
CaO	0.05	0.00	0.02	0.00	0.00	0.00	0.00
MgO	23.41	24.15	23.43	22.55	23.41	23.04	20.50
MnO	0.13	0.26	0.07	0.00	0.17	0.00	0.41
Na2O	0.00	0.00	0.00	0.00	0.00	0.00	0.00
K2O	10.40	10.27	10.36	9.10	10.23	9.98	11.10
Total	86.64	88.78	88.38	89.48	87.83	86.61	91.77

NUMBER OF IONS ON THE BASIS OF 22 OXYGENS

Si	6.28	6.28	6.31	6.33	6.68	6.73	6.16
Ti	0.07	0.08	0.08	0.06	0.02	0.04	0.08
Al	1.74	1.71	1.74	1.86	1.41	1.37	2.07
Fe2+	0.25	0.25	0.30	0.31	0.21	0.21	0.74
Ca	0.01	0.00	0.00	0.00	0.00	0.00	0.00
Mg	5.40	5.42	5.29	5.22	5.27	5.24	4.56
Mn	0.02	0.03	0.01	0.00	0.02	0.00	0.06
Na	0.00	0.00	0.00	0.00	0.00	0.00	0.00
K	2.05	2.00	2.00	1.80	1.97	1.94	2.13
Total	15.81	15.78	15.74	15.58	15.58	15.53	15.79

Celsian-hyalophane-K-feldspar

	67omd2	67core3	67core4	67core5	67core6	67core 7
SiO2	55.49	41.92	42.89	40.78	35.03	34.68
Al2O3	21.35	24.13	23.79	24.02	26.83	26.20
Na2O	0.59	0.00	0.65	0.63	0.00	0.00
K2O	10.44	3.96	4.56	3.67	0.54	0.77
CaO	0.00	0.00	0.00	0.00	0.00	0.00
BaO	13.65	29.00	27.13	29.18	37.28	36.77
TOTAL	101.52	99.01	99.02	98.28	99.68	98.42
NUMBER OF IONS ON THE BASIS OF 8 OXYGENS						
Si	2.75	2.39	2.42	2.36	2.11	2.12
Al	1.25	1.62	1.58	1.64	1.90	1.89
Na	0.06	0.00	0.07	0.07	0.00	0.00
K	0.66	0.29	0.33	0.27	0.04	0.05
Ca	0.00	0.00	0.00	0.00	0.00	0.00
Ba	0.26	0.65	0.60	0.66	0.88	0.88
TOTAL	4.98	4.95	5.00	5.00	4.93	4.94

	67core8	67omd9	67imd10	67omd11	67omd12
SiO2	33.54	54.09	45.55	54.32	54.08
Al2O3	26.90	21.20	23.29	21.07	21.11
Na2O	0.00	0.54	0.45	0.53	0.91
K2O	0.00	10.17	5.86	10.04	9.98
CaO	0.00	0.00	0.00	0.00	0.00
BaO	39.04	13.37	24.43	14.40	14.38
TOTAL	99.48	99.37	99.58	100.36	100.46
NUMBER OF IONS ON THE BASIS OF 8 OXYGENS					
Si	2.06	2.74	2.50	2.74	2.73
Al	1.95	1.27	1.50	1.25	1.26
Na	0.00	0.05	0.05	0.05	0.09
K	0.00	0.66	0.41	0.65	0.64
Ca	0.00	0.00	0.00	0.00	0.00
Ba	0.97	0.27	0.53	0.28	0.28
TOTAL	4.98	4.99	4.99	4.97	5.00

	112otr3	112otr4	112otr5	112v1	112core1	112core2
SiO2	53.86	54.00	53.71	54.51	64.14	64.04
Al2O3	20.49	20.83	20.80	20.61	17.81	17.32
Na2O	0.48	0.31	0.56	0.35	0.57	0.26
K2O	10.25	10.62	9.96	10.46	15.08	15.29
CaO	0.00	0.00	0.00	0.00	0.00	0.00
BaO	13.72	12.97	14.13	12.94	1.20	1.26
TOTAL	98.80	98.73	99.16	98.87	98.80	98.17
NUMBER OF IONS ON THE BASIS OF 8 OXYGENS						
Si	2.76	2.75	2.74	2.77	3.00	3.03
Al	1.24	1.25	1.25	1.23	0.98	0.97
Na	0.05	0.03	0.05	0.03	0.05	0.02
K	0.70	0.69	0.65	0.68	0.90	0.92
Ca	0.00	0.00	0.00	0.00	0.00	0.00
Ba	0.27	0.26	0.28	0.26	0.02	0.02
TOTAL	5.02	4.98	4.97	4.97	4.95	4.96

MUSCOVITE

	Msc431m	Msc431n	Msc431o	Msc431p	Msc431q
SiO2	47.80	47.90	48.80	47.60	47.80
TiO2	0.27	0.26	0.80	0.33	0.89
Al2O3	30.90	30.70	30.70	29.60	31.00
FeO	0.72	0.77	1.05	1.05	0.94
MnO	0.00	0.00	0.00	0.28	0.00
MgO	3.56	3.88	3.33	3.79	3.34
CaO	0.37	0.37	0.27	0.47	0.44
Na2O	0.43	0.00	0.00	0.00	0.00
K2O	11.10	11.10	11.90	11.50	10.90
Cl	0.00	0.00	0.00	0.00	0.00
TOTAL	95.27	94.98	96.85	94.63	95.31
NUMBER OF IONS ON THE BASIS OF 22 OXYGENS					
Si	6.39	6.41	6.44	6.44	6.38
Ti	0.03	0.03	0.08	0.03	0.09
Al3+	4.88	4.84	4.77	4.72	4.87
Fe2+	0.08	0.09	0.11	0.12	0.10
Mn	0.00	0.00	0.01	0.03	0.00
Mg	0.71	0.77	0.65	0.76	0.66
Ca	0.05	0.05	0.04	0.07	0.06
Na	0.11	0.00	0.00	0.00	0.00
K	1.90	1.90	2.00	1.98	1.85
Cl	0.00	0.00	0.00	0.00	0.00
Total	14.15	14.09	14.10	14.16	14.03

PHENGITE

	M434f	M1211a	M1211b	M1211c	M1211d	M1211e
SiO2	46.30	46.50	47.80	49.80	47.40	46.60
TiO2	0.78	0.28	0.19	0.92	0.37	0.74
Al2O3	29.50	32.30	30.60	29.80	31.90	31.30
FeO	1.92	0.89	1.18	0.95	1.26	1.12
MnO	0.00	0.00	0.00	0.00	0.00	0.00
MgO	4.87	4.28	4.46	4.52	4.15	4.49
CaO	0.61	0.23	0.20	0.13	0.10	0.00
Na2O	0.00	0.35	0.43	1.24	0.00	0.80
K2O	11.30	11.30	11.50	10.90	11.00	10.60
Cl	0.00	0.00	0.00	0.00	0.00	0.00
TOTAL	95.28	95.90	95.96	98.13	96.08	96.65
NUMBER OF IONS ON THE BASIS OF 22 OXYGENS						
Si	6.26	6.19	6.36	6.47	6.28	6.22
Ti	0.08	0.03	0.02	0.09	0.04	0.07
Al3+	4.70	5.07	4.80	4.56	4.98	4.92
Fe2+	0.22	0.10	0.13	0.10	0.14	0.13
Mn	0.00	0.00	0.00	0.00	0.00	0.00
Mg	0.98	0.85	0.89	0.88	0.82	0.89
Ca	0.09	0.00	0.00	0.00	0.00	0.00
Na	0.00	0.09	0.11	0.31	0.00	0.21
K	1.95	1.92	1.92	1.81	1.86	1.80
Cl	0.00	0.02	0.00	0.00	0.01	0.00
Total	14.28	14.25	14.23	14.22	14.12	14.25

	CHLORITE					GREENALITE	
	69sil1	69sil2	Chl1211j	Chl1211l	Vn1212x	69Grn1	69Grn2
SiO2	29.67	29.93	28.00	29.60	24.00	42.07	42.17
TiO2	0.00	0.00	0.00	0.00	0.00	0.00	0.00
Al2O3	12.19	12.94	16.90	16.00	20.10	2.49	2.87
FeO	34.69	35.24	28.40	30.30	31.40	39.57	41.08
MnO	0.00	0.00	0.00	0.00	0.00	0.00	0.00
MgO	12.07	11.99	13.00	12.10	11.10	4.05	4.27
CaO	0.00	0.00	0.00	0.00	0.00	0.00	0.00
Na2O	0.00	0.00	0.00	0.00	0.00	0.00	0.00
K2O	0.00	0.00	0.00	0.00	0.00	0.00	0.00
Cl	0.00	0.00	0.00	0.00	0.00	0.00	0.00
TOTAL	88.62	90.10	86.58	88.00	86.60	88.40	90.39
	NUMBER OF IONS ON THE BASIS OF 28 OXYGENS					14 OXYGEN	
Si	6.50	6.44	6.06	6.33	5.32	4.61	4.54
Ti	0.00	0.00	0.05	0.00	0.00	0.00	0.00
Al	3.15	3.28	4.31	4.03	5.25	0.32	0.36
Fe2+	6.35	6.34	5.14	5.42	5.82	3.63	3.70
Mn	0.00	0.00	0.00	0.00	0.00	0.00	0.00
Mg	3.94	3.85	4.19	3.86	3.67	0.66	0.68
Ca	0.00	0.00	0.00	0.00	0.00	0.00	0.00
Na	0.00	0.00	0.00	0.00	0.00	0.00	0.00
K	0.00	0.00	0.00	0.00	0.00	0.00	0.00
Cl	0.00	0.00	0.00	0.00	0.00	0.00	0.00
TOTAL	19.93	19.92	19.74	19.65	20.06	9.23	9.28

	CHLORITZED BIOTITE					
	69ClBt1	69ClBt2	69ClBt3	69ClBt4	124ClBt1	124ClBt2
SiO2	39.24	39.82	40.12	39.52	35.96	35.38
TiO2	0.60	0.42	0.44	0.66	2.35	2.43
Al2O3	13.31	13.44	13.15	12.91	15.67	15.47
FeO	15.86	15.37	15.28	17.02	20.95	20.73
MnO	0.00	0.00	0.00	0.00	0.43	0.00
MgO	14.79	15.37	14.93	14.42	11.07	10.45
CaO	0.00	0.00	0.00	0.00	0.00	0.00
Na2O	0.00	0.52	0.00	0.00	0.00	0.00
K2O	7.42	7.46	7.54	7.78	8.06	7.51
Cl	0.00	0.00	0.00	0.00	0.00	0.00
TOTAL	91.22	92.40	91.46	92.31	94.49	91.97
	NUMBER OF IONS ON THE BASIS OF 22 OXYGENS					
Si	6.04	6.04	6.13	6.06	5.54	5.58
Ti	0.07	0.05	0.05	0.08	0.27	0.29
Al	2.41	2.40	2.37	2.33	2.85	2.88
Fe2+	2.04	1.95	1.95	2.18	2.70	2.73
Mn	0.00	0.00	0.00	0.00	0.06	0.00
Mg	3.39	3.48	3.40	3.29	2.54	2.46
Ca	0.00	0.00	0.00	0.00	0.00	0.00
Na	0.00	0.15	0.00	0.00	0.00	0.00
K	1.46	1.44	1.47	1.52	1.59	1.51
Cl	0.00	0.00	0.00	0.00	0.00	0.00
TOTAL	15.41	15.51	15.37	15.46	15.55	15.45

APPENDIX V - CARBON AND OXYGEN ISOTOPE CATALOGUE

JCU #	HS#	Description paragenetic stage - host rock - strat. interval	Relative strat. position (m)	δ18O (‰) (SMOW)	δ13 C (‰) (PDB)
44685	008	Stage OI whole rock ferroan dolomite - BM - I interval	9.2	18.2	-3.8
44686	0012a	Stage OI whole rock ferroan dolomite - BM - I interval	21.0	18.2	-3.5
44700	0044b	Stage OI whole rock ferroan dolomite - BM - I interval	56.5	18.4	-2.6
44690	0022b	Stage OI whole rock ferroan dolomite - MM - I interval	44.0	18.4	-2.7
44717	100	Stage OI whole rock ferroan dolomite - MM - I interval	7.0	18.2	-2.6
44718	101	Stage OI whole rock ferroan dolomite - MM - I interval	10.0	18.2	-2.6
44685	0008	Stage OI whole rock ferroan dolomite - SM - I interval	9.0	18.0	-3.8
44728	127	Stage OI whole rock ferroan dolomite - SM - I interval	62.5	18.5	-2.9
44818	DC36845	Stage OI whole rock ferroan dolomite - BM - C interval	234.0	17.2	-1.7
44817	DC36840	Stage OI whole rock ferroan dolomite - BM - C interval	232.5	17.3	-1.5
44817	DC36840	Stage OI whole rock ferroan dolomite - BM - C interval	232.0	17.1	-1.4
44711	0083i	Stage VIII whole rock ferroan carbonate - BM - A interval	318.0	16.2	-4.0
44753	202b	Stage VIII whole rock ferroan carbonate - BM - B interval	268.0	16.5	-2.1
44757	226b	Stage VIII whole rock ferroan carbonate - BM - B interval	241.0	16.6	-2.1
44700	0044b	Stage I calcite - MM - I interval	56.0	18.0	-2.9
44709	0079c	Stage I calcite - MM - I interval	72.0	17.4	-1.7
44732	132	Stage I calcite - MM - I interval	83.0	17.1	-3.0
44686	0012a	Stage I calcite - WB - I interval	21.1	17.7	-3.7
44689	0020g	Stage I calcite - WB - I interval	38.0	17.8	-2.6
44691	0023b	Stage I calcite - WB - I interval	45.5	17.7	-2.4
44726	125	Stage I calcite - WB - I interval	61.0	17.7	-4.1
44728	127	Stage I calcite - WB - I interval	61.0	17.8	-3.1
44817	DC36840	Stage I calcite - WB - C interval	232.6	15.0	-2.4
44818	DC36845	Stage I calcite - WB - C interval	234.1	14.4	-3.0
44817	DC36840	Stage I calcite - WB - C interval	232.1	14.4	-2.2
44691	0023b	Stage I calcite - Nod - I interval	45.0	17.8	-2.7
44717	100	Stage I calcite - Nod - I interval	7.5	17.9	-3.2
44817	DC36840	Stage I calcite - Nod - C interval	232.7	14.9	-1.9
44817	DC36840	Stage I calcite - Nod - C interval	232.2	16.2	-1.3
44818	DC36845	Stage I calcite - Nod - C interval	234.2	13.0	-2.8
44815	DC36839	Stage I calcite - Nod - C interval	237.0	14.9	-1.9
44815	DC36839	Stage I calcite - Nod - C interval	237.4	15.4	-1.9
44723	118	Stage VIII feroan carbonate - Nod - H interval	80.0	15.7	-4.0
44724	122	Stage VIII feroan carbonate - Nod - H interval	85.0	15.3	-3.5
44736	138b	Stage V sugary ferroan dolomite vein infill - E/F interval	183.0	17.1	-1.6
44735	137a	Stage V sugary ferroan dolomite vein infill - E/F interval	161.0	16.5	-2.7
44744	159	Stage V sugary ferroan dolomite vein infill - E/F interval	158.0	14.6	-1.7
44743	158	Stage V sugary ferroan dolomite vein infill - E/F interval	156.0	14.9	-1.9
44772	272b	Stage IXa ferroan dolomite vein infill - H interval	93.0	16.2	-4.6

APPENDIX VI - Pb ISOTOPE CATALOGUE

JCU #	HS#	Sample description-stratigraphic interval	206Pb/204Pb	207Pb/204Pb	208Pb/204Pb
44772	272a	Stage IXa galena infill in J75-type fault; Hhw	16.089	15.417	35.734
44779	289	Stage IXa galena infill in J75-type fault; Hhw	16.108	15.446	35.804
44813	UG29	Stage VII coarse-grained galena breccia; D	16.087	15.417	35.716
44813	UG29	Stage VII coarse-grained galena breccia;D	16.115	15.456	35.831
44813	UG29	Stage VII coarse-grained galena breccia; D	16.103	15.44	35.778
44813	UG29	Stage VII coarse-grained galena breccia; D	16.096	15.434	35.75
44813	UG29	Stage VII coarse-grained galena breccia; D	16.112	15.451	35.82
44811	UG25	Stage VII coarse-grained galena breccia; D	16.096	15.429	35.785
44747	173b	Stage VII medium-grained galena breccia; D	16.109	15.445	35.81
44801	UG8	Stage VII medium-grained galena breccia; C	16.12	15.454	35.83
44784	296	Stage VII medium-grained galena breccia; D	16.097	15.433	35.759
44794	UG1	Stage VII discordant galena vein; C	16.117	15.45	35.817
44808	UG15	Stage VII discordant galena vein; C	16.115	15.456	35.847
44781	292	Stage VII discordant galena vein; D	16.113	15.455	35.83
44812	UG26	Stage VII discordant galena vein; D	16.117	15.453	35.826
44812	UG26	Stage VII discordant galena vein; D	16.098	15.427	35.754
44812	UG26	Stage VII discordant galena vein; D	16.093	15.428	35.748
44813	UG29	Stage VII discordant galena vein; D	16.107	15.446	35.813
44781	292	Stage VII galena matrix in mixed sulphide breccia; D	16.101	15.43	35.758

APPENDIX VII - SULPHUR ISOTOPE CATALOGUE

JCU #	HS #	δ34SCDT	Mineral	DESCRIPTION
44810	UG#23	9.9	Galena	Stage VII medium-grained galena breccia with sphalerite clasts; C
44810	UG#23	9.6	Sphalerite	Stage VII fine to med grained red-brown sphalerite breccia; C
44802	UG#9	8.7	Sphalerite (AgS)	Stage IV nodular calcite-hosted medium-grained honey sphalerite; C
44802	UG#9	10.6	Pyrite	Stage II-IV spheroidal-brassy pyritie mixture from rhythmically laminated pyritic siltstone; C
44725	LC 123	9.7	Sphalerite (AgS)	Stage IV nodular calcite-hosted medium-grained honey sphalerite; Hfw
44725	LC 123	8.3	Brassy Pyrite	Stage II-IV spheroidal-brassy pyritie mixture from rhythmically laminated pyritic siltstone; Hfw
44738	LC 144	9.7	Sphalerite	Stage IV breccia-vein -hosted, coarse-grained orange sphalerite; D
44737	LC 143	10	Galena	Stage VII discordant vein-hosted galena; D
44791	LC 305	14.2	Galena	Stage VII discordant vein-hosted galena; E
44791	LC 305	13.4	Sphalerite	Stage IV breccia-vein-hosted, medium-grained brown sphalerite; E
44772	LC 272b	7.6	Sphalerite	Coarse red-brown sphalerite infill in Stage IXa dol-qtz-cal-Py-Po-Cpy-Gn-Sp vein; Hhw
44772	LC 272b	7.6	Sphalerite	Coarse red-brown sphalerite infill in Stage IXa dol-qtz-cal-Py-Po-Cpy-Gn-Sp vein; Hw
44772	LC 272b	6.1	Galena	Coarse galena infill in late-stage dol-qtz-cal-Py-Po-Cpy-Gn-Sp vein; Hhw
44772	LC 272b	5.4	Galena	Coarse galena infill in late-stage dol-qtz-cal-Py-Po-Cpy-Gn-Sp vein;Hhw
44737	LC 305	14.2	Galena	Stage VII discordant vein-hosted galena; E
44737	LC 305	13.9	Sphalerite (AgS)	Stage IV breccia-vein-hosted, medium-grained brown sphalerite; E

APPENDIX VIII - BITUMEN REFLECTANCE DATA

JCU # 44714 , HS# 0087f, PTS# 56ii - Migrabitumen Population 2, meso-impsonite

	B *Ro* min	B *Ro* max
	2.8	2.96
	2.63	2.7
	2.7	2.78
	2.59	2.73
	2.54	2.98
	2.82	2.92
	2.82	2.91
	2.9	3.01
	2.88	2.97
	2.62	2.87
	2.58	2.82
	2.52	2.68
	2.91	3.13
	2.52	2.96
	2.48	2.95
	2.78	2.96
	2.9	3.03
	2.53	2.73
	2.41	2.86
	2.85	2.96
	2.57	3
	2.62	3.19
		Avg=2.91
		Mean=2.95
		SD=0.1297

JCU # 44722 , HS# 117, PTS# 161 - Migrabitumen Population 2, cata-impsonite

	B *Ro* min	B *Ro* max
	4	5.11
PTS161	4.43	4.79
	3.89	4.81
	4.5	5.07
	4.07	5.22
	4.27	5.16
	4.71	5.39
	4.18	5.04
	3.97	5.06
	3.75	4.47
	2.95	4.25
	3.72	4.7
	4.64	6.2
	4.19	5.93
	4.74	5.41
	5.63	6.31
	5.75	6.41
	5.64	6.31
		Avg=5.31
		Mean=5.33
		SD=0.6407

JCU # 44697 , HS# 0033d, PTS# 4 - Migrabitumen Population 1, epi-impsonite

	B *Ro* min	B *Ro* max
	0.54	1.4
	0.7	1.61
	0.62	1.47
	0.74	1.55
	0.66	1.33
	0.76	1.43
	0.94	1.35
		Avg=1.45
		Mean=1.47
		SD=0.095

APPENDIX IX - TOTAL ORGANIC CARBON ANALYSES

JCU#	HS#	Sample description	Total Carbon (ppm)	Organic Carbon (ppm)
44694	0029d	SM	51250±320	34355±45
44709	0079g	MM - calcitic	88680±450	34420±120
44815	DC36839	PS	47660±90	3594±5
44693	0025d	BM	41665±655	3696±73
44707	0063d	MM - dolomitic	76605±45	28400±280
44700	0044a	SM	48990±470	10800±30